B. AHMED

ATILIM UNIVERSITY 2022

EXPLORING THE POTENTIALS OF COMMERCIAL RADAR CHIPSETS FOR PROXIMITY SENSING WITH RESOLVING VELOCITY AMBIGUITY

THE GRADUATE SCHOOL OF NATURAL AND APPLIED SCIENCES
OF
ATILIM UNIVERSITY

BADAR-UD-DIN AHMED

A DOCTOR OF PHILOSOPHY THESIS
IN
THE DEPARTMENT OF MODELING AND DESIGN OF ENGINEERING SYSTEMS (MAIN FIELD OF STUDY: ELECTRICAL & ELECTRONICS ENGINEERING)

JANUARY 2022

EXPLORING THE POTENTIALS OF COMMERCIAL RADAR CHIPSETS FOR PROXIMITY SENSING WITH RESOLVING VELOCITY AMBIGUITY

A THESIS SUBMITTED TO
THE GRADUATE SCHOOL OF NATURAL AND APPLIED SCIENCES
OF
ATILIM UNIVERSITY

BY

BADAR-UD-DIN AHMED

IN PARTIAL FULFILLMENT OF THE REQUIREMENTS
FOR
DOCTOR OF PHILOSOPHY
IN
THE DEPARTMENT OF MODELING AND DESIGN OF ENGINEERING SYSTEMS (MAIN FIELD OF STUDY: ELECTRICAL AND ELECTRONICS ENGINEERING)

JANUARY 2022

Approval of the Graduate School of Natural and Applied Sciences, Atilim University.

Prof. Dr. Ender KESKİNKILIÇ
Director

I certify that this thesis satisfies all the requirements as a thesis for the degree of **Doctor of Philosophy in Modeling & Design of Engineering Systems, Atılım University**.

Prof. Dr. Ender KESKİNKILIÇ
Head of Department

This is to certify that we have read the thesis EXPLORING THE POTENTIALS OF COMMERCIAL RADAR CHIPSETS FOR PROXIMITY SENSING WITH RESOLVING VELOCITY AMBIGUITY submitted by BADAR-UD-DIN AHMED and that in our opinion it is fully adequate, in scope and quality, as a thesis for the degree of Doctor of Philosophy.

Assistant Prof. Dr. Ertan Zencir
Co-Supervisor

Prof. Dr. Ali Kara
Supervisor

Examining Committee Members:

Prof. Dr. Şimşek Demir
Electrical & Electronics Eng. Department,
Middle East Technical University

Prof. Dr. Ali Kara
Electrical & Electronics Eng. Department,
Gazi University

Prof. Dr. Alaaeldeen Elrouby
Electrical & Electronics Eng. Department,
Ankara Yıldırım Beyazıt University

Prof. Dr. Elif Aydın
Electrical & Electronics Eng. Department
Atılım University

Asst. Prof. Dr. Yaser Dalveren
Avionics Eng. Department
Atılım University

Date: *20th January, 2022*

I hereby declare that all information in this document has been obtained and presented in accordance with academic rules and ethical conduct. I also declare that, as required by these rules and conduct, I have fully cited and referenced all material and results that are not original to this work.

Name, Last Name : Badar-ud-din Ahmed

Signature :

ABSTRACT

EXPLORING THE POTENTIALS OF COMMERCIAL RADAR CHIPSETS FOR PROXIMITY SENSING WITH RESOLVING VELOCITY AMBIGUITY

Ahmed, Badar-ud-din
PhD., Department of Modeling & Design of Engineering Systems
Supervisor : Prof. Dr. Ali Kara
Co-Supervisor : Assist. Prof. Dr. Ertan Zencir

January 2022, 124 pages

In this thesis, an attempt is made to explore the potentials of Commercial-off-the-shelf (COTS) Frequency Modulated Continuous Wave (FMCW) mmwave automotive radar for proximity sensing with a focus on endeavour to resolve velocity ambiguity. The selected hardware platform operates in 77 GHz ~ 81 GHz frequency band. A 9 mm pistol bullet was initially selected as prospective target because it could be fired with speed of almost 300 m/s speed which is many orders of magnitude higher than typical speeds encountered in the automotive scenarios and for which automotive radars are designed. This selection of 9 mm bullet led to a RCS measurement study which has not been attempted earlier in similar frequency band for such target types.

Due to safety and other allied reasons, a 5.5 mm airgun pellet was decided to be used in field experiments instead of 9 mm bullet. A magnitude interpolation technique was developed for resolving phase ambiguity in complex numbers and the resolved phase was then used to measure the speed of the small RCS high-speed target (5.5 mm airgun pellet). The proposed method is a novel but nascent application of classical relation between magnitude and phase angle of complex numbers which can be possibly applied in other scientific fields and scenarios as well.

Subsequently, extensive sets of field experiments were conducted to study and demonstrate the use of Chinese Remainder Theorem (CRT) for resolving velocity ambiguity. CRT is an important theorem in number theory but it is known to be prone to errors. The research in this thesis helps to demonstrate that CRT can be used for effectively resolving velocity ambiguity in COTS FMCW radar, provided that the requisite parameters are tuned judiciously. Such demonstration of velocity ambiguity resolution by CRT application for similar types of target by using comparable frequency band, has not been reported earlier in the literature.

Certain peculiar aspects with regards to study of phase in frequency domain analysis were encountered which have been compiled for tutorial purposes at the end of the thesis.

Keywords: 77 GHz automotive radar, FMCW radar, Velocity ambiguity, Bullet velocity measurement, Phase measurement

ÖZ

TİCARİ RADAR YONGALARININ HIZ BELİRSİZLİĞİNİN OLMADIĞI TAPA SENSÖRÜ OLARAK KULLANILMASI

Ahmed, Badar-ud-din
Doktora, Mühendislik Sistemlerinin Modellenmesi ve Tasarımı
Danışman : Prof. Dr. Ali Kara
Eş-danışman : Dr. Öğrt.Üyesi Ertan Zencir

Ocak 2022, 124 sayfa

Bu tez çalışmasında, otomotiv uygulamaları için tasarlanmış Frekans Modülasyonlu Sürekli Dalga (FMSD) RAfta HAzır Ticari (RAHAT) yonganın, tapa sensöründe hız belirsizliği olmadan kullanım potansiyeli çalışılmıştır. Hedef milimetre radar platformu (yonga) 77-81 GHz bandında çalışmaktadır. Tipik otomotiv radarındaki hedef hızları ile kıyaslandığında 300 m/sn hızlara kadar çıkabilen 9mm'lik tüfekler hedeflenmiştir. Bu durumda, daha önce literatürde karşılaşılmayan, bu bantlardaki mermi radar kesit alanı (RKA) ölçümleri öncelikle çalışılmıştır. Ardından hız testleri için ise güvenlik ve ilgili mevzuat kısıtları dikkate alınarak 5.5mm'lik havalı tüfek atışları kullanılmıştır. Yankı sinyalinin genlik faz değişiminin doğrusal olması ile öncelikle faz belirsizliği giderilerek hız tespiti çalışılmıştır. Bu bilinen bir yöntem olmakla birlikte bu bant ve uygulama için ilk defa çalışılmıştır ve bazı kısıtları olduğu bilinmektedir. Ardından çoklu darbe tekrarlama frekansı kullanımına dayanan Çinlilerin Kalanlar Teoremi (ÇKT), hız belirsizliğini gidermek amaçlı olarak kullanılmıştır. Deneysel çalışmalar sonucunda ÇKT bazlı çoklu darbe tekrarlama aralığı kullanımının hızdaki belirsizliği gidererek otomotiv radarı ile çok yüksek hızlardaki küçük cisimlerin hızlarını ölçebileceği gösterilmiştir.

Anahtar Kelimeler: 77 GHz otomotiv radarı, FMSD radar, hız belirsizliği, mermi hızı ölçümü, faz ölçümü

To …my parents, my family and my country

ACKNOWLEDGMENTS

Praise be to Almighty Allah, who created the provisions and circumstances for me to undertake this PhD study and then provided the means to complete it.

Next, I am indebted to the Government of Pakistan for granting me the scholarship to undertake PhD studies in this beautiful and historic country of Turkey which has become a life-long cherishable memory to me.

I must express my utmost gratitude to Prof. Dr. Ali Kara for being my supervisor. In addition to being my mentor in the academic studies and for arranging whatever equipment and resources I needed for my research, he has been a tremendous support and guidance in whatever sphere I requested him, be it be living in Turkey, travelling across breadth of Turkey or any other aspect of academic or personal life.

I also feel indebted to Dr Ertan Zencir, the co-supervior, for many insightful discussions on various matters that immensely enhanced my understanding on many diverse topics.

I feel lucky to have Prof. Dr. Simsek Demir on my Thesis Examining Committee. His vast and deep knowledge in FMCW radar engineering, especially from application aspects and the discussions and question answer sessions during the various thesis progress evaluation sessions, enabled me to grasp some very key concepts.

Prof. Dr. Alaa Elrouby with his expertise in microwave engineering also brought forward critical questions and suggestions as the member of Thesis Examining Committee and I am thankful to him.

I must also express my gratitude to the faculty and staff of Atilim University. It was a really memorable experience to take various courses from worthy faculty members. In addition, the support and conduct of administrative staff in all units of the university was very forthcoming.

I particularly wish to express my gratitude towards Mr. Eyyup Sarikaya and Mr. Tayep Ozdemir for their sincere support whenever I needed, whether it was related to field experiments or to any other aspect of living in a foreign country.

TABLE OF CONTENTS

CHAPTER

LIST OF TABLES

TABLES

LIST OF FIGURES

FIGURES

CHAPTER 1

INTRODUCTION

Radio Detection and Ranging (RADAR) traces back its development to more than a hundred years ago when Heinrich Hertz performed pioneer experiments on radar in the late nineteenth century. However, it was mostly during the World War II (WWII) that immense research and development was witnessed in the radar technology. Various types of radar technologies and principles evolved over the time. Among them, Continuous Wave (CW) Radar could be virtually termed the simplest radar due to higher sensitivity, simpler architecture and lesser average power [1], as compared to the pulse radar. However, CW radars can only measure the velocity. In order to enable CW radar to measure range, the carrier frequency of CW radar needs to be modulated [2]. Among several kinds of modulation, Frequency Modulation (FM) is most commonly used modulation technique with CW to implement Frequency Modulation Continuous Wave (FMCW) radar, particularly for range measurement [1]. The FMCW radars have the capability of detecting static and moving targets alike [3]. In yester years, owing to certain technological constraints and its basic principle, use of FMCW radar remained primarily limited to certain special and limited applications. However, FMCW radars started to become available in increasingly smaller form factor and with gradually higher level of circuit abstraction which become possible due to miniaturization and progress in semiconductor technology. Significant research is being carried out on FMCW mmwave radars both by academic entities and by industrial concerns. This research is gradually shifting in vertically higher levels of integration and circuit abstraction i.e. from discrete components to building blocks ICs (e.g. transmitter, receiver, Phase Locked Loop (PLL), Voltage Controlled Oscillator (VCO)) to complete radar transceiver packaged in one single IC.

Apart from the working principle segregation, the radars are differentiated into several classes based on the working frequency. Millimeter wave (mmwave) is one of the several frequency ranges used for the radar. Mmwave radars have been in use for quite a long time now, however, the first use of mmwave radar in automotive field was reported in early 1970's [4]. Nonetheless, inefficient integration level, higher cost, bigger size and technology complexity forbade entry to any feasible and practical mmwave radar product into the automotive market until late 1990's [1].

1.1 FMCW Automotive Radar

FMCW mmwave radars gradually found use in automotive market over the years. At the onset, such radars were employed as passive comfort features in only luxury and higher end cars. However, with the passage of time, two phenomena occurred. First, naturally, the FMCW mmwave technology matured, became integration-friendly and cost-effective. Second, the use of FMCW radar shifted from passive comfort to active safety functions. As a result, FMCW radars are forecasted to be integrated soon even in mid-range cars and that too with active safety features like Automatic Emergency Braking (AEB). The following TABLE I from [4] summarizes the transition of features of automotive radars over the time:

TABLE I TRANSITION OF FEATURES OF AUTOMOTIVE RADARS

Automotive Radar Application Domain	Example
Passive Comfort	Parking Aid
Passive Safety	Airbag
Active Comfort	Adaptive Cruise Control (ACC)
Active Safety	Automatic Emergency Braking (AEB)

The automotive radars are becoming widely available at the ever-decreasing costs. Some of the well-known automotive radar modules are being produced by OEMs like Bosch, Delphi, Toyota, Continental, Fruno and Denso [5], [6], [4]. Many OEMs are producing constituent components of the automotive radars, however, the complete radar transceiver chipsets or chipsets with one lower level of circuit abstraction are being produced by the OEMs like Analog Devices, Infineon, NXP, Texas Instruments and ST Microelectronics. Like any other scientific field, FMCW radar technology is also governed by theoretical calculations coupled with hardware constraints. Given the cost-effective wide availability of millimeter-wave (mmwave) automotive radars, it is naturally appealing to the application experts and technologists to extend the operational limits of the mmwave automotive radars beyond the specifications dictated by the hardware constraints. The two most important issues in order to extend the operational limits of the automotive radars are to resolve ambiguities in the range measurement and velocity measurement [7], [8], [9]. Ambiguity is an uncertainty in the measurement when a target possibly has a range (or velocity) greater than the maximum measurable value for which the radar was designed to provide unambiguous reading. In this case, it cannot be ascertained whether the measured range (or velocity) is the true value or a value folded into the designed unambiguous limits. If and when the ambiguity can be resolved effectively, certainly the measurable range/velocity can be extended.

It is pertinent to mention here that the ambiguity resolution concept and problem have been traditionally more relevant and pronounced in pulse (Doppler) radars as compared to FMCW radars [9]. The reason is that the FMCW radars have been usually used more often in simple applications like level sensing [10], [11], proximity sensing [12] etc, which involve relatively closer ranges than pulse (Doppler) radars. Indeed, FMCW radars have also been used for velocity measurements, but their prevalent applications do not usually involve higher velocities, for example health care applications [13], [14] , vital signs detection [15] etc. Even in case of typical use of automotive radars, the velocities encountered by FMCW radars are much lower than the ones typical with the pulse radars as used for example in air traffic control.

1.2 The Problem Statement

It is a well-known and established fact that usually any technology gradually finds wider and divergent application areas as it progresses from inception to maturity. The prevalent focus of ongoing research on FMCW mmwave automotive radar is on increase in velocity resolution, range resolution and angular position resolution of individual and multiple targets ranging from automotive vehicles to pedestrians. In addition, the researchers and application experts are exploring use of commercial-off-the-shelf (COTS) automotive mmwave radars in vast number of diverse applications.

This thesis endeavours the research on exploring the potentials of COTS FMCW mmwave automotive radar for proximity sensing with resolving velocity ambiguity. The desired measurable velocity limit is approximately 0.8~0.9 Mach which is well beyond the velocity limit for which the automotive radars are designed. Thus, an ambiguity is bound to be present if velocity of such a magnitude is attempted to be measured with some automotive radar. Therefore, the main focus of the thesis is research on attempt to resolve velocity ambiguity in COTS FMCW mmwave automotive radar.

As the desired speed is in several orders of magnitude higher than the typical automotive speeds, therefore, it was envisaged to use 9 mm bullet as probable target for speed measurement. This idea triggered a study of Radar Cross Section (RCS) measurement of 9 mm bullet with a COTS FMCW mmwave automotive radar. However, owing to safety, weapon availability and other reasons, the remaining experiments were conducted with 5.5 mm airgun pellet as small RCS high-speed target.

The thesis thus constitutes theoretical and experimental study and research to resolve ambiguity in speed measurement of a small RCS high-speed target (5.5mm airgun pellet) with a COTS FMCW mmwave automotive radar platform.

1.3 Composition of The Thesis

The subsequent chapters of the incumbent thesis are organized as follows:

Chapter 2 presents a brief state-of-art of COTS FMCW mmwave automotive radars which is followed by a theoretical introduction to FMCW radars.

Chapter 3 presents results of a study conducted for RCS measurement of 9 mm bullet with 77 GHz COTS FMCW automotive radar.

Chapter 4 provides details of a magnitude interpolation technique proposed to resolve ambiguity in phase angle measurement of complex numbers. This technique is further demonstrated with an experimental study to resolve the ambiguity in velocity measurement of a fast-moving small RCS target which is a 5.5mm airgun pellet.

Chapter 5 describes an experimental field study on use of Chinese Remainder Theorem (CRT) for resolving ambiguity in speed measurement of the fast-moving small RCS airgun pellet.

Chapter 6 consolidates some peculiar application aspects observed during the use of COTS FMCW automotive radars.

Chapter 7 concludes the dissertation with conclusions and possible venues for future research.

In order to avoid explicitly advertising a particular product, the COTS FMCW mmwave automotive radar module used during the research for this thesis, has been purposefully not identified. However, the relevant radar parameters have been described where necessary.

CHAPTER 2

FMCW RADAR : AN ABRIDGED INTRODUCTION

2.1 Brief State-of-Art of mmwave FMCW Automotive Radars

2.1.1 Silicon Technology

A limited and approximate scenario of Silicon technology transition with respect to mmwave automotive radars is as follows:

1999: Emergence of 77 GHz mmwave commercially available radar sensors based on GaAs Gunn diodes [4].

2006: GaAs MMIC chips become commercially available as COTS for realization of 77 GHz FMCW radar systems [16].

2006-09: Gradual progress and use of SiGe technology for 77 GHz automotive radar MMICs.

2009-10: 77 GHz FMCW mmwave works are reported with 90 nm CMOS technology [17], [18].

2013: 77 GHz transceiver chip IC reported to be produced with 65 nm CMOS technology [17].

2015-16: The main obstacle in the way of popularity of 77 GHz radar is identified to be the cost of the CMOS technology based MMICs and it was hoped that soon the impediments would be overcome [18]. FMCW radar transceivers are mostly realized using SiGe technology, however, capabilities of CMOS technology are also increasing and it may soon find application in 77 GHz radar transceiver technology [19]. Reference [19] reports implementation of continuous wave (CW, not FMCW) 77 GHz radar transceiver by employing 20 nm CMOS technology.

2017: Implementation of complete 77 GHz radar transceiver chip on 130 nm SiGe BiCMOS 8HP technology reported [20].

2018: 77 GHz automotive FMCW mmwave complete radar transceivers are now available as COTS based on CMOS technology with 40 nm technology node.

Research works are continually reported in the literature based on the transceiver ICs designed and fabricated by various research groups in frequency ranges beyond 77-81 GHz. However, it is not known that whether those ICs evolved into mature, industrialized products for commercial use or not. Nonetheless, 77-81 GHz family radars dominate the COTS market and the prominent OEMs producing automotive FMCW radar transceivers or constituent ICs include Analog Devices, Infineon, ST Microelectronic, Texas Instruments and NXP.

2.1.2 Operating Frequency

The 24 GHz band was temporarily opened in the European market in the year 2005 by the European Telecommunications Standards Institute (ETSI) for Short Range automotive Radars (SRR) [3]. Some OEMs continue to provide products in 24 GHz band while many OEMs offer 77 GHz transceivers with up to 4 GHz bandwidth. However, there are certain country-specific scenarios also, for example, in Japan, 77 GHz radar are allowed to have only 0.5 GHz bandwidth and therefore 79 GHz are separately considered and developed [20]. 77-81 GHz is the most widely used frequency band these days for mmwave FMCW radar transceiver products.

2.1.3 Complex and Real Base-band Processing

Real, as well as, Complex baseband processing is available in certain COTS radar transceivers. Real processing enables simpler frontend processing whereas Complex baseband processing also offers better image and interference rejection capabilities.

2.1.4 General Classification of Automotive FMCW Radar Modules

There is no well-defined categorization criterion for classification of automotive radars. However, the following general distinction exists:

Short Range Radar (SRR): A relatively wideband application working within a distance of 30 m, usually used for stop & go, collision avoidance and blind spot detection features. These radars are either operated at 22-29 GHz or 77-81 GHz frequency range [17], [18].

Long Range Radar (LRR): These radar configurations are used for Automatic Cruise Control (ACC) with a frequency range of 77-81 GHz, range detection capability of 150 m and employ relatively narrow beam width as compared to SRR [17], [18].

Mid Range Radar (MRR): Some manufacturers use an additional range between SRR and LRR as Mid Range Radar.

Although use of separate radars with separate frequencies has been seen earlier for SRR and LRR, however, it is becoming more common to use single radar for SRR, MRR and LRR configurations and this is commonly done with 77-81 GHz radar. These three different functionalities are achieved by multiplexing the radar operation for the three modes and by employing different antenna configurations, using various beam forming techniques and varying chirp parameters of the same radar system for different radar modes.

2.1.5 Comparative Works on Complete Radar Systems

Some research works have been witnessed in the literature which compare the performances and parameters of complete automotive radar modules produced by various OEMs. One such work compares the performances of radar by Toyota Laboratories, LRR3 automotive radar from Bosch and ARS300 automotive radar by Continental ADC [5]. A contemporary work compares the specifications of Bosch LRR3, Continental ARS300 and Denso DNMWR004 radar systems [4]. Some of the recent entrants in complete radar systems include Vayyar, Ainstein and Uhnder.

2.1.6 Some Observations on Commercially Available mmwave FMCW Automotive Radars

The automotive radar transceivers market was initially dominated by 24 GHz products however now 77 GHz products are also appearing in the market. The business strategy of the OEMs is complex. Some OEMS are only producing 24 GHz products and some OEMS are only producing 77-81 GHz products. In addition, there are some other OEMs who are marketing their 24 GHz products and they have reported/advertised work on 77-81 GHz products but their 77-81 GHz products are not yet available in the open customer market. The abstraction level of the system also varies among the various OEMs. Some OEMs offer complete radar transceivers ICs while others offer products with a lower level of abstraction i.e. they offer transmitter, receiver and Phased Locked Loop (PLL) (as signal source) ICs and the customer needs to integrate them on its own. Still other/same OEMs offer additional products with further lower abstraction level. The various offered products provide real baseband processing and complex baseband processing capabilities; the choice depends upon the customer while considering other attributes. Usually, the IF output is provided for the customer use in certain format/protocol e.g. Low Voltage Differential Signalling (LVDS) protocol. The IF output is provided for customer use after being digitized by ADC. The ADC sampling rate is at times selectable by the user within certain limits. Further analysis and processing of the IF output is possible at the user end. The product portfolios sometimes include different products for industrial sector and automotive sector.

2.2 Abridged Theory of FMCW Radar

The research in this thesis is based on the Inphase-Quadrature (I/Q) architecture of FMCW radars which is generally shown as in Figure 2.1 [21] :

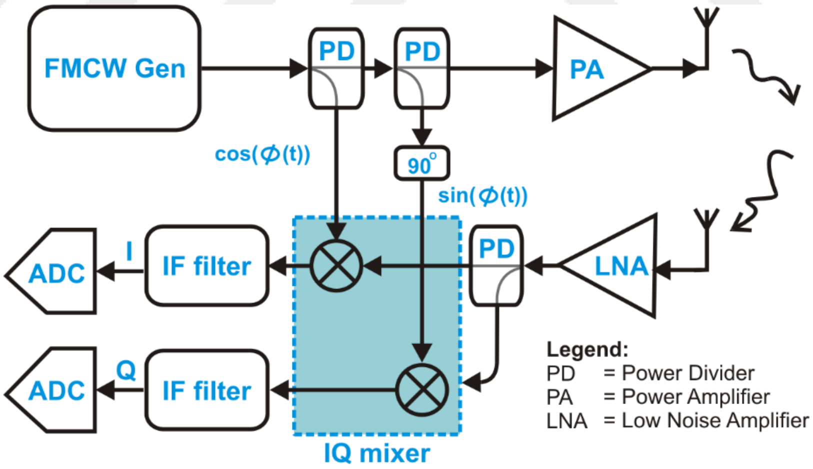

Figure 2.1 FMCW Radar I/Q Architecture

The I/Q Intermediate Frequency (IF) architecture enables the acquisition of IF frequency in complex number format which has range and velocity information ciphered into it. As an introduction to the subject, summarized equations are presented which describe the I/Q IF frequency output of a FMCW radar. The content is mainly derived and summarized from [21], [22], [23], [24], [25], [26] and [27] along with some additional notes from the author.

A general (co)sinusoidal signal is given by the Eq. (2.1):

$$x(t) = A\cos\big(\emptyset(t)\big) \tag{2.1}$$

where A is the amplitude of the signal and $\emptyset(t)$ is the instantaneous phase of the signal. We choose to use a cos() operator in order to denote a real valued signal consistent with Euler's complex exponential. The shape of $\emptyset(t)$ function defines the phase or frequency modulation. A most commonly used modulation in FMCW is Linear Frequency Modulation (LFM) whose instantaneous frequency is given by the relation

$$f(t) = f_c + St \tag{2.2}$$

where f_c is the initial carrier frequency, S is the slope of the frequency waveform and is given by $S = B\ /\ T_c$, where B is the bandwidth of the frequency modulation and T_c is the chirp time or chirp duration.

For the moment we will study a single segment of the signal with time t running from 0 to T_c. Frequency in Eq. (2.2) is easily converted to radian frequency by $\omega = 2\pi f$ and then the phase angle is defined as the accumulated phase shift over time and is given by the integral

$$\emptyset(t) = 2\pi \int_0^t f(t)dt = 2\pi\left(f_c t + \frac{S}{2}t^2\right) + \varphi_0 \tag{2.3}$$

where φ_0 is the initial phase. Eq. (2.1) can then be written for the transmitted LFM signal with magnitude F as follows:

$$x_{tx}(t) = F\cos\left(2\pi\left(f_c t + \frac{S}{2}t^2\right) + \varphi_0\right) \tag{2.4}$$

Eq. (2.4) describes the transmitted signal for the first chirp (from $t = 0$ to T_c). FMCW radars repeatedly transmit such chirps, which can be grouped into bursts. A burst of chirps with identical chirp parameters will be later referred to as a Coherent Processing Interval (CPI). As chirps in a burst are repeated with constant time interval T_c, this interval defines the Pulse Repetition Frequency (PRF) – the rate at which the chirps are transmitted by the radar, equal to $1 / T_c$. In order to describe a whole CPI, the number of chirps need to be incorporated into the mathematical model and we can redefine t as [22], [24].

$$t = nT_c + t_s \,, \qquad \text{where } 0 < t_s < T_c \tag{2.5}$$

where n is the index of a chirp and t_s is the time from the start of the n^{th} chirp for a particular ADC sample under study. Thus, Eq. (2.4) can be rewritten as

$$x_{tx}(t) = F\cos\left(2\pi\left(f_c(nT_c + t_s) + \frac{S}{2}{t_s}^2\right) + \varphi_0\right) \tag{2.6}$$

Figure 2.2 shows the attributes of the transmitted chirps.

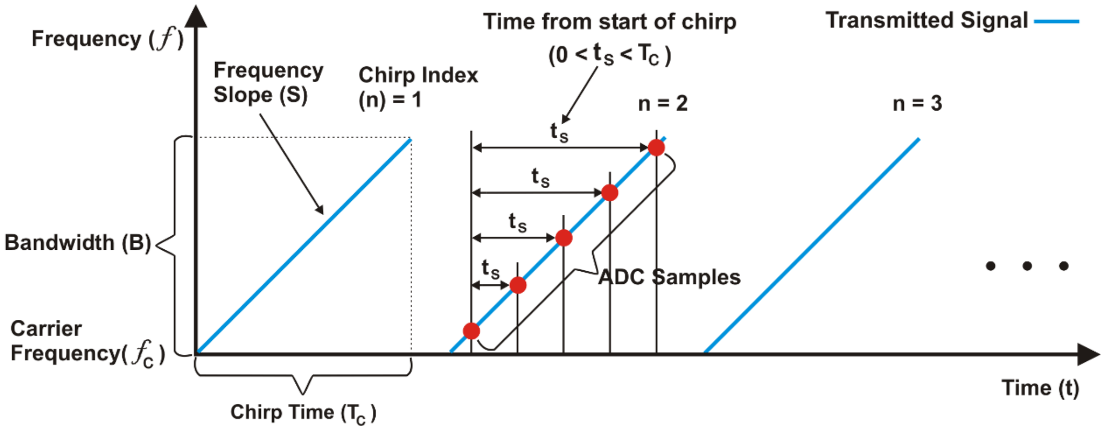

Figure 2.2 FMCW Radar Transmitted Chirps

The transmitted signal is received back by the radar after being reflected by the target. This received signal is obtained after a Round-trip Time of Flight (RTOF), τ, and with an attenuated amplitude, H and thus it is an attenuated and time-shifted copy of the transmitted signal. The received signal can be easily expressed as:

$$x_{rx}(t) = H\cos\left(2\pi\left(f_c(nT_c + t_s - \tau) + \frac{S}{2}(t_s - \tau)^2\right) + \varphi_0\right) \tag{2.7}$$

The attenuated amplitude H of the received signal mainly depends on the power attenuation with the 2-way travel distance, Radar Cross Section (RCS) of the target and receiver antenna gain. The RTOF, τ, for a stationary target is given by $\tau = 2R\ /\ c$, where R is range and c is speed of light.

Let us define the target velocity v as the first derivative of $R(t)$ so that $R(t) = R_0 + vt$, with a non-accelerated movement where R_0 is the initial range of the target from the radar. Then , we have :

$$\tau = \frac{2(R_0 + vt)}{c} = \frac{2(R_0 + v(nT_c + t_s))}{c} \tag{2.8}$$

The received signal is mixed with a copy of the transmitted signal in the FMCW I/Q mixer as shown in Figure 2.1. The output of the mixing operation of Figure 2.1, x_{mx}, is the result of a multiplication operation given by:

$$x_{mx}(t) = x_{tx}(t)x_{rx}(t) \tag{2.9}$$

In the case of inphase part of the mixing operation, the operation is governed by the simple trigonometric operation $\cos(\alpha)\cos(\beta) = 1\ /\ 2[\cos(\alpha + \beta) + \cos\ (\alpha - \beta)]$. By certain simplifications, substitution of τ from Eq. (2.8), considering that $v \ll c$ and thus ignoring high powers involving $v\ /\ c$, the simplified relation for the inphase part of the mixer output Eq. (2.9), can be obtained as

$$x_{mi}(t_s, n) = \frac{FH}{2}\cos\left(2\pi\left(\frac{2SR_0}{c}t_s + \frac{2f_c v}{c}nT_c\right) + \frac{4\pi f_c}{c}R_0\right) \tag{2.10}$$

Similarly, by using $\cos(\alpha)\sin(\beta) = 1\,/\,2[\sin(\alpha+\beta)+\sin(\alpha-\beta)]$, and substitutions and simplifications as done for Eq. (2.10), the following relation can be obtained for the quadrature part of the mixer output

$$x_{mq}(t_s, n) = \frac{FH}{2}\sin\left(2\pi\left(\frac{2SR_0}{c}t_s + \frac{2f_c v}{c}nT_c\right) + \frac{4\pi f_c}{c}R_0\right) \tag{2.11}$$

From Figure 2.1, the inphase and quadrature components of the IF I/Q mixer output are joined to form the complex baseband signal:

$$x_{mb}(t_s, n) = x_{mi}(t_s, n) + jx_{mq}(t_s, n) \tag{2.12}$$

where x_{mi} = inphase IF signal (real part of mixer output), x_{mq}= quadrature IF signal (imaginary part of mixer output), x_{mb} = complex (baseband) I/Q IF signal and j is the imaginary unit ($j = \sqrt{-1}$).

Figure 2.3 shows the general pictorial presentation of the transmitted and received chirps for a FMCW radar.

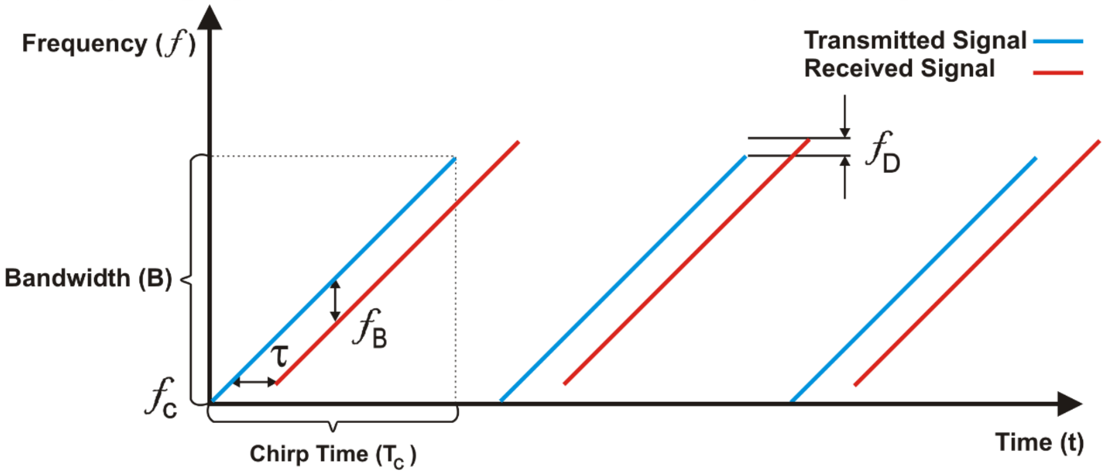

Figure 2.3 LFM Radar Tx-Rx Wave Model

As we can see, at any point in time between $t_s = \tau$ and T_c, there is a difference (f_B) in the frequency of the transmitted and received signals. A signal with this frequency (usually called beat frequency) will be extracted by the mixer operation. The f_B is composed of two parts, one due to the initial range R_0 and the other due to the velocity v. The velocity-related component can be seen as the Doppler shift (f_D) which is the motion-induced difference between the frequency of the transmitted and received signals. In the case of a stationary target, f_D will be zero and the received signal will be only a time shifted copy of the transmitted signal.

The signal processing in an FMCW radar is designed to provide the measurement of the f_B and then to separate its two components – this allows finally to calculate range R and velocity v of the target.

Note that Eq. (2.10), Eq. (2.11) and Eq. (2.12) are given as functions of two variables, i.e. t_s which is the time from the start of relevant chirp and n which is the chirp index. Thus, we can arrange the data in a matrix of two dimensions. The time-domain ADC sampled chirp data $x_{mb}(t_s)$ is attributed to one dimension of the radar data matrix, called “fast-time dimension”. The second dimension is the index n, that indicates which chirp the data comes from. This dimension is called the “slow-time dimension”, as it is incremented by a relatively large value of T_c. Some radars are built with many receive antennas distributed in space – then, a third (spatial) dimension is introduced and the data matrices are stacked to form a radar data cube. Interested reader may refer to [28] for a basic introduction to radar data cube; however the spatial dimension is not dealt with in this thesis, so only the fast-time and slow-time dimensions will be referred and used.

A joint look at Eq. (2.10), Eq. (2.11) and Eq. (2.12) shows that the complex beat signal can be interpreted as having three phase components each from the inphase and quadrature outputs of the mixer. By ignoring the trigonometric functions of the I/Q parts and other common factors, we can see that the first component is $(2SR_0/c)t_s$. The factor $2SR_0/c$ is the range frequency part of the beat frequency and its relevance to range is evident by the presence of R and by signal being sampled with t_s in this term. We can also see clearly that it will be visible along the fast time dimension (first dimension) of the radar data matrix. This part is the primary contributor to the range information. The second component of the phase term is $(2f_c\, v/c)nT_c$ and the presence of nT_c shows that it corresponds to the slow dimension (2nd dimension) of the radar data matrix. The factor $(2f_c\, v/c)$ is the Doppler frequency related to the target speed and it is evident from the presence of v term in this expression. The third part is a constant phase term of the form $(4\pi f_c/c)R_0$ and it is not much useful.

Typically (however not always), the radar parameters and target scenario are such that the range frequency is larger than the Doppler frequency. From a strictly range point of view, the non-zero Doppler frequency introduces an error into the range measurement, but in a typical scenario, this error is small and can be neglected [24]. On the other hand, targets with different Doppler frequencies can be distinguished when the slow time dimension of the radar matrix is processed.

CHAPTER 3

EXPLORING THE POTENTIAL OF 77 GHz COTS AUTOMOITVE RADAR FOR RCS MEASUREMENT OF 9 mm BULLET MODEL

During the initial stages of the research phase, it was planned to use a 9 mm pistol to generate velocity of ~300 m/s (0.9 Mach) as it seemed to be rather convenient from logistics and practical point of view. This decision naturally called for determining if the at-hand COTS FMCW mmwave automotive radar was capable of detecting the 9 mm bullet. This exploratory study led to the findings submitted in this chapter.

Radar Cross Section (RCS) is the basic property of an object which determines its detection by a radar. Research on RCS of various bullets used in different weapons has been very rarely reported publicly. Possible underlying reasons could be patronage of such programs by the government institutions and the allied confidentiality aspects. This seems natural for assault rifles and sniper rifles etc. However, given the increase in prevalence of asymmetric warfare and requirements of neighbourhood safety especially in the urban settings, there is a huge potential for research and use of COTS mmwave radars for detection of bullets fired from small arms. Such studies could lay foundations for development of practical, cost effective, field deployable, Hostile Fire Indication (HFI) systems by the industry, academia and government research institutions alike.

[29] and [30] are some examples of studies on RCS measurements of small arms and assault rifles bullet models in 1.5 GHz ~ 5 GHz and 32.4 GHz ~ 35.6 GHz frequency. [31] reports simulation studies for RCS measurements of rockets and artillery rounds at 1.5 GHz ~ 9.5GHz frequency range. It is interesting to note that such studies have been both a legacy and are rare as well. [32] reports a study three decades ago for the parameters’ determination of space debris with 4 mm to 80 mm dimension with a radar frequency of 35 GHz with 20 kW power at a range of 25 km. At the same time, [33] reports use of 35 GHz and 94 GHz frequency for detection of tanks etc. A

relatively recent study reports use of 32-36 GHz and 90-95 GHz frequencies for detection of foreign objects on the runway by Synthetic Imaging Radar (SAR) [34]. However, one point common in all these studies is the use of bulky custom-built radar systems instead of available COTS systems.

This chapter describes measurement of RCS variation against aspect angle for a 9 mm (9.3 mm×14.8 mm) pristine (not fired from the gun) bullet (projectile) model. 9 mm is a fairly common calibre for small arms and handguns.

This chapter is intended to indicate a thus far unexplored area of applied research and development to the application and system engineers and researchers from broad engineering backgrounds. This intent, coupled with unavailability of anechoic chamber and Vector Network Analyzer (VNA) in the required mmwave frequency range, prompted the author to undertake this activity and report it for the broader audience so that it can be realised that expensive RF laboratories and infrastructure is not essentially required in order to realize systems with practical utilization from the COTS mmwave radar systems or to carry out basic studies at least.

3.1 RCS Measurement Setup

As stated above, a 9 mm bullet model was selected for this study. The bullet model was machined from general purpose Aluminium as per nominal dimensions in Figure 3.1. A commercially available COTS FMCW mmwave automotive radar hardware platform was used for taking the RCS measurements. This FMCW radar mmwave Integrated Circuit (MMIC) system operated in 77 GHz to 81 GHz frequency range. A standard laboratory room at the university was used for this experiment; the bullet model was suspended and RCS measurements were taken with 10 degree increments over the 360 degrees. The measurements have not been taken in an anechoic chamber and without a turntable. Figure 3.2 shows the suspended bullet.

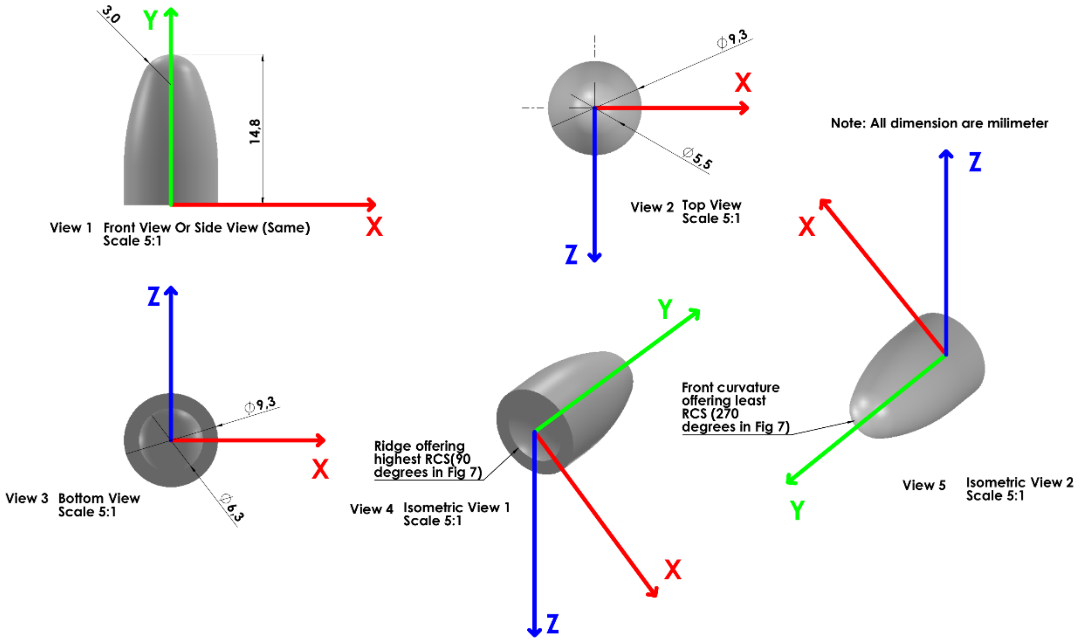

Figure 3.1 Solid model views and major dimensions of the bullet model

Figure 3.2 Suspended 9 mm bullet model for RCS measurement

IEEE Std 1502-2007 [35] is the current applicable version of a document for RCS measurements which is a comprehensive source even for new entrants in this field. The usual practice for RCS measurement is the use of VNA for collection of frequency domain data and conversion of this data into time domain data by IFFT [35, 36]. However, this thesis study used the complex Inphase-Quadrature (I/Q) data at

Intermediate Frequency (IF) stage from the built-in 16-bit analog to digital converter (ADC) in COTS radar transceiver chip. During the offline post processing, this data was used to build the radar data cube and the 256-point FFT was obtained against the fast-time dimension to calculate the range profile [28]. No zero-padding and no truncation was used in the FFT.

RCS (σ) is defined as the ratio of power backscattered by the target to the power incident on the target which can be written as [27], [37] :

$$\sigma = 4\pi \lim_{\mathrm{R}\to\infty} \left(R^2 \frac{P^{scat}}{P^{inc}} \right) \tag{3.1}$$

where R is the range of target from the radar, P^{inc} is the power incident on the target and P^{scat} is the power scatterered after reflection from the target. The power or intensity of an electromagnetic (EM) wave is proportional to the square of its electric or magnetic field magnitude. Therefore, Eq. (3.1) is widely written as [37], [38] :

$$\sigma = 4\pi \lim_{R\to\infty} \left(R^2 \frac{|E^b|^2}{|E^t|^2} \right) \tag{3.2}$$

where E^b and E^t are the backscattered and transmitted complex magnitudes of electric fields respectively. RCS is usually shown in unis of dBsm. The above equation gives the absolute RCS. However, for this study in particular and for radar applications in general, it is the calibrated (detectable) RCS that is more useful and important vis-á-vis the hardware specifications of the system.

An Aluminium sphere of 15 mm diameter was machined and then used as reference target in this study where the diameter of the sphere corresponds to the biggest dimension (length) of the bullet model.

The salient general parameters of the used hardware configuration were: bandwidth (B) of FMCW chirp = 4 GHz, frequency slope (S) of chirp = 67 MHz/us, ADC samples/chirp = 256, sampling rate (F_s) = 5209 ksps and number of chirps =128.

As the experiment was conducted in a laboratory room instead of an anechoic chamber, so the presence of reflections from the walls, roof and floor and their interactions were natural. In view of this, the bullet model was selected to be placed at (an optimal) distance of 76 cm from the radar and it fulfilled the far field requirement as well.

3.2 Simulation and Measurement Results

The bullet model was roll-symmetric about y-axis while the rotation about x-axis would not alter the area facing the radar beam. Therefore, it was decided to study the aspect angle variations by rotation of bullet model about the z-axis only (refer Figure 3.1). The combination of angle variations in all three axes was neither feasible considering the available resources nor it was deemed to be of much significance as in that case the bullet area facing the radar would be more than the bullet area considered in aspect angle variations due to rotation about the z-axis only. Therefore, the aspect angle variation by rotation about z-axis only presented the worst case scenario for RCS measurement.

The suspended bullet model was rotated in increments of 10 degrees from 0 to 360 degrees; three readings for radar data cube were taken at each single angle position and average of these complex magnitudes was used to calculate the range profile. The 15 mm diameter Aluminium reference sphere was suspended in the same setup at the same position and measurements for its RCS were taken by the same method as used for the bullet model. Figure 3.3 shows the actual bullet model and the 15 mm sphere used for measuring the calibrated RCS.

Figure 3.3 Bullet model and 15 mm sphere (holes for suspension threads visible) Top view and 45° angle view (from rear side)

The particular hardware platform used provided the complex I/Q data at Intermediate Frequency (IF) of the FMCW transceiver. Mostly, I/Q data at the IF stage is available from the radar front end and this is from where the further signal processing starts. Then, this stage is usually where the end user has the flexibility to implement its own algorithms and signal processing.

3.2.1 Concept of Relative Calibration

A study was made for the reference sphere. The theoretical RCS of a sphere with radius r is defined in dBsm as $10\log\,(\pi r^2)$ which gives a value of -37.5 dBsm for a sphere of 15 mm diameter. CST Studio Suite from Dassault Systems was used for obtaining the RCS of required objects by simulation. It provided RCS of -37.2 dBsm for the 15 mm diameter sphere at the selected frequency of 79 GHz.

Subsequently, the complex I/Q IF data was attempted to determine the RCS of reference sphere. The complex I/Q IF data was acquired and subjected to FFT processing for the reference sphere echo while the transmitted power was 17 mW. Using these, the RCS value of 95 dBsm was obtained by using Eq. (3.2). However, this value does not match the theoretical and simulation value of -37 dBsm because Eq. (3.2) uses only the magnitudes of the scattered and transmitted electric fields. These values can be readily measured during standard RCS measurement as discussed earlier in section 3.1. However, in case of common FMCW COTS systems, the backscattered echo undergoes several additional processes including amplification (LNA), mixing with the Local Oscillator (LO) frequency, conversion to IF and finally digitization by the ADC (all inside the chipset). During all this process, although the information about the range and velocity is retained, the magnitude of the original backscattered echo received at the radar undergoes significant changes in the magnitude before it is available to the end user as output of ADC and in the form of I/Q IF data. Therefore, the true value of RCS will not be obtainable by use of Eq. (3.2). In this case, the concept of relative calibration becomes handy which defines the calibrated RCS of a target as:

$$\text{RCS} = \left(\frac{(\text{Magnitude of target echo})^2}{(\text{Magnitude of reference target echo})^2}\right) \times \text{Theoretical RCS of reference target} \tag{3.3}$$

Eq. (3.3) can be written as Eq. (3.4) for RCS in dBsm units:

$$\sigma = 10\log\frac{|E_t|^2}{|E_0|^2} + \sigma_0 \tag{3.4}$$

where E_t and E_0 are measured echoes of the target and reference target (sphere) respectively and σ_0 is the theoretically calculated RCS (in dBsm units) of the reference target (sphere) [39]. The operation of Eq. (3.3) and Eq. (3.4) takes care of all the magnitude conversions during various stages of signal conditioning and signal processing and proves to be a very useful tool in this case of somewhat non-conventional RCS measurement.

3.2.2 Selection of Frequency for Simulation

It was planned to use the bandwidth of 4 GHz with starting frequency of 77 GHz for this RCS study, therefore, a simulation study was carried out for finding the RCS of the 15 mm diameter reference sphere and the bullet model at 90 degree and at 270 degree. As it will be discussed further, the bullet model gave strongest reflection at 90 degree while it gave weakest reflection at 270 degree orientation. The RCS was simulated for these three target models for frequency sweep of 77 GHz to 81 GHz with the interval of 200 Hz. Figure 3.4 shows the results of these simulations which show that the simulated RCS of three target types with different orientations remains almost constant over the frequency range of 77 GHz to 81 GHz. Due to this reason, the RCS of bullet model was simulated at the average frequency of 79 GHz and then it was compared with the experimentally measured results.

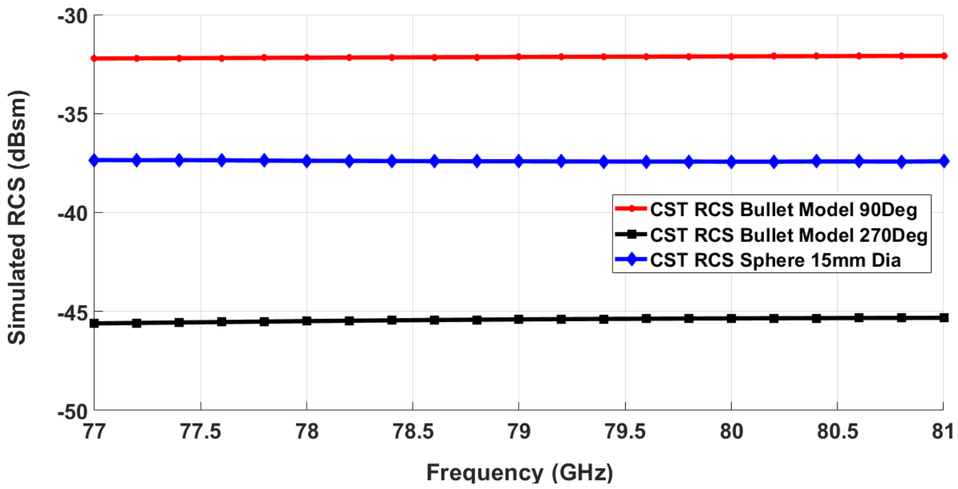

Figure 3.4 CST simulated RCS against frequency sweep for bullet model and reference sphere

3.2.3 Results of RCS Measurement Experiment

RCS measurements were taken for all the angle positions as discussed earlier. Figure 3.5 shows the range profile for the bullet model at 100 degrees as a representative case where peak at 0.76 m corresponds to the bullet model and y-axis shows the calibrated RCS calculated by using Eq. (3.4) above.

Antenna coupling at close ranges is a well-known phenomenon in FMCW radar which is evident in Figure 3.5 also. On the other hand, increasing the distance decreases the signal strength of the received signal. In view of these, 0.76 m is somewhat an optimized distance for the bullet placement.

Figure 3.6 depicts results at 180 degrees as another example. Furthermore, it is natural to expect and have stronger echo signals from distant objects or nearby objects with RCS much greater than the Unit Under Test (UUT); bullet model in this case. Range gating is usually done in RCS measurement in order to show / acquire data only from the range position of interest [35]. Range gating was carried out in this activity to limit the observation range to 3 meters. Reflections from roof, floor and walls are naturally present in indoor environment and they may interfere constructively at some range bins. Figure 3.6 shows the echo from such interference and it has been purposefully not removed by range gating to show the real scenario. (Figure 3.5 and Figure 3.6 may be studied jointly for various range plot features description).

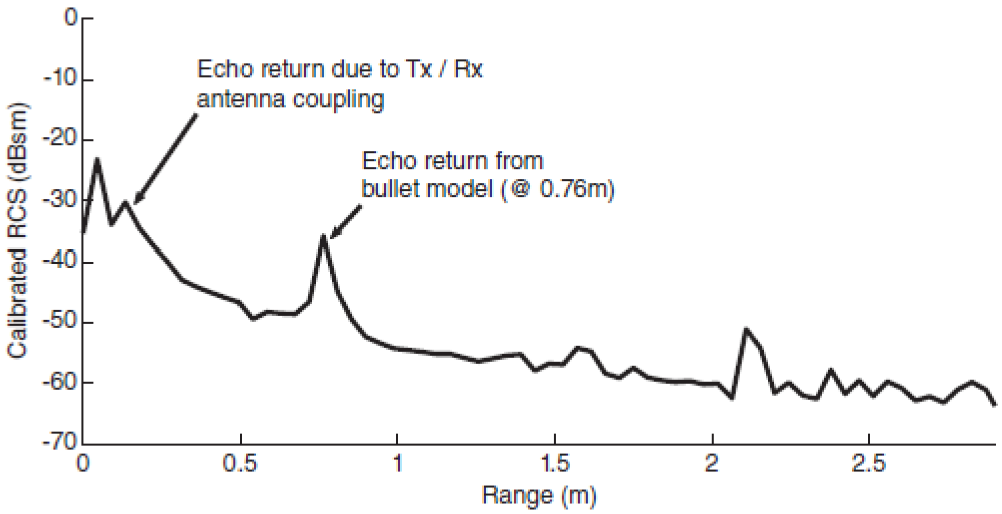

Figure 3.5 Range profile showing calibrated RCS for bullet model at 100° position

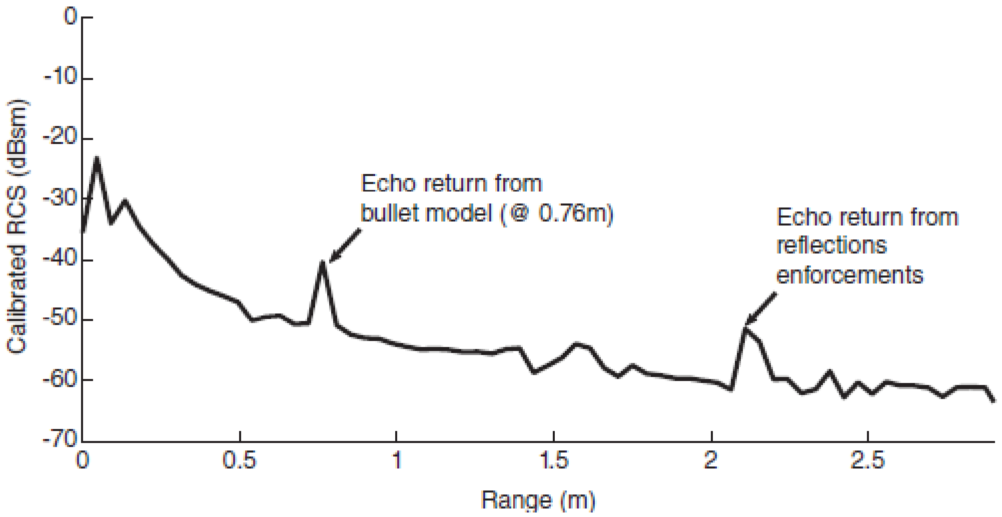

Figure 3.6 Range profile showing calibrated RCS for bullet model at 180° position

As the target was almost always consistently present in the same range bin, therefore, the same range bin was used to extract the magnitude of echo, irrespective that the echo was visually discernible or not. The measured calibrated RCS against the aspect angles (along with symbolic bullet orientations) is plotted in Figure 3.7. The simulation results for the same bullet model were obtained using CST Studio Suite and are shown along with the measured results.

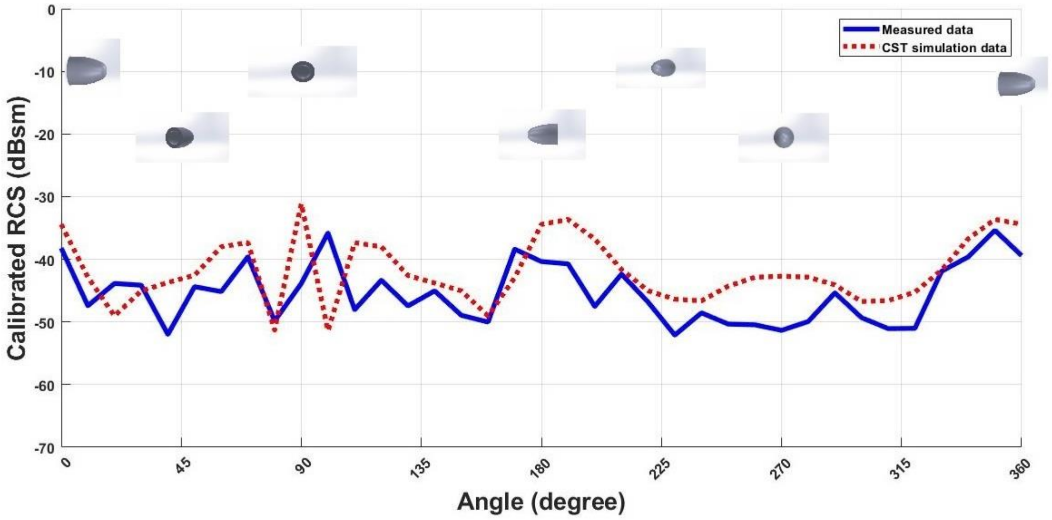

Figure 3.7 Comparison of measured and simulated results for calibrated RCS variation against the bullet model aspect angle

3.3 Discussion

No windowing technique was applied and no curve fitting was carried out. It was deliberately done to present the data in its raw and direct form so that readers become aware of the possible challenges. Moreover, the precise drilling of suspension holes in the bullet model was not possible in the university level workshops. This, coupled with lack of precise positioning system, resulted in some lateral offsets at some angular positions between the measured and the simulation data. The dBsm levels were permissible to vary among two plots as CST calculates the absolute RCS while the calibrated RCS was measured experimentally which was naturally very much hardware platform dependent. However, it is evident that the overall shape as well as the levels of both graphs fairly match each other given the possible sources of errors/offsets and sub-optimal availability of the facilities. Nonetheless, the matching of two patterns is more important than matching of dBsm levels.

Owing to the peculiar structure of the bullet and the model extent (length), the calibrated RCS is significant when the bullet is lateral to the radar (0 degrees and 180 degrees) and when it is traversing away from the radar (90 degrees) (refer Figure 3.1 and Figure 3.7). Although the area posed by the bullet at 90 degrees is less than the area posed at 0 degree and 180 degree, however, as expected, the ridge visible at 90 degree position contributes significantly to the RCS due to its discontinuous nature.

The bullet poses least RCS when facing the radar (270 degree) and at about 45 degree in 3rd and 4th quadrants. This could be one of the major challenges for adopting use of 77 GHz COTS FMCW systems for RCS measurement of 9 mm bullet. There are techniques to address such situations however they are not a topic of this thesis. However, for these aspect angles, the parameters of various different available COTS systems might be evaluated to increase the measured/detected RCS reasonably well above the noise level.

As mentioned above, a ‘pristine’ bullet (projectile) model was used for this study which was smooth and did not have grooves and edges that would be actually present on the body of the bullet fired from a firearm. [36] reports a study for determination of RCS of cylinders in terahertz frequency range. The RCS was evaluated as a function of surface smoothness and it was found, as expected, that observed RCS increased as surface roughness increased. This brings encouragement that the actually fired bullets will have greater RCS due to their rougher surface as compared to the pristine bullet model in this case in this frequency range. This is expected to partially circumvent and overcome the challenge of the relatively feeble echo returns at certain aspect angles of the pristine bullet model.

Another important aspect that warrants attention here is that considering the two major dimensions (i.e. diameter (9 mm) and length (14.7 mm) of the bullet model), which are comparable to the nominal wavelength (λ) 4 mm (approx.) of the radar frequency, the RCS lies in the Mie resonance region which is not a preferred choice for the radar developers who tend to base their systems in the optical region where the target extent is much larger than the radar operating wavelength [27]. In the same background, [40] introduces such a HFI system in 240 GHz frequency range. However, such high frequency systems are both difficult and expensive to develop and build. It brings hope and encouragement to observe that the available COTS systems in 77 GHz to 81 GHz frequency range are able to both detect the discussed 9 mm bullet model and can also discern its aspect angle based on calibrated RCS measurements.

3.4 Conclusive Remarks for RCS Study

This chapter presents the results of an applied study for the calibrated RCS measurement of a 9 mm bullet (projectile) model by using commercially available COTS mmwave FMCW radar transceiver MMIC; this bullet type, mmwave frequency and application concept has not been thus far studied and reported in literature. The aim is to present the results in the particular frequency range; the available COTS systems from various OEMs are expected to possess comparable parameters.

The study identifies both the potentials as well as the challenges likely to be faced while endeavouring development of HFI systems by employing such systems along with possible ways to address such challenges.

This study explored use of low-cost COTS system for measuring RCS at that difficult band of 77 GHz ~ 81GHz. This may motivate interested individuals/entities to try to measures (at acceptable accuracy before anechoic chamber measurements) RCS of similar small-size objects by using such low-cost COTS platforms. This is one of the critical contributions that has been endeavoured to demonstrate in this work. Outdoor measurements could give better results, especially the possible lowering of noise level and possible removal of interferences, however, they have their own allied environmental limitations. For precise measurements though, use of anechoic chambers is imperative.

CHAPTER 4

LINEAR INTERPOLATION OF COMPLEX MAGNITUDE FOR RESOLVING PHASE ANGLE AMBIGUITY

Phase angle of a complex number is an important topic in Complex Number Theory. It has immense importance in a multitude of sensors used in physical sciences fields including but not limited to acoustics, Synthetic Aperture Radar (SAR) interferometry (including contour mapping), optics (including optical interferometry), seismic processing, inphase-quadrature (I/Q) architectures including Frequency Modulated Continuous Wave (FMCW) radar, digital signal processing, digital image processing (including medical image processing e.g. MRI), radio astronomy, just to name a few.

Phase retrieval is a closely related topic in applied mathematics which involves usage in many of above mentioned fields with probably most important use in diffraction imaging; it involves recovering (lost) phase information from the intensity (magnitude) of some transform, of which Fourier Transform is most widely used [41].

In other sensor applications, particularly the radar applications and optical coherence tomography (OCT) [42], it is more convenient and technically possible to have I/Q architectures. The I/Q architectures enable the provision of baseband complex signal and thus enable extraction of phase information directly from the imaginary and real parts of the complex number (instead of attempting phase retrieval form magnitude only as discussed in [41]).

Phase is a delicate physical quantity which is quite prone to noise present in the real world. However, in spite of its greater susceptibility to noise as compared to the magnitude of a complex number, the phase angle of a complex number is widely used for accurate measurements of very small displacements and velocities, especially in radar engineering. Indeed, there are also instances where phase angle change is used for measurement of relatively higher speeds [43]. The ability of phase angle to provide information about very fine displacements prompts its widespread use in healthcare applications involving human respiration and breathing movement detection / measurement [44]. Phase angle changes find extensive use in SAR interferometry [45] for terrain mapping, for example. Phase angle measurement is the cornerstone for finding Direction of Arrival (DoA) with multiple antennas in radar engineering [46], [47]. Quite often, in range measurements with (FMCW) radar, a coarse range measurement is made with the beat frequency and then a narrower fine measurement is made by using phase change for range calculation; various diverse tools are the topic of contemporary research in this area as exemplified in [48], [49] and [50]. However, the phase angle can only be measured unambiguously within the 2π radians [45], [48], [49], [50] and [51]. On the other hand, it is natural and logical that phase excursions beyond 2π do exist in nature in the physical phenomena. Therefore, a definite need exists to resolve this ambiguity beyond 2π limitation. In most of the cases, whether it is phase angle determination for velocity determination (for example [43]), or if it is phase angle determination for terrain mapping (for example [52]), or if it is optical interferometry (for example [53]), or if it is for very fine range measurements (for example [48], [49] and [50]), almost always, two things are common in all such instances. One that the unambiguous phase angle and resultant range / speed measurement interval is limited to 2π phase change. Second, that in case of essential ambiguity of phase angle beyond 2π, the phase unwrapping algorithms are used.

It is pertinent to summarily mention here that most of the works reported for use of phase for range and velocity measurement in (FMCW) radars do not attempt to resolve the basic inherent phase ambiguity but rather concentrate on various phase unwrapping techniques. On the other hand, while trying to address phase ambiguity issues in DoA problems (for example [46], [47]), again, resolution of phase ambiguity is not much attempted and other methods / algorithms are used to rather circumvent this issue. It can be stated, though with caution, that attempts to resolve the phase ambiguity at the very basic and origin level, have not been much reported in the literature.

This chapter presents an applied technique to resolve the phase angle ambiguity of the complex numbers and involves a relatively novel pragmatic approach which has not been explored so far, to the knowledge of the authors.

The method alleviates the need for the use of phase unwrapping algorithms and provides unambiguous phase measurement beyond the 2π limit imposed by the arc tangent (arctan) function on phase angle. The author came across this idea when trying to resolve the phase ambiguity for velocity measurement in a field experiment with the COTS mmwave FMCW radar. The mathematical bases of the idea are unexplored so far but they are based on simple, straight forward and well-established physical and mathematical aspect of the magnitude and phase angle of complex numbers. The method is further explained with an application example of velocity measurement by use of a FMCW radar. As it is a first application attempt of a nascent idea, therefore the application example has certain significant constraints and limitations which are summarized in section 4.3.2 and section 4.4. The application example is a one limited use case pertaining to the research area of the authors and researchers / practitioners in similar or other mathematical / physical sciences / sensing technology fields may possibly consider exploring the suitability and applicability of this method in their own specialized domains because the method is intrinsically based upon the relation between the magnitudes and angles of complex numbers.

The forth coming sections of this chapter explain the theoretical basis of the proposed method for resolving phase angle ambiguity based on complex magnitude interpolation. The method is further explained graphically, and then with a pseudo code and allied elaboration. Subsequent to that, the method is applied and demonstrated with simulation and with a real time experiment by use of a FMCW radar. The phase difference between two consecutive sampled complex numbers of I/Q IF signal is practically measured unambiguously for up to $\sim 12\pi$ radians (much beyond 2π unambiguous limit). This extended unambiguous measured phase change is then used to measure the velocity that is up to ~12 times the velocity that could be otherwise measured unambiguously. The proposed method is not a phase unwrapping algorithm but it will emancipate the need of such algorithms, provided that the limitations of the method are overcome.

4.1 Theoretical Basis of The Phase Interpolation Technique

4.1.1 Phase Angle of a Complex Number

The (instantaneous) phase angle of any complex number ($x = a + jb$) (j being the imaginary unit ($j = \sqrt{-1}$)), is calculated by the arctan function which is given by [54]

$$\text{phase}_{inst}(\emptyset) = \arctan \frac{\text{imaginary part } (b)}{\text{real part } (a)} \tag{4.1}$$

A peculiar observation about the above famous simple definition of phase angle is that no matter what could be the (relative) magnitudes of real and imaginary parts of the relevant complex number (i.e. ($a, b \in \mathbb{R}$)), the arctan will always give a value in the open interval, $\emptyset \in \left(-{}^{\pi}/_{2}, {}^{\pi}/_{2}\right)$ radians (rad). When the phase difference between two complex numbers exceeds ${}^{\pi}/_{2}$, 2π ambiguity occurs. The mathematicians more commonly use the convention of phase angle interval as $\emptyset \in \left(-{}^{\pi}/_{2}, {}^{\pi}/_{2}\right)$. However, most computer programs used in the applied scientific fields, in contrast to the convention used by the mathematicians, further convert this range into either symmetrical $(-\pi, \pi)$ open interval, or one sided $(0, 2\pi)$ open interval. That is the reason that we often come across different notations for the unambiguous phase angle interval, for example $(0, 2\pi)$ [55], $(-\pi, \pi)$ [46], [51], $(0, \pi)$ (single-sided) [43] and modulo 2π [47], [52], [56]. All these intervals are in fact different manifestations of the principal unambiguous interval of range of arctan function. The general nature of a complex number is explained via Figure 4.1 (reproduce with persmission from [57]).

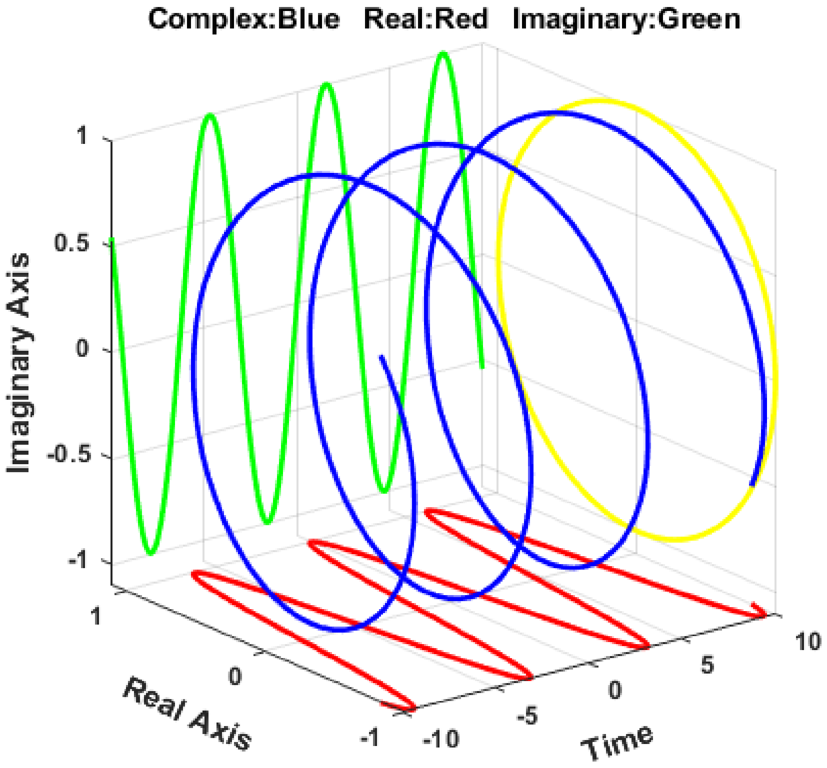

Figure 4.1 The complex number and its parts

Eq. (4.1) gives the phase angle of the complex exponential in Figure 4.1 by using the arctan function which is a multivalued function, with the principal value of phase angle lying in the interval $(0\,,2\pi)$, as discussed above. The general values of arctan (including the principal value and values outside the principal value interval) are given by

$$\varphi = \varphi_{principal} + 2\pi k \quad | \quad k \in \mathbb{Z} \tag{4.2}$$

As per elementary wave theory, the instantaneous phase angle of a wave changes by 2π rad when the wave travels a distance equal to one wavelength (λ) [44], [58] and this phase is uniformly distributed over the $(0, 2\pi)$ interval [55]. This implies that the distance travelled by a wave can be estimated if the phase change can be measured (and vice versa), which is one of the basic principles used in displacement measurement in radar theory and in optical and microwave interferometry. However, as mentioned earlier, it puts a very severe limit of < 2π rad before the phase measurement becomes ambiguous.

4.1.2 2π Phase angle: A Limitation of Mathematics, Not Present in The Nature

Considering $(0\,, 2\pi)$ interval (which is just another manifestation of $(-\pi,\ \pi)$ interval representation), it is evident that the maximum difference between the (instantaneous) phase of any two (possibly consecutive) complex numbers will be (|2π| + |2π|) < 4π (< 4π because the open interval $(0\,, 2\pi)$ does not include the endpoint 2π). However, it is a logical, natural and self-evident fact that the phase difference between any two consecutive complex numbers representing any mathematical / physical quantity is not necessarily limited to 4π. This is basically a limitation of the mathematics and not a limitation that exists in nature itself.

One of the possible ways to circumvent 2π phase ambiguity is to use more samples between the two relevant complex numbers and then to use some phase unwrapping algorithm, as mentioned earlier. However, there might be practical limitations to incorporate additional samples between the two relevant complex numbers. In addition, the phase unwrapping algorithms have their own constraints which are not discussed here. Nonetheless, the fact remains that although the phase unwrapping techniques can produce phase difference values of more than 4π by progressively building upon the instantaneous phases of more than two successive complex numbers, however, there seems no way to resolve the phase ambiguity between two consecutive complex numbers.

The important impediment is that the phase difference will be limited to a maximum value of < 4π, irrespective if the incumbent mathematical / physical phenomenon was producing a phase difference (much) larger than 4π between two complex numbers.

4.1.3 The Proposed Method to Resolve Phase Ambiguity

Figure 4.2 explains the basic concept of the method being proposed to determine the phase angle of complex number(s) by linear interpolation of the magnitude of complex number(s). A, B and C are the complex numbers used in the depiction.

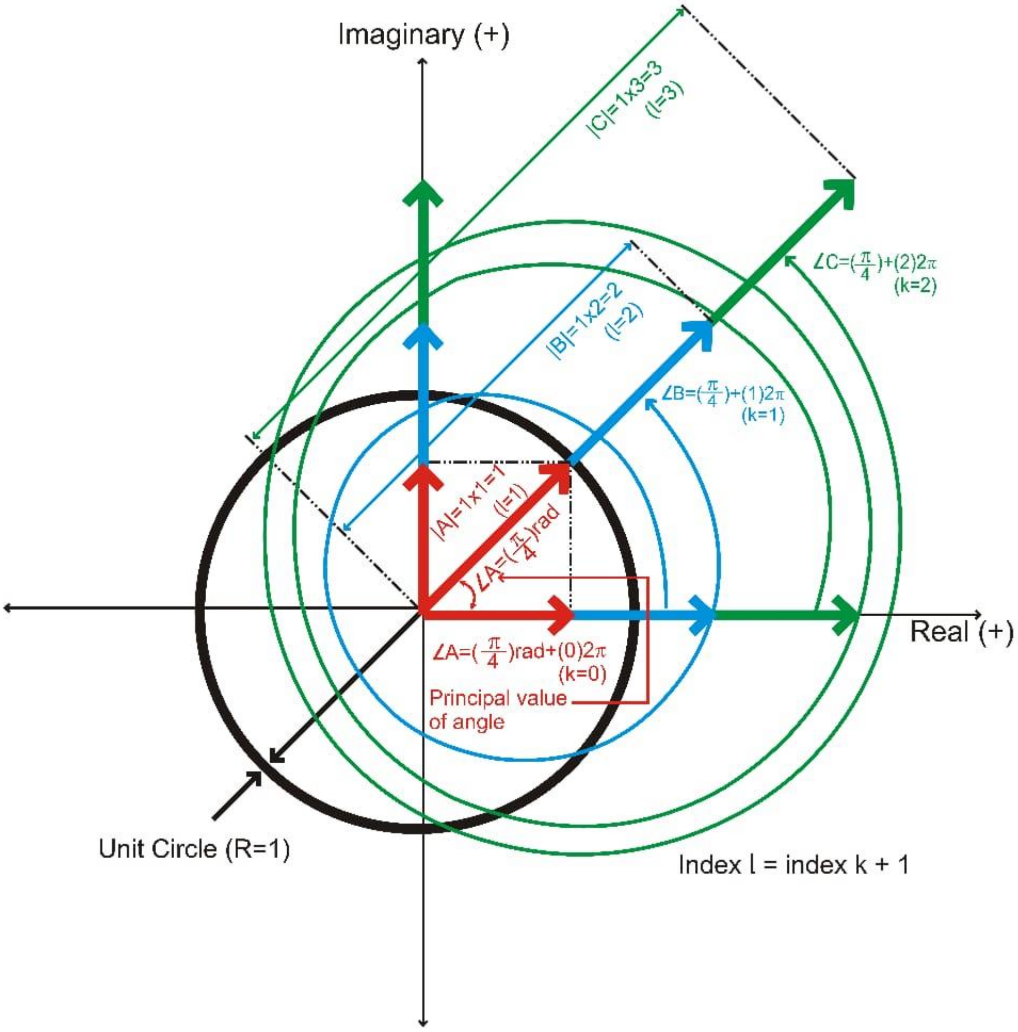

Figure 4.2 Graphical depiction of the idea to resolve phase angle ambiguity of complex numbers by magnitude interpolation

Figure 4.2 suggests that it is reasonable to assume that the phase of a complex number (or complex exponential/logarithm) completes one revolution (equal to one λ distance) and the phase *changes* by 2π rad, when the magnitude of the complex number ($|x|$) is *increased* (or *decreased*) linearly, by an amount equal to magnitude of complex number at the unit circle. Mathematically, it is straightforward to write for the complex number $x = a + jb$:

$$|a|_l = l \times |a|_{unit\ circle} \quad | \quad l = k + 1 \tag{4.3a}$$

$$|b|_l = l \times |b|_{unit\ circle} \quad | \quad l = k + 1 \tag{4.3b}$$

$$|x|_l = l \times |x|_{unit\ circle} \quad | \quad l = k + 1 \tag{4.3c}$$

It implies that finding the number of discrete magnitude steps between the magnitudes of two complex numbers, enables the estimation of the phase difference between any two complex numbers. Note that each such discrete step corresponds to travel of wave equal to one λ. The estimation of phase difference in this manner emancipates the process from the inherent ambiguity beyond 2π phase limit.

The concept is further explained with Figure 4.3 which shows the comparison between conventional 2π constrained phase angle processing (Figure 4.3(a)) and proposed method (Figure 4.3(b)) for the three assumed complex numbers, L, M and N. Figure 4.3 (a) shows that whatever might be relative magnitude of complex numbers in conventional processing, the phase difference between two complex number cannot exceed 2π. Figure 4.3 (b) depicts the interpolation of magnitude between two complex numbers relative to unit circle magnitude. The phase angle is also accordingly interpolated. Figure 4.3 (b) explains that given that we have two complex numbers, say , L and N, the magnitude between these two complex numbers can be *"interpolated"* in the form of *'quantized' steps*. Each such quantized step refers to one revolution of phase angle (one λ distance). By such interpolation, we are able to obtain a phase difference of 12π in this demonstration, between L and N, whereas by conventional methods, we would have phase ambiguity beyond 2π phase difference

Corollary # 1: The complex numbers L and N, can very conveniently be two consecutive sampled complex numbers obtained from a sensor for any natural/physical phenomena, still they can have virtually unlimited phase angle difference between them, as opposed to facing 2π phase ambiguity limit by conventional methods.

Corollary # 2 : The demonstration in Figure 4.3 is based on increasing magnitude. The same approach can be applied to decreasing magnitude as well where the magnitude is decremented linearly from a reference magnitude.

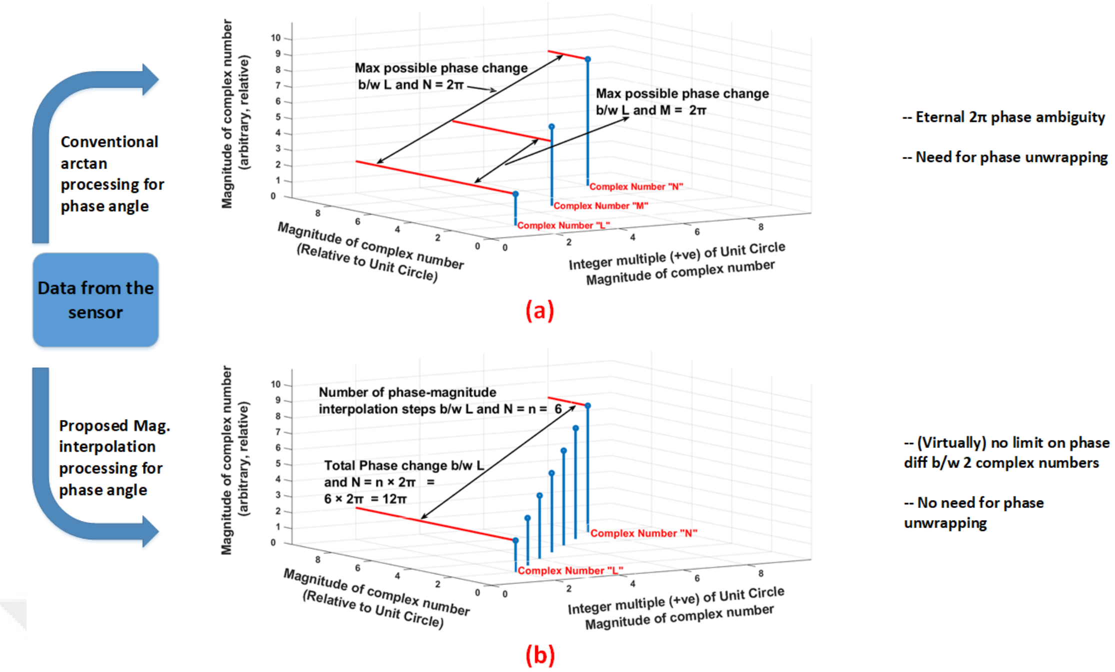

Figure 4.3 Interpolation of Complex Magnitude and Phase Angle

The above proposed method is further elaborated with the following pseudocode:

Pseudocode 1: Interpolation of complex number magnitude to resolve phase ambiguity

---

```
Input:
        Consecutive sampled complex numbers, $x_i = \{x_1, x_2, x_3, \ldots\ldots, x_i\}$
        Physical quantity $y_i \;\; | \;\; x_i \longrightarrow y_i$

Procedure:
        Magnitude, $A_i = \mathrm{abs}(x_i)$
        for the $A_i, (i = 1, 2, \ldots, i-1)$, do
            | if $A_i < A_{i+1}$
            |   Direction of Interpolation (DoI) = +ve
            | else if $A_i > A_{i+1}$
            |   Direction of Interpolation (DoI) = -ve
            | end
        end
        Physical quantity corresponding to 2π phase difference, $y_{2\pi} = y(y_1, \varphi_{2\pi})$
        Magnitude 2π, $A_{2\pi} = A(y_1, A_1, y_{2\pi})$
        for the $x_i, (i = 1, 2, \ldots, i-1)$, do
```

```
    Pick $A_i$
    Initialize Counter, Ctr = 0
    Set $A_{ctr} = A_i$
    repeat
        $A_{ctr} = A_i + A_{2\pi}$   ( if DoI = +ve )
        $A_{ctr} = A_i - A_{2\pi}$   ( if DoI = -ve )
        Increment Ctr
    until  $A_{ctr} < A_{i+1}$     ( if DoI = +ve )
           $A_{ctr} > A_{i+1}$     ( if DoI = -ve )
    Ctr = Ctr - 1
    $Phase(x_i, x_{i+1}), \varphi_m = \varphi(x_i) + (2\pi \times Ctr) + \varphi(x_{i+1})$
    reset Ctr⟶ 0
end
```

Output:

Vector of phase values (not constrained by 2π limit), $\varphi_m = \{\varphi_1, \varphi_2, \varphi_3, \ldots\ldots, \varphi_{i-1}\}$

The above pseudo code is almost self-explanatory, however, a few points need elaboration and emphasis here. The conversion of the complex number x_i to the physical quantity y_i, is a technology and field specific step for the particular physical phenomenon. A priori knowledge of this parameter is needed as input to the Pseudocode 1 and this will be governed by the relevant equations governing the particular physical phenomenon. This will be a critical step when implementation of this proposed phase interpolation method will be possibly attempted in other fields by the interested researchers. For example, in case of a FMCW radar, x_i could denote the beat frequency after conversion of time-domain IF I/Q sampled data to frequency domain by Fast Fourier Transform (FFT). This frequency is further converted to the target range as the physical parameter (y_i) for meaningful observation. In some other field, for example in image processing, the complex number x_i could be mapped to grey scale intensity y_i. This aspect will be briefly discussed further in section 4.4.4 about application in other fields.

$A_{2\pi}$ is the magnitude change which is a function of the reference physical quantity y_1, the magnitude A_1 mapped to the reference physical quantity y_1 and $y_{2\pi}$ the physical quantity corresponding to phase change of 2π. Thus, $A_{2\pi}$ corresponds to the physical quantity $y_{2\pi}$, in a mapping relationship with y_1 and A_1.

In Figure 4.3, for example, y_1(not shown) will be the physical quantity corresponding to magnitude of complex number L (A_1), $A_{2\pi}$ is the change (from A_1) in magnitude when y_1 changes corresponding to 2π phase change. (Here, it is accomplished by increasing the magnitude of real and complex parts by increments equal to their magnitudes at the unit circle.) Then, A_1 increases in 6 incremental steps, each step *change* being equal to $A_{2\pi}$, to reach magnitude of complex number N. Thus, we obtain a phase difference of 12π between consecutive complex numbers L and N.

The decay or increment of the magnitude is determined to decide about direction of interpolation. However, it is not trivial to note here that the method mainly works on change in phase and is relatively independent of direction of interpolation. It is further possible that there might not be a uniform increasing or decreasing trend of change in magnitude (A_i) for the determination of direction of interpolation. In such case, a subset of A_i might be selected which has a consistent trend in change of magnitude. The practical demonstration example will elaborate this possible situation in detail.

4.1.4 Difference of Proposed Methods from Similar Methods

a) Riemann surface of arctan (complex number) is relatively complicated however the Riemann surface of complex logarithm is very similar to Figure 4.1 [59]. They can be used to determine the required ‘branch’ of the complex function curve and thus value of k can be ‘selected’ for use in Eq. (4.2). A similar concept is the winding number which is the number of finite turns that a closed curve takes around an arbitrary fixed point. If there could be a way to find k or the number of turns of phase revolution corresponding to a certain measurement, then the problem of phase ambiguity could be resolved. However, Riemann surfaces cannot be used for ‘finding’ the value of a particular branch cut (k in Eq. (4.2)) corresponding to a certain physical phenomenon. This is because the open curve of Riemann surface (for complex logarithm) and the spiral complex (blue) curve of Figure 4.1 extend from -∞ to +∞ and there is no way to differentiate between any two branches of the Riemann surface / complex curve (as far as phase angle is concerned).

b) The phase retrieval methods generally employed in diffraction imaging rely on the phase less information which is usually in the form of signal intensity (magnitude) [41]. The nature of those measurements is such that the phase information is not available there. However, the method proposed here works by extraction of phase information contained along with magnitude information in the Fourier transform of the signal. In fact, the magnitude and instantaneous phase of two complex numbers, work in tandem to generate unambiguous phase difference between two consecutive complex numbers and this phase difference is now not capped by virtually any limit.

c) De Bruijn code is another technique used for phase unwrapping [60]. However, that is relatively computationally more complex and based on conventional wrapped phase shadowed by 2π phase ambiguity.

The concept introduced above, is further explained below with a simulation example and a real time / real data experiment.

4.2 Demonstration of the Proposed Method with FMCW Radar Speed Measurement

It is the $x_{mb}(t)$ in Eq. (2.12) which is the focus for demonstration of the phase interpolation method proposed in this article. Although this time domain signal contains the target range and velocity information, however, either one or both of these information cannot be derived from time domain magnitude and/or phase of IF signal. Therefore, the time domain signal of Eq. (2.12) is converted to frequency domain by FFT.

4.2.1 Speed Measurement in FMCW Radars

Speed is measured in FMCW radars by using the phase change between the echo returns form chirps lying in the same range bin. However, use of either two-dimensional (2D) FFT or one-dimensional (1D) FFT is the implementation level detail that defines two similar ways for speed measurement. A brief introduction to these ways will help in better understanding the application of the proposed method in a real time demonstration. (Speed and Velocity are used interchangeably in this thesis).

1) Speed measurement by 2D FFT:

This method requires combining a certain number of chirps into a frame and a certain number of frames are then transmitted, received after reflection from target and then processed by 2D FFT to form a range-doppler map for each frame. Speed information can be readily derived from the range-doppler map. Each frame can be thought of one Coherent Processing Interval (CPI).

2) Speed measurement by phase change in 1D FFT:

The second method for velocity measurement makes use of 1D FFT range profile for each chirp. The method uses the phase difference between target echoes from two successive chirps for velocity measurement as per following relation [61]:

$$v_r = \frac{\lambda \Delta\varphi_v}{4\pi T_c} \tag{4.4}$$

where v_r is the velocity of target relative to the radar, $\Delta\varphi_v$ is the difference between instantaneous phases of target echoes from two consecutive chirps, λ is the wavelength and T_c is the chirp time. The 1D FFT divides the range profile (or time domain signal) into frequency bins with width Δf given by relation:

$$\Delta f = \frac{F_s}{n} \tag{4.5}$$

where F_s is the sampling frequency and n is the number of FFT points. The complete range profile can be divided into n range bins whose width can be calculated either by relation $\Delta R = c/2B$, or by converting Δf to ΔR by using relation $\Delta R = c\Delta f/2S$. For the speed detection method by using Eq. (4.4), it is imperative that the two consecutive chirps lie within the same range bin, however, the restricting condition is that the phase difference should not exceed π rad. Considering the unambiguous phase $|\phi| < \pi$, Eq. (4.4) gives the maximum detectable velocity as [61] :

$$v_{r,max} = \frac{\lambda}{4T_c} \quad (4.6)$$

4.2.2 Demonstration Scenario and Setup

The demonstration of the proposed method is attempted with conduct of a field experiment and allied simulation study. The details of the demonstration scenario, setup and conduct of experiment are furnished to elaborate the problem statement, especially in context of FMCW radar.

1) Experimental setup and parameters:

A deliberate attempt is made to not indulge in to the radar technology specific jargon, however, the following necessary details are furnished for the general reader including technologists, mathematicians and other physical sciences' experts.

A COTS mmwave FMCW radar platform is used for the conduct of the experiment (the COTS platform is not being identified in order to avoid publicizing a particular product). The target used has an extremely small RCS which is towards the lowest limit of the RCS detectable by this radar. The target has a (nominal) speed of 296 m/s which is well beyond the speed measurable by the relevant COTS radar due to hardware constraints. Among many other parameters, the COTS radar enables the user to select the number of time domain signal samples, frequency slope, chirp duration etc. The experiment is conducted in an open field, without an anechoic chamber. The target under study is a 5.5 mm airgun pellet which is fired from an airgun with 1000 feet per second (fps) nominal muzzle speed, Figure 4.4 shows the 5.5 airgun pellet used in this study. Figure 4.5 shows the actual experimental setup. The radar platform is placed on first floor of a building which helps in avoiding ground clutter. Figure 4.6 shows the graphical sketch of the experimental setup to explain the geometrical aspects.

Figure 4.4 5.5 mm airgun pellet (target under study)

Figure 4.5 Actual experimental field setup

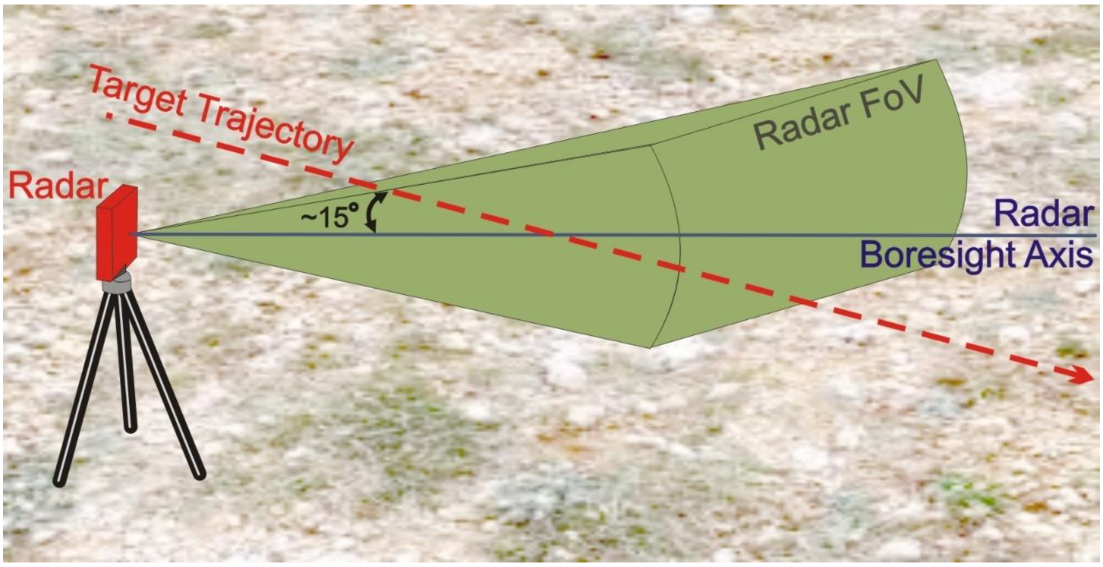

Figure 4.6 Sketch of the experimental setup

2) Conduct of experiment for data collection and problem statement

For this experiment, the small RCS target (airgun pellet) with 296 m/s (nominal speed) is made to cross the radar field of view (FoV) at a range of approx. 0.5 ~ 0.8 m from the radar. A carrier frequency bandwidth of 4 GHz is used. The azimuth and elevation beamwidths of the radar receiving antenna are 60° and 30°, respectively. 128 time domain samples are acquired for each chirp, 32 chirps are combined in one frame and 450 frames (total 14400 chirps) are transmitted and received. The data is post-processed in offline mode for this proof of concept. In order to keep the data in its raw and empirical form, the FFT is performed with radix-2 algorithm without any windowing, zero-padding or truncation. As the target is traversing across the radar FoV at almost 0.85 Mach speed, therefore it is detected in just one or a few frames. Figure 4.7 shows the 2D FFT range-doppler map for the 200th frame in which target was detected. It can be observed that the maximum detectable velocity is ~ 25 m/s and as the target speed is ~ 300 m/s, therefore, although the target is detectable, however, the velocity measurement is ambiguous and seems to smear across a number of bins in the range-doppler map.

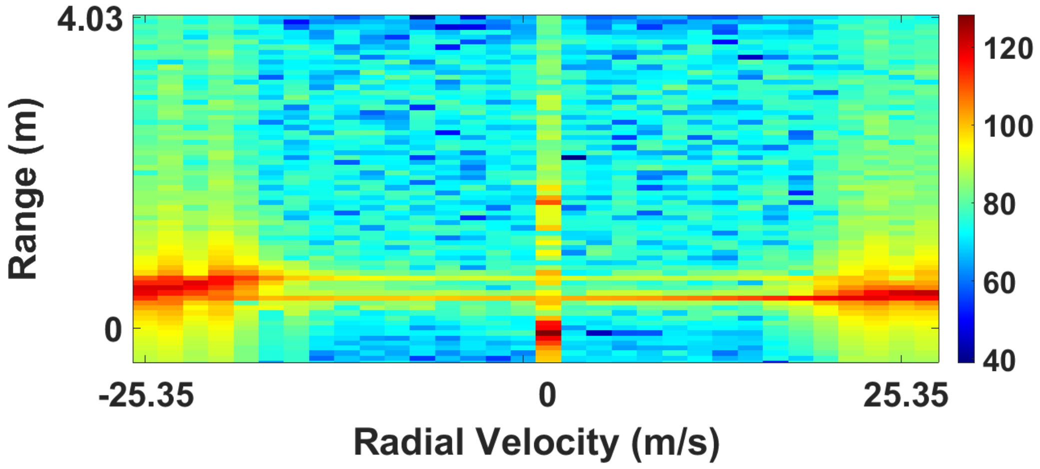

Figure 4.7 Range-doppler map (2D FFT) of complex number data (of time domain)

This phenomenon is occurring because the Pulse Repetition Frequency (PRF) is not high enough (due to hardware constraints) and thus the doppler ambiguity is evident and signal energy is spread across several doppler bins [62].

Figure 4.7 also highlights a reason for not performing any type of windowing operation which is that field data has fairly noticeable peaks in 2D FFT Range-Doppler map (Figure 4.7) in spite of the fact that the target has very small RCS and the actual target speed is many times more than the unambiguous speed measurement limit. This makes use of a windowing operation redundant.

The speed can also be measured using 1D FFT method discussed earlier. The values, $\lambda = 0.0039$ m and $T_c = 36$ µs, are used in this experiment. Using these values in Eq. (4.4) gives maximum detectable speed of 25 m/s which is in agreement with Figure 4.7, 2D FFT range-doppler map. This implies that both of the above-mentioned speed measurement methods give same maximum measurable speed limit and that an ambiguity in speed measurement is bound to occur with these parameters.

It is at this juncture that the approach suggested above becomes useful for unambiguous speed measurement, with virtually no upper limit.

4.2.3 Tailored Pseudocode for The Implementation of The Proposed Method

The following pseudocode delineates the steps for the execution of the proposed phase interpolation method. This pseudocode has been tailored (from

Pseudocode I) for the demonstration of the earlier proposed phase interpolation method for use with FMCW radar for speed measurement.

```
Pseudocode 2: Implementation of proposed phase interpolation method for speed measurement in FMCW radar
Input:
    Consecutive sampled complex numbers denoting time domain IF I/Q Target echo chirp data, $D_i = \{D_1, D_2, D_3, \ldots, D_i\}$ , where size($D_i$)= number of ADC samples/chirp

Procedure:
    1. Complex FFT operation with no zero-padding or truncation, $C_i = \mathrm{FFT}(D_i)$
    2. Magnitude, $\mathrm{FM}_i = \mathrm{abs}(C_i)$
    3. Target Peak Magnitude, $A_{pi} = \max(\mathrm{FM}_i)$
    4. Extract target beat freq, $f_{bi}$ from each $C_i$
    5. FFT/Range bin having target → Plot $A_{pi}$ vs $C_i$
    6. Select $C_i$ lying in same range/FFT bin and having linear decaying (or increasing) relation (discussed in Section 4.3.2(1) ), $C_s = \{C_{s1}, C_{s2}, C_{s3}, \ldots, C_{sm}\}, sm \leq i$
    7. Range (Physical quantity) $R_{s1}$ | $f_b(C_{s1}) \longrightarrow R_{s1}$ (convert beat frequency to range using chirp slope (S), $R = {f_b \times c}/{2S}$ )
    8. $A_{s1} = \max(\mathrm{abs}(C_{s1}))$
    9. Range (Physical quantity) corresponding to 2π phase difference, $R_{2\pi} = R(\lambda, \varphi_{2\pi})$
    10. Magnitude 2π, $A_{2\pi} = A(R_{s1}, A_{s1}, R_{2\pi})$
    11. for the $C_{sm}$, $(m = 1, 2, \ldots, m)$, do
        Pick $A_{sm}$
        Initialize Counter, Ctr = 0
        Set $A_{ctr} = A_{sm}$
        repeat
            $A_{ctr} = A_{sm} + A_{2\pi}$ (or $A_{ctr} = A_{sm} - A_{2\pi}$ )
            Increment Ctr
        until $A_{ctr} < A_{sm+1}$ $(or\ A_{ctr} > A_{sm+1})$
        Ctr = Ctr - 1
        $Phase(C_{sm}, C_{sm+1}), \varphi_m = \varphi(C_{sm}) + (2\pi \times Ctr) + \varphi(C_{sm+1})$
        reset Ctr⟶ 0
    end

Output:
    ▪ Vector of phase values (not constrained by 2π limit), $\varphi_{sm} = \{\varphi_{s1}, \varphi_{s2}, \varphi_{s3}, \ldots\ldots, \varphi_{sm-1}\}$
    ▪ Vector of Velocity values, $V_{sm} = {\lambda\varphi_{sm}}/{4\pi T_c}$
```

Direction of Interpolation (DoI) has been discussed earlier with Pseudocode I and allied aspects are discussed further in detail in ‘Peculiarities and Constraints’. Therefore, in order to keep the structure lucid, this aspect is not elaborated much in Pseudocode 2.

4.3 Simulation and Experimental Results

The proposed method is explored and validated jointly by means of both simulation and experimental evaluation. The results and discussion of the simulation and experimental are presented together for ready reference. A few notes specific to the simulation study are as follows:

4.3.1 Speed Measurement in FMCW Radar

The simulation study is carried out primarily by modeling of Eq. (2.10), Eq. (2.11) and Eq. (2.12). The relevant parameters have already been defined with these equations. The parameters used in the simulation as well as experimental study are: Number of ADC samples/chirp = 128, frequency slope (S) = 99.022 MHz/μs, f_c = 77 GHz, Chirp time (T_c) = 35.2 μs, c = speed of light, v = velocity of target i.e. 296 m/s and sampling frequency (F_s) = 5500 ksps. The target is supposed to be present in 12th FFT/range bin and 4 chirps in the same FFT/range bin are simulated. The FFT/range bin changes when beat frequency changes by $\Delta f\ /\ 2$ (from Eq. (4.5)). Therefore, the target beat frequency is calculated by using the relation $f_b = (\Delta f \times (\text{Target bin index} - 1)) + (\Delta f\ /\ 2)$. The initial range corresponding to first chirp is then obtained by $R_1 = R(f_b, \text{freq slope}) + (2 \times \text{distance travelled per chirp})$, where the last term introduces a sort of buffer to place the range measurements and the chirps well within the boundaries of the relevant FFT/range bin. It is pertinent to mention that the ranges for simulation of chirps and FFT/range bin need to be selected carefully while considering their mutual interaction with nominal speed. It is imperative that all the chirps (under observation) must reside in the same FFT/range bin otherwise the relation between their magnitude and phase will become meaningless due to change in FFT/range bin. Although, these chirps will have different factual ranges and different magnitudes, however, owing to the FFT range resolution, the target echoes (chirps) will give same f_b(and range) after 1D FFT.

The parameters F and H in Eq. (2.10) and Eq. (2.11) hold certain significance. In many texts, the relations for FMCW complex baseband IF I/Q signal assume a unity magnitude. However, for a truthful modeling, the magnitudes of transmitted and received signals (F and H respectively) need to be considered. Therefore, the terms F and H are calculated by using standard radar range equation given as [27]:

$$P_r = \frac{P_t G_t G_r \lambda^2 \sigma}{(4\pi)^3 R^4} \tag{4.7}$$

where P_r is the power received at the radar after reflection from the target, P_t is the power transmitted by the radar, G_t is the gain of the radar transmitter antenna, G_r is the gain of the radar receiver antenna, λ is the wavelength of the carrier frequency, σ is the target RCS and R is the target range. Transmitted power of 17 mW, Tx and Rx antenna gains of 9 dB and a roughly estimated target RCS of -39 dBsm are used to estimate the received power/magnitude corresponding to factual range of each chirp. The Tx power of 17 mw is used as F and received power for each chirp using above parameters is used as H in Eq. (2.10) and Eq. (2.11). This mapping helps to bring in the relative strength of Tx signal and RCS dependent Rx signal strength.

Eq. (2.10) and Eq. (2.11) in [22] assume that chirp time is equal to ADC sampling time. However, it is not the case in real world and there is usually a non-sampling buffer time as well within the total chirp time. Therefore, in order to simulate equations Eq. (2.10), Eq. (2.11) and Eq. (2.12), total chirp time 35.2 µs is used while the ADC sampling time is 23.2 µs which corresponds to the 128 ADC samples. These values are selected to match the experimental and simulation scenario as much as possible.

Further note that as the sampling frequency does not appear in Eq. (2.10) and Eq. (2.11), therefore, the simulation results are found to be not affected by change in sampling frequency. However, indeed, the Nyquist criteria needs to be observed.

4.3.2 Proof of Concept with Simulation Data and with Experimental Field Data

The simulation study is carried out while considering above details and as per Pseudocode 2. In addition, the results obtained from experiments carried out were also subjected to the Pseudocode 2.

Simulation studies are carried out with the same parameters as used for the experimental study. Figure 4.8 shows the linearly decaying magnitude calculated with using first chirp as reference. The magnitudes of target peaks in relevant chirps are also shown as straight horizontal lines. The time domain data has been obtained from Eq. (2.10), Eq. (2.11) and Eq. (2.12), as discussed earlier and then the chirp magnitudes are obtained for the 4 chirps after ID FFT.

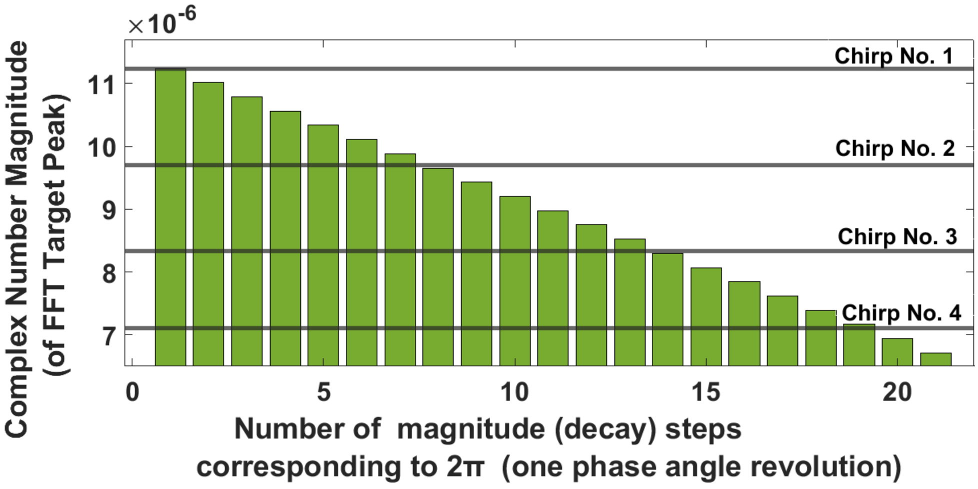

Figure 4.8 Simulation result of calculated gradual decay of Magnitude (of FFT Target Peak) from reference chirp 1

1) Some peculiarities and practical limitations

As an experimental data sample, the chirps contained and observed in one range bin are shown in Figure 4.9. This data is a subset of the frame no. 200 shown in Figure 4.7 range-doppler map which pertains to the real time data acquired for a target receding away from the radar with a nominal speed of 296 m/s. The magnitude of complex baseband target echoes after 1D FFT falling in range bin 12 are plotted in Figure 4.9.

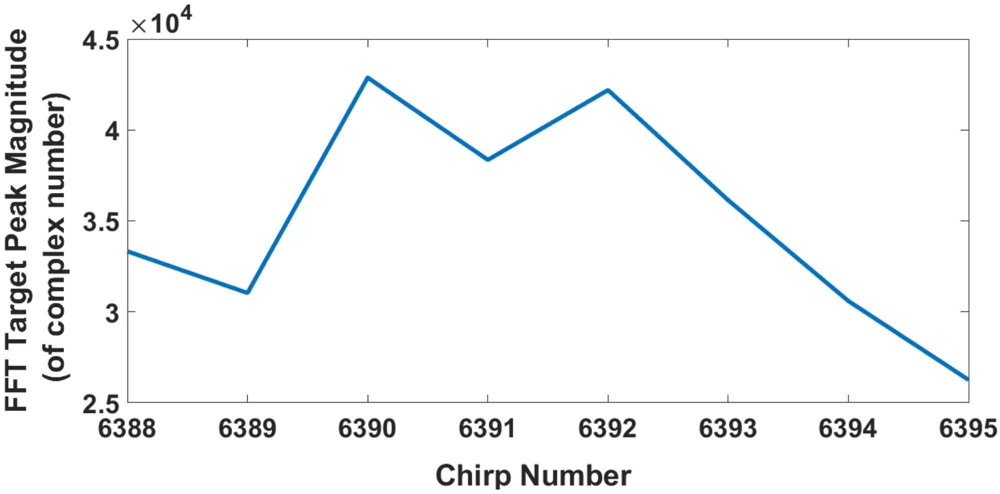

Figure 4.9 Magnitude of (complex numbers) of target peaks of chirps in Range (FFT Frequency) Bin No. 12

As per elementary radar theory, the magnitude of the target echo for a receding target must decrease with time for each subsequent chirp. However, it can be seen that the magnitude is increasing for a few initial chirps although the target is receding. This is a peculiar case as the target (Figure 4.4) has a non-symmetrical shape and thus non-uniform RCS. In this case, the RCS is dependent on the aspect angle. A similar study discusses the RCS variation with aspect angle in same mmwave frequency band [63]. As the target is traversing the radar FoV at an angle as it crosses radar boresight, its aspect angle changes. This change in aspect angle presents increased RCS to the radar beam therefore, for a few initial chirps, the increased RCS results in stronger echo magnitude even when the target is receding. As this study is part of a bigger project and as it is desirable to study the particular target with a much higher speed than the speed detectable by the particular COTS radar, therefore, it is deemed appropriate to use this target / speed for this proof of concept as it was not possible to project a uniform RCS target with this speed along the radar boresight.

For the experimental data, it can be seen in Figure 4.9 that chirps number 6392, 6393, 6394 (and 6395) have an (almost) linearly decaying relationship in their magnitude which is also in agreement with a priori knowledge that the target was receding. Note that, if the selected chirps have a linearly decaying (or increasing) relationship among their magnitudes, it would not make difference if the magnitude of first chirp is used as reference magnitude for all the subsequent chirps, or, if the magnitude of each previous chirp is used as reference for next chirp. Considering this, Figure 4.10 shows the linearly decaying magnitude calculated with using first chirp (6392) as reference. The actual magnitudes of target peaks in relevant chirps are also shown as straight horizontal lines, for reference.

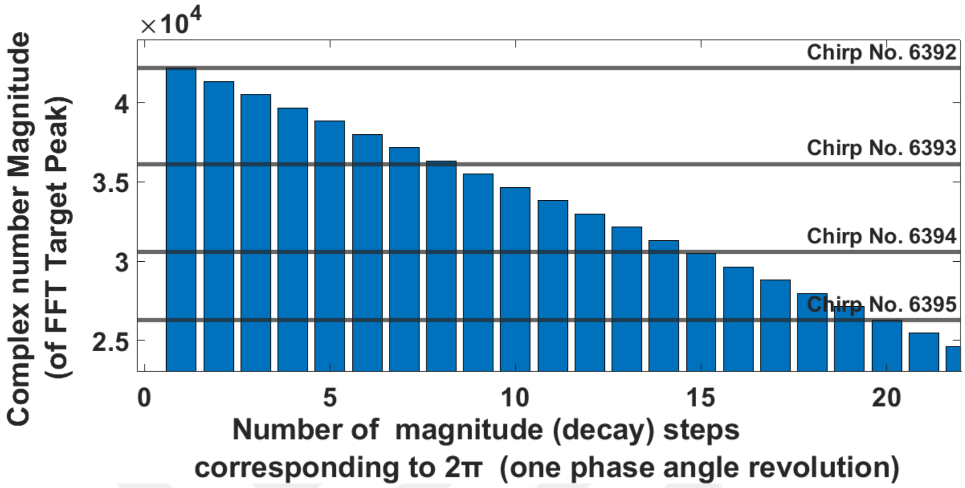

Figure 4.10 Calculated gradual decay of Magnitude (of FFT Target Peak) from selected reference chirp

2) Phase ambiguity resolution and speed measurement beyond maximum unambiguous speed

As elaborated in Pseudocode 2, and referring Figure 4.8 and Figure 4.10, the total phase between two chirps is calculated as $\text{Phase}(C_{sm}, C_{sm+1}), \varphi_m = \varphi(C_{sm}) + (2\pi \times \text{No. of discrete magnitude steps}) + \varphi(C_{sm+1})$. This total phase is then used to calculate the target speed using Eq. (4.4).

Thus, Figure 4.11 shows the speed calculated by the simulation study from the relevant chirps by using accumulated linearly interpolated phase angle change as explained above. Likewise, Figure 4.12 shows the speed calculated from the experimental data from the relevant chirps (Figure 4.10) and Pseudocode 2 with Eq. (4.4). Compared to Figure 4.7 (range-doppler map) and considering the susceptibility of phase to noise and other suboptimal factors discussed in the start of this chapter, it can be seen that the proposed methodology enables the measurement of phase angle beyond the ambiguous limit. In this particular simulation and experimental setup, the proposed method has enabled unambiguous measurement of phase difference of ~12π between two consecutive chirps (complex numbers) as opposed to 2π phase difference as dictated by classical complex number theory. This extended phase difference enabled estimation of speed with optimal accuracy, which was earlier ambiguous in standard range-doppler map method and in the phase difference method using 1D FFT range profiles.

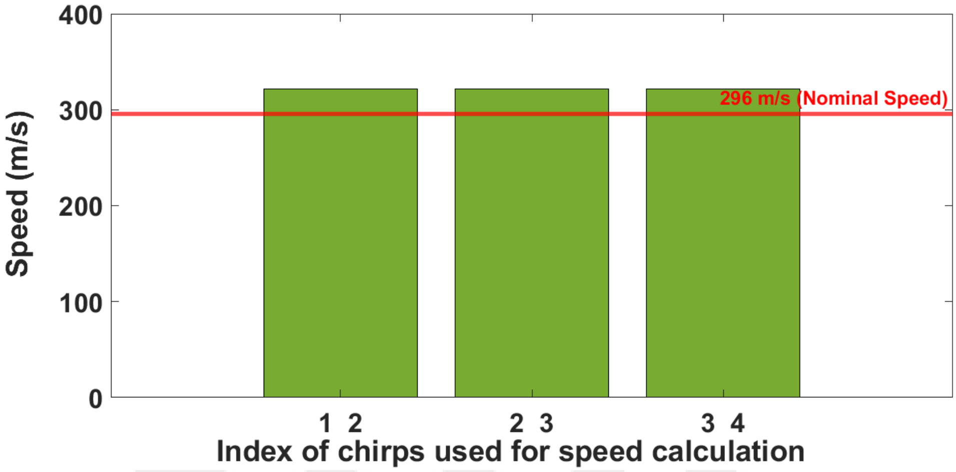

Figure 4.11 Simulation result for speed calculation

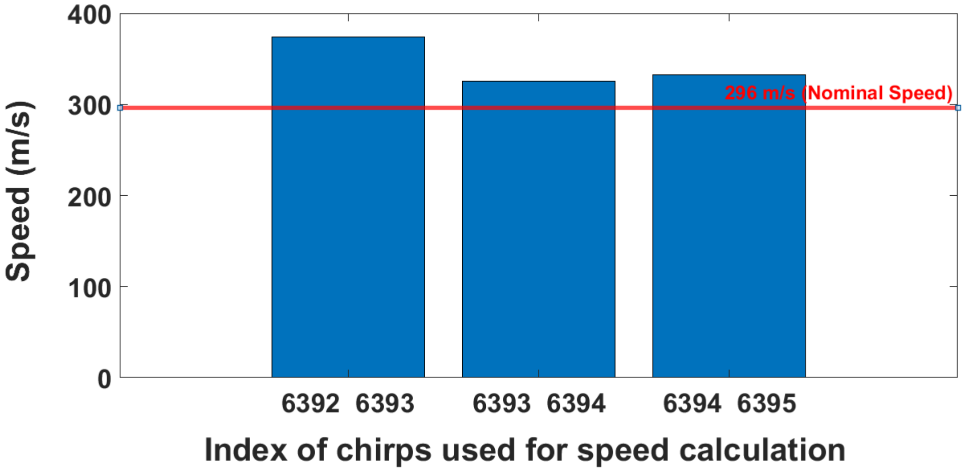

Figure 4.12 Experimental results for speed calculation from selected chirps

4.4 A discourse on The Results

The proposed technique has been demonstrated by simulation results with explanation of basic underlying concept. In addition, the experimental demonstration explains the application concept in a more rugged and realistic manner but it has some significant allied constraints as well. The technique is able to produce *optimally* accurate and stable results provided that the real life data is as much free from unwanted noise and disturbances as possible. This particular experiment can be termed as possibly one of the worst-case scenarios, involving very small RCS, RCS variation of target along its trajectory due to change in aspect angle, unavailability of anechoic chamber and target speed being almost 12 times the speed unambiguously measurable. However, the method has been able to measure the speed with optimal accuracy.

4.4.1 A Caution about the Linearity Concept

This method works on an interpolation concept involving a '*linear*' relationship between complex magnitude and the 'integral' multiples of 2π angle rotations as shown in Figure 4.2. This needs to be segregated from an approximated quasi-linearity in the FMCW radar demonstration example. Make a special note that in Figure 4.8 and Figure 4.10, the magnitude of the target is 'almost' linearly dropping but it does not imply that the range is also necessarily linearly changing. It rather implies that the phase angle is almost linearly changing. It is well-known in radar engineering that the received power varies inversely with fourth power of range i.e. $P \propto (1 / R^4)$, implying a directly proportional but non-linear relation between P and $1 / R^4$. However, given that if the range measurement is infinitesimally small (i.e. range bin of ~4 mm against total range of ~50cm), then the relation between power (P) and range (R) can be termed as 'almost' linear. This 'approximation' can be used and in fact it is used in our calculations for calculating power at certain ranges. This will bring a source of error (as it is an approximation) when our phase interpolation method will be used in radar scenario but that this can be termed an acceptable error / approximation. This approximation will be field-specific and independent of the method being proposed. In the incumbent radar field example, it will was governed by $P \propto (1 / R^4)$ law. In optics, for example, it will be governed by the relation between intensity and phase, and likewise the effect of approximations will also probably change. In fact, the application of this proposed technique will be probably relatively convenient in some other scientific field where the relation between the magnitude of complex number and the physical quantity would be linear and directly proportional.

4.4.2 Further Sources of Errors and Constraints

Figure 4.8 and Figure 4.10 (for simulation and experimental study) show that reference and final chirps of the subset used for speed detection, contribute partial values to the total phase difference value. Although the complete linear multiples of phase have a clear relation with phase as they produce a phase excursion of 2π (Figure 4.2 and Figure 4.3), however, 'within' one bar representing a single 2π phase travel (Figure 4.8 and Figure 4.10), there is not such linear relation between the phase and magnitude of the complex number. This happens when partial phases are derived from the reference chirp ($\varphi(C_{sm})$) and final chirp ($\varphi(C_{sm+1})$), which introduces a maximum uncertainty of (2π+2π=) 4π rad in total phase (as shown in Pseudocode 2). A look at Figure 4.8 and Figure 4.10 shows that this uncertainty can be reduced if this (maximum) 4π, or the reference and final chirp phase contributions, form a lesser part of total phase travel which implies that λ should be decreased and/or chirp separation should be increased. These are theoretically possible, however, there might be practical limitations to those due to hardware constraints.

One major constraint is that this proof of concept is based on the conduct of experiment with the a priori knowledge of the velocity direction. This, coupled with the peculiar phenomenon of the target echo magnitude increase for a few initial chirps, for a receding target (due to RCS variation with aspect angle), is a scenario specific to this experiment. However, the underlying theory has been still demonstrated to be theoretically correct and experimentally demonstrable.

As the method is basically dependent on magnitude variation to interpolate phase angle, therefore, it is mandatory that the magnitude variation is predominantly caused only by the variations in the relevant physical parameter. Referring specifically to the radar application example, it is imperative that the target echo magnitude change is mainly caused due to range change and effects of noise, clutter and other disturbances are minimal.

The proposed idea is demonstrated for a receding target; the same idea is applicable to an approaching target as well.

4.4.3 Conditions for Interpolation of Magnitude for Phase Disambiguation

For establishing a truly linear relationship along a line, at least three points are needed. Therefore, it is suggested to at least have three points/chirps for the complex phase interpolation by this method.

This brings forth two corollaries.

Corollary # 1: The magnitude decay (and velocity) to be measured is assumed to be constant. If it is not the case, then the chirp time could be made infinitesimally small so that the magnitude decay (and velocity) remains constant during that time period. However, again, there might be practical impediments to that effect.

Corollary # 2: If the measurement time needs to be long enough and magnitude decay does not remain linear and velocity does not remain constant during that time interval, then the desirable condition of at least 3 points can be foregone. Still in that case, the method is capable of measuring phase difference between two complex numbers (chirps) and thus the velocity can be measured with quantization steps related to chirp time interval. This further implies that this method can be used to measure acceleration if at least two velocity measurements are available.

4.4.4 Possible Applications in Other Fields

The proposed method for interpolation of magnitude for resolving phase ambiguity has been first explained in the generic context of complex number theory. After that, the method is demonstrated by an applied field example for speed measurement in FMCW radar. The critical step in this regard is the conversion of the magnitude of relevant complex number, x, into the physical quantity, y, line 3 of Pseudocode 1, Input. The binding condition in this regard is that the relation between x and y should be linear or quasi-linear. This physical quantity could be specific to the particular field. In the case of demonstration example used in this manuscript, this physical quantity is the range of target. As this method is nascent to our knowledge, other field experts may like to explore application as per their expertise area. *Thus, this work humbly invites specialist from other fields to study and determine possible application of this method in other scientific fields where the problem of 2π phase ambiguity is encountered.*

4.5 Conclusive Remarks on Phase Interpolation Technique

The motivation for this part of thesis research work was to find ways to resolve phase angle ambiguity in complex number theory, especially in situations where it was not possible to circumvent the phase ambiguity due to limitations imposed by physical phenomena or technology constraints. The method is based on a nascent pragmatic perspective of a classical aspect of relation between phase and magnitude of complex numbers and works on interpolation between the magnitudes of two complex numbers to resolve the phase angle ambiguity. The method has an applied nature and it has been demonstrated with simulation and with a real time example of data collected from a COTS FMCW radar. The assumptions and possible limitations vis-à-vis the improvement venues from application perspectives have been identified. The method enables phase angle resolution in complex number theory. It can be especially useful in the fields where the phase angle is further used for estimation of displacement and/or velocity. The experimental results show that the velocity measurement by this method is not very accurate but it is fairly optimal considering that virtually there is no upper (theoretical) limit for the phase angle measurement and considering that phase angle is relatively quite prone to the disturbances/noise in real life applications.

The proposed method alleviates the need of using phase unwrapping algorithms which have their own limitations. The basic principle of the method is generic in nature however, the application example has certain limitations as discussed earlier. The applicability of the proposed method can be explored in other mathematical and physical sciences fields under the stated constraints provided that the limitations are overcome.

CHAPTER 5

APPLICATION OF CHINESE REMAINDER THEOREM FOR RESOLVING VELOCITY AMBIGUITY

Chinese Remainder Theorem (CRT) is a mathematical tool that is widely used in pulse Doppler radar literature for resolving the range and velocity ambiguity and the same is used in this thesis reaearch. This chapter presents a velocity disambiguation demonstration with CRT but a similar method can be applied to resolve range ambiguity as well. The simulation scenario is not presented as it would be straightforward and will not add much value. It is further deemed that real-life field demonstration example with a commercial-off-the-shelf (COTS) automotive mmwave radar brings forth some of the actual real time challenges faced in application development. In addition, the author notes that to his knowledge, such a tutorial study of velocity disambiguation in FMCW radars has not been reported in the literature with similar scenario, operating frequency and target speed.

5.1 Theoretical Prerequisite

5.1.1 The Single-Sided FFT, Double-Sided FFT and Doppler Frequency

FFT operations are typically used to provide the frequency domain picture from time-domain data acquired by the radar. Depending on the hardware used, real-only or complex (I/Q) data are available. The difference between these configurations is not important here and is not within the scope of this thesis. One has only to note that with complex input data, a complex FFT has to be used along the fast time dimension.

A chirp is defined in FMCW radars as a single waveform with LFM frequency. One-dimension (1D) FFT operation is performed on the time domain IF samples of a chirp which produces range profile for that chirp. The property of the FFT operation is that it decomposes the time domain signal into sets of positive and negative frequencies. As negative frequencies are meaningless in the physical world, therefore, the half FFT spectrum comprising the negative frequencies, is discarded. The individual quantized steps of the range profile obtained after 1D FFT are called range bins.

Further considering the general relations $A(t) = A_{max}\cos(\omega t + \phi)$ and $A(t) = A_{max}\sin(\omega t + \phi)$ and comparing them with Eq. (2.10) and Eq. (2.11), we can see that the beat frequency contains a constant phase term $(2f_c\, v/c)nT_c$ which varies from chirp to chirp, as n changes. This constant phase term adds to the term $(4\pi f_c/c)R_0$, as it reflects the increase of $R(t)$ from chirp to chirp.

This gives an expression for measuring the velocity, v_r, in FMCW radars, mentioned earlier as Eq. (4.4). The phase change between 1D FFT profiles may be interpreted as a complex sinusoid with normalized frequency of $\Delta\varphi_v\ /\ 2\pi$. Thus, estimating this frequency is possible with another FFT performed in the chirp-to-chirp direction and this is the idea of 2D FFT use in FMCW radar.

A second FFT operation is carried out across the subsequent chirps for each range bin and this produces the velocity profile. The combined output of two dimensional (2D) FFT is usually called Range-Doppler map (RD-map) which is obtained by sequentially executing 1st FFT and 2nd FFT on the time domain IF data from the radar. It should be noted that the 1st FFT is executed with the real or complex input data – depending on the hardware configuration – and the result is complex (having magnitude and phase information). Then, the 1st FFT result is an input to the 2nd FFT, thus the 2nd FFT deals with the complex input. Reference [64] discusses the modalities of real and complex FFT in detail.

In 2nd FFT, the negative frequencies are not discarded and both the positive and negative frequencies after the 2nd FFT are retained and analyzed in the velocity (Doppler) spectrum. The sign of the Doppler frequency indicates the direction of relative motion between the target and the radar – one can easily see the meaning of the positive or negative value of v in Eq (2.8).

A reader should note that there are two possible conventions for assigning the sign to the velocity. The prevalent one as used in Eq (2.8) is to see velocity as the derivative of $R(t)$ – thus we mark a positive velocity when the distance between the radar and target increases. Then, the Doppler frequency is given by the relation [65]

$$f_D = {}^{-2\dot{R}}/_{\lambda} \tag{5.1}$$

where f_D is the difference between the transmitted and received frequencies caused by the relative movement of radar and target (Doppler shift), $\dot{R}$ is the rate of range change and λ is the wavelength of the carrier signal. The minus sign is used to indicate that the approaching targets produce positive Doppler shift as range decreases implying a negative range rate [65]. However, in a practical FMCW radar implementation, it may happen that we measure the positive frequency along the slow time dimension for receding targets because of some hardware aspects, such as the reverse order of subtraction between the received and transmitted frequencies, the use of downchirp (negative (S) value) instead of upchirp or due to some frequency conversions in the RF frontend. In fact, in the particular radar hardware platform used in this experimental study, the positive Doppler indicates a receding target as opposed to a negative Doppler as required by Eq. (5.1). It is therefore essential to determine the true sign of the measured Doppler frequency vis-à-vis the direction of target motion for the specific hardware platform by using a relatively low speed target with a velocity less than the maximum ambiguous velocity for the particular PRF. This is required because a velocity greater than the maximum ambiguous velocity could get folded and aliased either as positive or as negative velocity and the results will be wrong if correct sign of the Doppler frequency has not been established beforehand.

The relation between the range of unambiguous Doppler frequency f_D obtained after 2D FFT of time domain IF samples and the PRF is given by [8]

$$-\frac{1}{2}\text{PRF} \le f_D < \frac{1}{2}\text{PRF} \tag{5.2}$$

Unless zero-padding or truncation is used in the 2nd FFT, the Doppler resolution is always equal to the width of the Discrete Fourier Transform (DFT) filter, given by ${}^{\text{PRF}}/_{N}$, where N is the number of DFT filters (DFT bins). One may recall here that in this case N is also equal to the number of FFT input samples.

The concept of CPI is relevant here which is the combination of a certain number of chirps (equally spaced in time – thus “C” for “coherent” in the CPI acronym) across which 2nd FFT is executed. For practical purposes, N can also be defined as the number of chirps in a CPI. Given that a N-point 2$^{\text{nd}}$ FFT (Doppler FFT) is executed and given that a target is detected in the k^{th} Doppler cell, then the sign and magnitude of Doppler frequency f_D are determined as given in [8]:

$$f_D = \begin{cases} k\dfrac{\text{PRF}}{N} & if\ 0 \le k < \dfrac{1}{2}N \\ -(N-k)\dfrac{\text{PRF}}{N} & if\ \dfrac{1}{2}N \le k < N \end{cases} \tag{5.3}$$

Note that the index runs from 0 to $N-1$. The terms Doppler cell and Doppler bin are used interchangeably. The Doppler bin at zero-index is also called zero-Doppler bin. From a FFT point of view, it contains the sum of all the signal samples, which is, in another formulation, the DC component of the signal. From the radar engineering perspective, in a 2D FFT RD-map, the zero-Doppler column contains the target echo returns from all the stationary targets including clutter. Its significance will be discussed further in section 5.2.4, section 5.3.6 and in Figure 5.9 which shows the zero-Doppler column and correct Doppler bin numbering for the RD-map. Eq (5.3) defines the part of spectrum occupied by the positive and negative frequencies respectively.

5.1.2 The Velocity Ambiguity Problem

Doppler velocity measurement by finding the frequency along the slow-time dimension will be unambiguous only if the Nyquist criterion is fulfilled. As the Doppler signal is sampled with sampling interval equal to T_c, the Nyquist criterion is equal to the requirement of $|f_D \times T_c| < 1/2$ (or $|f_D \times T_c| < 1$, assuming that we know the sign a priori). Note that T_c is in some texts denoted as "PRI" $-$ Pulse Repetition Interval [66]. Velocity ambiguity arises when the actual target velocity is greater than the maximum unambiguous measurable velocity

Similarly, range ambiguity is an analogous problem. Range ambiguity may be present when the IF is sampled with a sampling frequency, F_s, too low with respect to the maximum possible frequency $(2SR_{max})/c$ – then the range will be unambiguous for the beat frequency with a maximum value of $F_s\ /\ 2$ as per Nyquist criteria and the range measurement will become ambiguous when the beat frequency measurement from samples will exceed that value. Even with F_s high enough, another type of range ambiguity may arise from the delay (τ in Eq. (2.8)) being larger than T_c – then the echo is mixed with the next Tx pulse (or even with m-th subsequent pulse, $m > 0$) and thus appears to be delayed by $\tau - mT_c$. This ambiguity type is related to PRF, as $T_c = 1 /$ PRF.

Various techniques exist for resolving the range and/or velocity ambiguities. One such described method suitable for f_D measurement is the carrier frequency variation but this is relatively undesirable due to complex technology requirements and possible RCS variation if frequency excursion is significant [67]. PRF variation is a preferable and popular method. No deterministic definition exists for defining the various PRF regimes, however, the subjective definitions are given as follows for the signal of interest [65] :

Low PRF : No range ambiguity, Doppler ambiguity exists
High PRF : No Doppler ambiguity, range ambiguity exists
Medium PRF : Both range and Doppler ambiguity exist

Please note that these regimes depend on the limits for the expected target ranges and velocities, i.e. on the considered application of a given radar.

We can see that by keeping the carrier frequency constant and increasing the PRF, the ambiguity domain moves from Doppler velocity to range measurement [67]. This concept is pictorially demonstrated with the conceptual Figure 5.1 (derived in part from [68] and [9]). Figure 5.1 shows the range-Doppler ambiguity generally for the three PRF regimes.

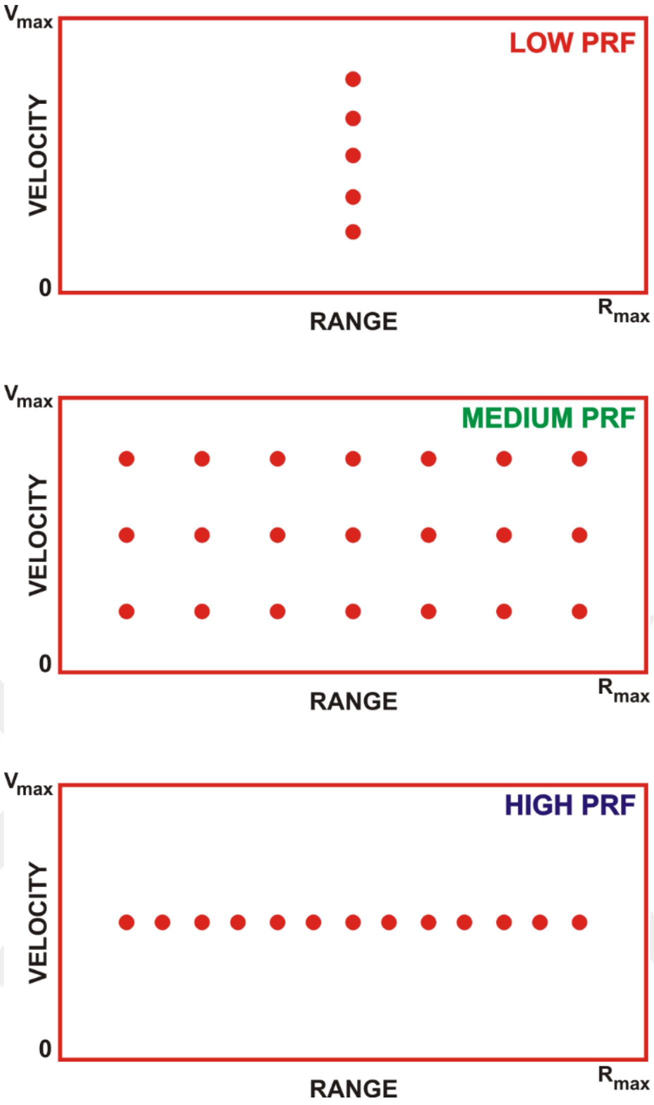

Figure 5.1 PRF Ambiguity Diagram

The low PRF, medium PRF and high PRF terms were defined for use in pulse Doppler radars as mentioned earlier, however, they also describe the properties in FMCW radar domain. The low PRF radars primarily work on time discrimination and possess good range resolution. These basically work by deriving range information from the term $(2SR_0/c)t_s$ in Eq. (2.10) and Eq. (2.11). The high PRF radars basically work on frequency discrimination and thus they mainly derive velocity information from the term $(2f_c\ v/c)nT_c$ in Eq. (2.10) and Eq. (2.11). We can see that either range or velocity or both types of ambiguities exist in high, low or medium PRFs. In any case, the use of multiple PRFs is a popular method to resolve range ambiguity or velocity ambiguity or both. The basic theme of the multiple PRF approach is to obtain more than one estimate for range or velocity from more than one PRFs and then use some ambiguity resolution technique to resolve the incumbent ambiguity. Theoretically, for a single target case, the use of two PRFs would be sufficient to resolve an ambiguity; however, additional PRFs may be added for redundancy [69].

5.1.3 The Chinese Remainder Theorem

The earliest form of the Chinese Remainder Theorem (CRT) is attributed to 3rd century Chinese mathematician Sun-Tzu. CRT is a theorem in number theory which states that it is possible to uniquely find a number from its remainders of division by certain integers under the general condition that the divisors are coprime (relatively prime).

The term CRT is also used with respect to mathematical tools for solving such a problem. Extensive literature exists on CRT problem formulation, however a very brief and concise CRT representation for velocity ambiguity resolution in radar applications is presented below, mainly adopted from [68]. We present it using three different PRFs, however it can be used with any number of PRFs greater than one.

Let K1, K2 and K3 be the number of Doppler cells in PRF1, PRF2 and PRF3, respectively. Let us assume that the Doppler frequency is measured with different CPIs and the PRFi and Ki are chosen such that the velocity cell size Δv is the same in all the CPIs. Let A_{ai} be the index of the apparent (ambiguous) measured target Doppler cell obtained from the RD-map for the i^{th} PRF. The general CRT (GCRT) requires Ki's to be co-prime and to be whole numbers. There are indeed some works reporting some robust versions of CRT which do not require Ki to be a whole number [70], however, this thesis chapter is based on the assumption of Ki being whole numbers and co-prime.

The Doppler cells are numbered from 0 to $(\text{Ki} - 1)$. Then the single-sided CRT resolved unambiguous Doppler cell number, A_{uCRT} is given

$$A_{uCRT} = (C_1 A_{a1} + C_2 A_{a2} + C_3 A_{a3})\text{modulo}(\text{K1K2K3}) \tag{5.4}$$

where

$$C_1 = B_1\mathrm{K2K3} \tag{5.5}$$

$$C_2 = B_2\mathrm{K1K3} \tag{5.6}$$

$$C_3 = B_3\mathrm{K1K2} \tag{5.7}$$

and B_i's are the smallest integers fulfilling the conditions

$$B_1\mathrm{K2K3}(\mathrm{modulo K1}) = 1 \tag{5.8}$$

$$B_2\mathrm{K1K3}(\mathrm{modulo K2}) = 1 \tag{5.9}$$

$$B_3\mathrm{K1K2}(\mathrm{modulo K3}) = 1 \tag{5.10}$$

There is one major drawback in CRT that if there is even a slight error of one Doppler cell in the target declaration, then the result of the CRT will be grossly incorrect. Such an error may appear when the actual frequency value is close to the FFT bin boundary. However, if there is the same quantity of error in all PRFs then the CRT result will not deviate significantly from the correct value.

Consider a case of K1=9, K2=7 and K3=5 and A_{a1}=7, A_{a2}=4 and A_{a3}=2, then we obtain A_{uCRT}=277. We assume that all A_{ui} have been declared without error, so A_{uCRT}=277 is assumed to be a correct answer. However, suppose that there is an error of just one cell number in Doppler cell declaration and A_{a1}=6 , while A_{a2} and A_{a3} remain the same. Then we obtain A_{uCRT}=312 and the large amount of error is evident. Now consider that we have a situation that induces an error and shifts the Doppler cell declaration by one number in all PRFs; thus suppose A_{a1}=6, A_{a2}=3 and A_{a3}=1, then we obtain A_{uCRT}=276, as compared to A_{uCRT}=277 in previous case and the error is quite small. The same aspect is reported in [71] for even a robust CRT based on a theoretical study demonstrating that the error range for the reconstructed integer is the same as error range for the remainders, provided that the error range does not exceed a certain limit.

5.1.4 The Coincidence Algorithm

The Coincidence Algorithm (CA) is another tool that is commonly used for resolving range and/or velocity ambiguity. Considering a case of velocity ambiguity with three PRFs, a simple presentation of CA is presented which is mainly adopted from [9]:

Let K1, K2 and K3 be the number of Doppler cells in PRF1, PRF2 and PRF3 and A_{ai} be the number of apparent ambiguously measured Doppler cell number for the the i^{th} PRF. The Doppler cells are numbered from 0 to $(\text{Ki} - 1)$. Then, the set of single-sided unfolded Doppler cell numbers, A_{ufi} is given by Eq. (5.11), adopted with modification from [72], [73]:

$$A_{ufi} = A_{ai} + o\text{Ki}\,, \quad o = 0, 1, 2, 3\,, \ldots \tag{5.11}$$

where o is the order of ambiguity (which is a (folding) integer), and Ki is the number of Doppler cells in the i^{th} PRF. Then the unambiguous Doppler cell number, A_{uCA}, is obtained at the first instance when all the unfolded Doppler cell numbers from all the PRFs coincide with each other. For a three PRF example, we obtain A_{uCA} when the following condition is met

$$A_{uf1} = A_{uf2} = A_{uf3} = A_{uCA} \tag{5.12}$$

CA is expected to be less error prone than CRT as an error of ± 1 or ± 2 Doppler cells might be allowed in the Doppler cell declaration. In that case, a certain tolerance will be allowed in matching all the A_{ufi}. This naturally brings in clustering algorithms that incorporate various measures for allowing and minimizing error in Doppler cell declaration.

5.1.5 The Clustering Algorithm

A simple form of Clustering Algorithm (CS) [68], [74] is briefly mentioned for demonstration purpose which is adopted from [68] and modified for use in velocity estimation. Let A_{ufi} be as defined earlier, A_{ufoo} be the ordered sequence of A_{ufi} for the o^{th} order, $\overline{A_{ufo}}$ be the median value o^{th} sequence of i ordered unfolded Doppler cells. The average squared error for velocity, $C_v(o)$, for i consecutive ordered Doppler cells in the o^{th} order is given by

$$C_v(o) = \frac{1}{i}\sum_{l=1}^{l=i}\left|A_{ufol} - \overline{A_{ufo}}\right|^2 \tag{5.13}$$

The best cluster is the one with lowest value of $C_v(o)$. Once the best cluster is selected, its unfolded Doppler cell number $\overline{A_{ufo}}$ could be selected and converted to Doppler frequency and then to the Doppler velocity. Eq. (5.3) can be used to convert the unfolded Doppler cell number to the Doppler frequency with the correct sign but we can see that the index of Eq. (5.3) goes to N while the index of Eq. (5.11) goes to infinity. To resolve this difference, the first instance of such best cluster is to be selected when using Eq. (5.13) and the same applies to CRT and CA also.

It also transpires that, given that the permissible error in the declaration of the Doppler cell (remainder) is reduced to zero, both the CA and CS degenerate to GCRT. [75] reports a similar such study about GCRT and CS.

This brings us to the concept of Decodability Constraint.

5.1.6 The Decodability Constraint

The Decodability Constraint applicable to Doppler velocity ambiguity resolution is defined as follows [9] :

$$\mathrm{LCM}(\mathrm{PRF1}, \mathrm{PRF2}, \mathrm{PRF3}, \ldots, \mathrm{PRFi}) \leq f_{Dmax} \tag{5.14}$$

where LCM stands for Least Common Multiple. The above constraint applies to all the Doppler velocity ambiguity resolution techniques in general and the three techniques in particular which are summarized in this paper. If the unfolded/resolved Doppler frequency exceeds f_{Dmax} value, then there will be again an ambiguity. Therefore, a priori knowledge of maximum expected velocity is necessary while deciding about the PRFs to be used in the ambiguity resolution scheme.

A subtle point to note here is all three techniques (i.e. CRT, CA and CS) provide single-sided unambiguous Doppler cell number. That Doppler cell number is then converted to the double-sided Doppler frequency by using Eq. (5.2) and Eq (5.3). N in

Eq (5.3) is replaced by $\mathrm{LCM}(\mathrm{K}1, \mathrm{K}2, \mathrm{K}3, \dots, \mathrm{Ki})$, Ki being the number of Doppler bins in PRFi.

5.2 Experimental Demonstration of Velocity Ambiguity Resolution by use of CRT

5.2.1 Test Setup

The experimental test setup is same as explained in section 4.2.2. The main user programmable parameters of the radar hardware include the number of ADC samples/chirp, frequency slope, number of chirps/CPI, chirp duration, CPI duration, idle time between chirps, idle time between CPIs, etc. The I/Q IF data is obtained in complex number format.

As the target RCS was extremely low, therefore the magnitude of the target echo dropped very rapidly as the distance from the radar increased. Therefore, the radar was placed as close to the airgun muzzle as possible. The difference in this phase of study from the previous phase (Chapter 4) is that a ballistic chronograph was made avaialble in this phase of study. The chronograph was used with the radar to perform another independent simultaneous measurement of the pellet speed. The ballistic chronograph has two optical sensing windows and it measures the speed of pellet by measuring the time elapsed between two instances when the pellet passes across each of the two sensing windows. The ballistic chronograph has a stated accuracy of ±5% of measured speed. The radar is placed between the two sensing apertures of the ballistic chronograph so that the speed measurement arrangement for the radar and for the chronograph is as similar as possible. Figure 5.2 shows the actual experimental setup with the addtion of the ballsitic chronograph.

Figure 5.2 Field Experiment Setup with Ballistic Chronograph

5.2.2 Tuning and Optimization of Radar Hardware Parameters

Using the fact that $\text{PRF} = 1 / T_c$ and using Eq. (5.1) without a minus sign, we can simply write Eq. (5.2) as follows for double-sided relation

$$-\frac{1}{2T_c} \leq \frac{2v}{\lambda} < \frac{1}{2T_c} \tag{5.15}$$

which also gives single-sided $v_{r,max} = \lambda / 4T_c$, as in Eq. (4.6). The maximum unambiguously measurable velocity is dependent only on the carrier frequency wavelength, λ, and chirp time, T_c, or alternatively, the PRF. For increasing the maximum measurable velocity, T_c needs to be reduced; however, naturally there has to be a hardware defined lower limit for the T_c. T_c is mainly governed by the number of ADC samples/chirp and the ADC sampling frequency, F_s, and it is straightforward to note that in ideal and simple conditions, $T_c = (\text{No. of ADC samples}) / F_s$. One noteworthy point here is to observe that in ideal conditions, T_c, will not have any idle or non-sampling time, however in the actual scenario, there is always an idle non-sampling time at the start of chirp. Furthermore, FMCW radars mostly use Phase Locked Loops (PLLs) as frequency synthesizers and the PLLs require a certain reset time at the end of chirp to bring the output frequency down to the start of carrier frequency for the next chirp. This usually results in having another idle time at the end of the chirp. The comparison of ideal and practical chirp is shown symbolically in Figure 5.3. One needs to be careful to note that in practical scenarios, T_c will have additional idle time segments at the start and end of chirp [23]. These aspects need to be kept in mind when deciding about the required frequency slope.

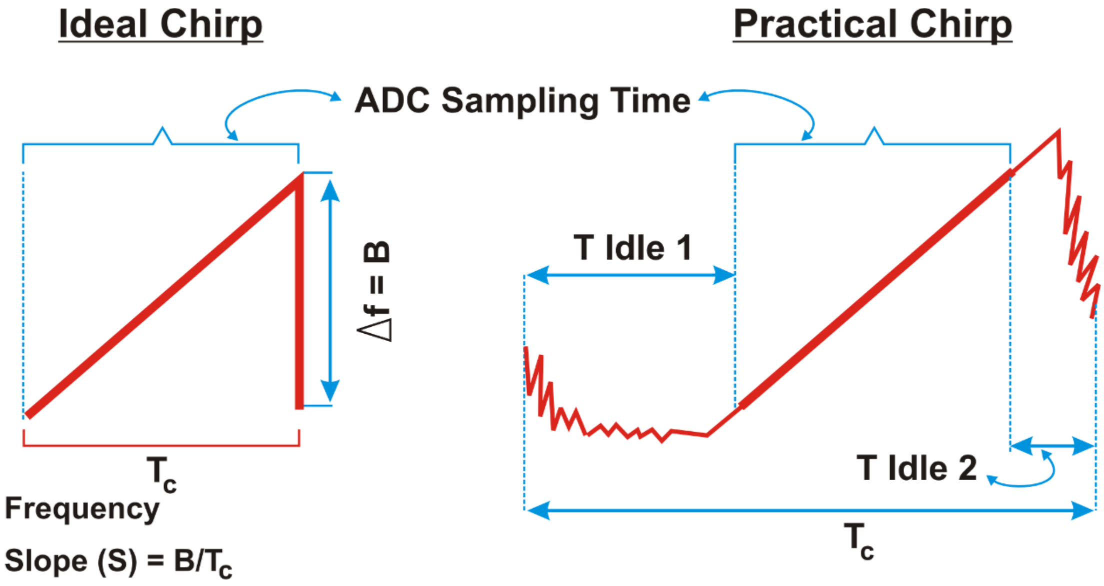

Figure 5.3 Ideal and Practical LFM Chirp

The frequency slope (S) is another important parameter that defines the maximum unambiguous range by the relation $R_{max} = (F_s\ c)\ /\ 2S$. Considering the maximum possible value of S that could be set, the range is kept at a minimum for this experiment so that possible reflections from the targets present at farther ranges are avoided. Another point to note here is that very strong reflectors at ranges greater than R_{max} may still appear in the range profile with folded ranges (range ambiguity phenomenon); however that would be a quite complex and intricate situation. More often, the approach of limiting the value of R_{max} to the range of interest by accordingly setting the value of the frequency slope, usually excludes the unwanted echoes from farther ranges.

As discussed before, T_c is also dependent on the number of ADC sampled/chirp and a higher number of ADC samples might be tempting because it will provide finer range resolution (if needed). However, at the same time, a higher number of ADC samples will increase the chirp time and observation time as well, which might be desirable or otherwise. In the case of very fast-moving targets, especially those with very small RCS, one needs to realize that a longer chirp duration (in part due to a higher number of ADC samples) will result in target echo magnitude dropping very rapidly during the observation window. In addition, in certain scenarios, the target motion dynamics may even change during the observation window. The radar platform used in this study allows minimum 64 ADC samples in given preferable configuration. In view of this, the minimum T_c with a minimum of 64 ADC samples and maximum F_s (~5.5 MHz) was selected which gave a ball-park figure with T_c value of ~26 μs (including ADC sampling time and idle times). With a minimum T_c value of ~26 μs, a maximum single-sided velocity of ~68 m/s could be measured by using Eq. (4.6). Any velocity above this velocity would pose an ambiguity problem when measured with this radar platform and with these parameters.

As this chapter is based on velocity measurement by 2D FFT method, therefore, a certain number of chirps are combined into a subframe which is in fact a CPI. The target under study is a single point target and theoretically two CPIs can be used to resolve the velocity ambiguity; therefore, two sub frames are used. These two subframes are then combined into a single frame. From a theoretical and signal processing viewpoint, there is no difference between a subframe and frame mentioned here, however, this distinction is needed due to hardware specific constraints. A burst of total 800 frames was transmitted and the airgun was also fired simultaneously. Synchronization between radar transmission and airgun firing was not possible, neither it was deemed to add much value, so this operation was performed manually. This resulted in the detection of target in different frames during the conduct of experiment. Figure 5.4 shows the relation of chirp, subframe and frame where Ki is the number of chirps/CPI. The inter-subframe and inter-frame times were kept to the minimum possible.

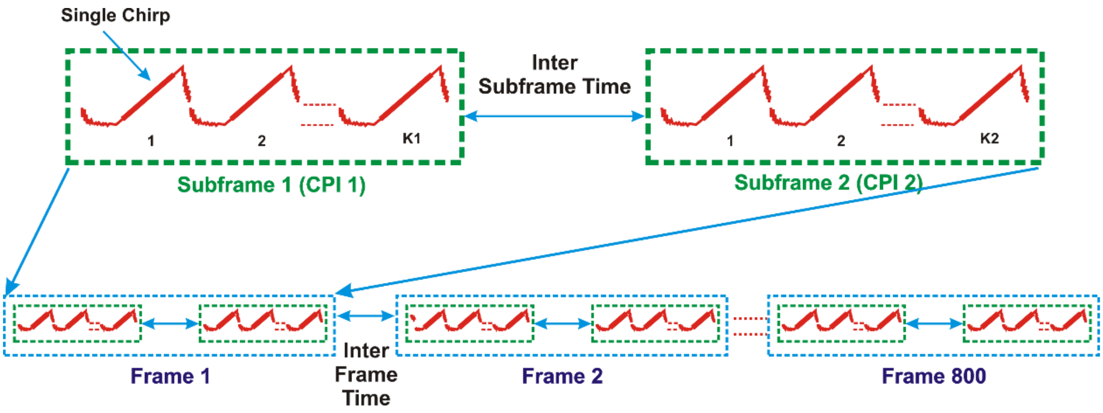

Figure 5.4 Chirp, Subframe and Frame Configuration

5.2.3 Parameters Selection for CRT Application vis-à-vis Test Scenario Constraints

A concise ab inito application introduction to CRT by use of simulation results is presented in [76]. However, the worse case application scenario at hand has certain peculiarities that further make the CRT application difficult. The major consideration is that the target is visible only for a relatively short time in the radar Field of View (FoV), refer Figure 4.6. The target enters the radar FoV and then it exits the radar FoV quickly due to its relatively high speed. It is analogous to say that dwell time is quite less. Therefore, out of the transmitted 800 frames, the target will be only visible in a small number of frames. The second difficulty, as discussed earlier, is that owing to the extremely small RCS of the target, the target echo magnitude falls very rapidly as the distance increases. This makes the target observation in later CPIs increasingly difficult even if the target is still within the radar FoV. This calls for the number of PRFs, number of chirps/CPI and time for chirp and CPI to be as short as possible. On the other hand, if the number of chirps/CPI is reduced significantly, say less than 10, then the Doppler resolution gets quite worse.

It is usually advisable to better have at least three PRFs for the application of CRT or similar ambiguity resolution techniques. However, theoretically, two PRFs should be able to resolve velocity/range ambiguity for a single target, preferably a point target. Initial work on the problem at hand included tests with three PRFs with lesser number of chirps/CPI (9,7,5) however this approach was abandoned in favor of a more rigorous attempt to resolve velocity with just two PRFs. Almost minimum possible chirp time was used for this study so that the CPI time was kept to a minimum for the two reasons mentioned above.

Generalized CRT (GCRT) requires that the bases (number of Doppler cells in this case) should be co-prime, implying that their Greatest Common Divisor (GCD) is 1. As mentioned earlier, the data was processed without any zero-padding and without any truncation. No windowing operation was performed either. This was done on purpose to keep signal processing as basic as possible and to study target detection and speed ambiguity resolution scenarios as unaided as possible. Without zero-padding, the Doppler cell resolution will be $\Delta f_D = \mathrm{PRF} \;/\; (\mathrm{No.\,of\ chirps\ in\ CPI})$. At this point, there could be two options - either to keep the Doppler resolution of both CPIs constant and change the length of FFT in both CPIs or to keep the FFT length constant and change the Doppler resolution in the two CPIs. Keeping the FFT length same in both the CPIs will necessarily imply zero-padding in at least one CPI. In view of this, it was decided to keep the Doppler resolution constant among the two CPIs as it would also ease CRT application. This brings forth the following condition:

$$\Delta f_D = \Delta f_{D1} = \Delta f_{D2} \tag{5.16}$$

where

$$\Delta f_{D1} = {}^{\mathrm{PRF1}}/_{\mathrm{K1}} = {}^{1}/_{\mathrm{K1}T_{c1}} \tag{5.17}$$

and

$$\Delta f_{D2} = {}^{\mathrm{PRF2}}/_{\mathrm{K2}} = {}^{1}/_{\mathrm{K2}T_{c2}} \tag{5.18}$$

where T_{ci} is the chirp time and Δf_{Di} is the width of the Doppler frequency cell for the i^{th} CPI. Likewise, the width of the Doppler velocity cell is well-known to be given by

$$\Delta v = {}^{\Delta f_D}/_{2\lambda} \tag{5.19}$$

The maximum single-sided unambiguous velocity, $v_{iss}(\mathrm{max})$, from i^{th} PRF could be calculated as

$$v_{iss}(\mathrm{max}) = \mathrm{Ki}\Delta v \tag{5.20}$$

Note that the velocity cell in both the CPIs is the same, but the number of cells differ. Given that, we have A_{a1} and A_{a2} as observed ambiguous Doppler cell numbers in CPI1 and CPI2 respectively, then, the resolved Doppler cell number by CRT is denoted by $k_{CRT} = C_{resolved}\mathrm{mod}(\mathrm{K1K2})$, where $C_{resolved}$ is the cell/column number resolved using CRT. The maximum value of the resolved cell, $k_{CRT}(\mathrm{max})$, is deduced from the decodability constraint given in Eq. (5.14), as follows [73]:

$$k_{CRT}(\mathrm{max}) = \mathrm{LCM}(\mathrm{K1K2}) \tag{5.21}$$

so with coprime K1 and K2, it is just K1K2. Likewise, the maximum resolvable single-sided Doppler frequency is given by

$$f_{DCRT}(\max) = \Delta f_D \mathrm{LCM}(\mathrm{K1K2}) \tag{5.22}$$

And maximum resolvable single-sided Doppler velocity is given by

$$v_{CRT-ss}(\max) = \Delta v \mathrm{LCM}(\mathrm{K1K2}) \tag{5.23}$$

As the Doppler spectrum is double-sided which facilitates the measurement of positive and negative Doppler velocities, therefore, the double-sided maximum resolvable velocity by this CRT example is given by

$$v_{CRT-ds}(\max) = \pm {}^{v_{CRT-ss}(\max)}/_{2} \tag{5.24}$$

Eq. (5.16) ~ Eq. (5.24) help to define the Doppler frequency resolution, velocity resolution, maximum Doppler frequency, maximum measurable single-sided and double-sided velocity etc. The actual velocity was measured by using CRT to derive k_{CRT} from the A_{a1} and A_{a2} obtained from the RD-maps of the two CPIs. Then an important and cautious step is to convert k_{CRT} to double-sided Doppler cell number, k_{CRT-ds} as follows, in lines with Eq. (5.3)

$$k_{CRT-ds} = \begin{Bmatrix} k_{CRT} & if\ 0 \leq k_{CRT} < \frac{1}{2} N_{CRT} \\ -(N_{CRT} - k_{CRT}) & if\ \frac{1}{2} N_{CRT} \leq k_{CRT} < N_{CRT} \end{Bmatrix} \tag{5.25}$$

where $N_{CRT} = \mathrm{LCM}(\mathrm{K1K2})$.

Note the subtle point here that the Doppler cell numbers are being used here, both for the ambiguous and the resolved cases and the relations for the Doppler frequency are not being used. This is because GCRT works on whole numbers and Doppler cell numbers are given in whole numbers. As discussed earlier, there are versions of CRT that work with non-integers also but that is beyond the scope of this thesis. Also note that the index of Doppler bin number is from $0 \rightarrow (N-1)$ in Eq. (5.3) and Eq. (5.25). Once k_{CRT-ds} has been determined, it is converted to the resolved unambiguous velocity by using the simple relation

$$v_{CRT-ds} = k_{CRT-ds}\Delta v \tag{5.26}$$

Note that the velocity cell Δv is the same for single- and double-sided interpretation of velocity.

As discussed above, the very rapid decay of the return echo magnitude with distance and very small observation time, compelled the use of two PRFs. The relevant parameters for the two PRFs were selected, tuned and calculated using the above equations. The summary of the parameters optimized for this experiment is presented in TABLE II.

Note that although chirp times are different for the two PRFs, however, the ADC sampling time, number of ADC samples, ADC sampling frequency, frequency slope and modulation bandwidth are kept constant in both the PRFs. Of course, some researchers/practitioners could study and implement the CRT regime by varying one or more of these parameters, however, in this study, these are kept constant so that the number of variables is kept at a minimum and the GCRT only needs to resolve the ambiguous Doppler cell number. If one or more of these parameters are changed from one PRF to the other, then the Doppler cell resolution will not remain the same and hence it will not be possible to work on the Doppler cells indices as whole numbers. In that case, CRT would need to be used for resolving Doppler frequency which may or may not be in whole number and besides that, it will make the CRT implementation needlessly difficult.

Also notice in TABLE II, the much smaller maximum measurable unambiguous velocity limits for both PRFs ($v_{iss}(\max)$) individually and how the use of CRT dramatically increases the maximum measurable velocity limit, $v_{CRT-ss}(\max)$.

TABLE II SELECTION AND CALCULATION OF PARAMETERS

Symbol	Description	Quantity with units
f_c	Carrier frequency	77 GHz
$NumADC$	Number of ADC samples/chirp	64
F_s	ADC sampling frequency	5.5Msps
S	Frequency slope	95.015 MHz/μs
B	(Modulation) Bandwidth	1.1056 GHz
$K1$	Number of Chirps in Subframe 1 (CPI1)	17
$K2$	Number of Chirps in Subframe 2 (CPI2)	15
T_{c1}	Chirp Time in CPI1	25.40 μs
T_{c2}	Chirp Time in CPI2	28.79 μs
T_{c1ADC}	ADC sampling time for chirp 1	11.63 μs
T_{c2ADC}	ADC sampling time for chirp 2	11.63 μs
Δf_{D1}	Doppler frequency cell width for CPI1	2315.61 Hz
Δf_{D2}	Doppler frequency cell width for CPI2	2315.61 Hz
Δv_1	Velocity cell width for CPI1	4.52 m/s
Δv_2	Velocity cell width for CP2	4.52 m/s
$v_{1ss}(max)$	Single-sided max unambiguous velocity for CPI1	76.77 m/s
$v_{2ss}(max)$	Single-sided max unambiguous velocity for CPI2	67.73 m/s
Δf_D	Doppler frequency cell width (for CRT)	2315.61 Hz
Δv	Velocity cell width (for CRT)	4.52
$k_{CRT}(max)$	Maximum value of CRT resolved cell	255
$v_{CRT\text{-}ss}(max)$	Maximum resolvable single-sided velocity	1151 m/s
$v_{CRT\text{-}ds}(max)$	Maximum resolvable double-sided velocity	±575 m/s

5.2.4 Consideration of Zero-Doppler Column in PRF Parameters Selection

The zero-Doppler column gains some significance while deciding the values K1 and K2. We must remember that certain non-zero Doppler frequencies fall in the zero-Doppler column after aliasing [77]. We also need to consider that for a N-point time domain signal, the frequency domain signal after FFT operation will contain one DC value cell and the remaining $(N-1)$ non-zero frequency cells. Thus, for a convenient presentation, we decided to keep the number of FFT points (number of Doppler bins) as an odd number so that the zero-Doppler column will be in the exact center of RD-map, making it symmetrical about the zero-Doppler column.

5.2.5 FFT, Aliasing and Basic Signal Processing Related Aspects

The ADC data was acquired from the radar and it was post-processed in offline mode using MATLAB. Length of 1st FFT was set equal to number of ADC samples/chirp. The length of 2nd FFT was set equal to the number of chirps/CPI. A small detail to consider during FFT operations is to pay attention to the index numbering. In MATLAB, the array index runs from 1 to N – in our case N is the number of FFT points and thus the zero-Doppler column is at MATLAB's index one rather than at index 0 as stated in standard radar texts. Then, `fftshift()` operation of MATLAB was used to bring the zero-Doppler column to the center of the RD-map.

A quick discourse about the aliasing and folding of signals having frequency greater than Nyquist frequency, is relevant here. The ADC samples the IF signal with sampling frequency, F_s, and the Nyquist frequency in this case will be $F_S / 2$. An IF signal with more than $F_S / 2$ frequency will be aliased and that will give incorrect results for the range profile.

The slow time dimension of the radar data matrix is sampled at the rate of PRF (as opposed to fast time dimension which is sampled with the rate determined by ADC sampling clock). The Nyquist frequency in this case would be PRF $/ 2$.This brings us back to the discussion in section 5.1.1 and Eq. (5.3). When the Doppler frequency exceeds PRF $/ 2$ but its value is still less than the value of PRF, then this Doppler frequency falls into the negative part of the Doppler spectrum whose value is given by Eq. (5.3).

In the context of Nyquist criteria, the frequency spectrum is divided into an infinite number of Nyquist zones with each zone having a width of $0.5F_S$, where all the zones except the zone of the signal of interest, are called image zones [78]. This tutorial is based on usage of IF I/Q signal. IF signals are, mostly, baseband signals and same is the case with the hardware platform used in this experimental study. In the baseband signal, the signal of interest is contained in the first Nyquist zone while in bandpass signals the signal of interest is contained in a Nyquist zone other than zone 1. It is also well-known that phase reversal occurs when the signal falls after aliasing in an even numbered Nyquist zone [78], [79]. This causes the mirror image effect of Eq. (5.3) for the negative frequencies. The negative frequencies (after 2D FFT) signifying opposite Doppler direction, thus become meaningful and understandable in the Doppler domain while they are meaningless in the physical sense for the 1D FFT range profile as the range cannot be negative. Figure 5.5 spectrograms summarize these concepts which is adopted from [78].

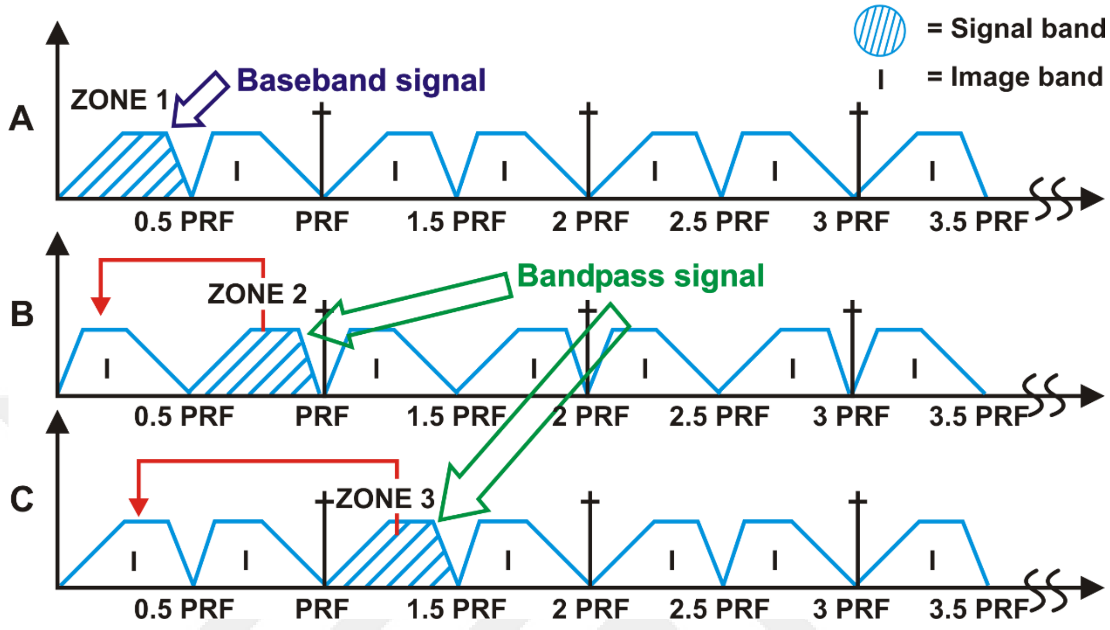

Figure 5.5 Nyquist zones for baseband and bandpass signals

The y-axis in Figure 5.5 shows the magnitude and the red lines show the translation of bandpass signal zones to the baseband signal zone (with or without phase reversal). We just need to be mindful that for baseband range profile, all zones beyond zone 1 are image zones and aliasing occurs when frequency exceeds $0.5F_s$. However, for Doppler profile, the zone 1 ($0 \rightarrow 0.5\text{PRF}$) and the zone 2 ($0.5\text{PRF} \rightarrow \text{PRF}$), both contain non-aliased information for positive and negative Doppler frequencies, respectively. Beware that the conventions ($0.5\text{PRF} \rightarrow \text{PRF}$) and ($-0.5\text{PRF} \rightarrow 0$) are used interchangeably and Eq. (5.3) comes in handy in that place. It is also to be noted that the phase reversal is another way of describing the idea of negative frequencies. It may be easier to think of phase reversal with a real-valued signal in mind, and about negative frequencies with a complex-valued signal.

The aliasing occurs for Doppler frequency beyond the value of PRF. It further means that all multiples of PRF will fold/alias into the zero-Doppler bin. In order to easily distinguish our moving object echo from the ground clutter, it is desirable to keep the Doppler frequency of our echo far from any integer multiple of PRF. A target echo falling into the zero-Doppler column will be difficult to observe, although this possibility will be still discussed further in the section 5.3.6. The zone and location of target echo can be estimated in Doppler dimension with the following relation:

$$f_D \Big/ \left(\Delta f \times \left({}^{\mathrm{Ki}}\!/_{2} + 0.5\right)\right) = X + y \tag{5.27}$$

where Δf is the width of the Doppler frequency cell, X is the whole number part of the quotient and y is the fractional part of the quotient.

The Doppler frequency under consideration will occupy the (X+1)th Nyquist zone and the Doppler echo will be in the middle of the (X+1)th zone if $y \rightarrow 0.5$. Eq. (5.27) can be used to tune the values Δf and Ki, provided that the value of f_D is known which requires an a priori estimate of the velocity. Note that y should be just used to tune the radar parameters so that $y \rightarrow 0.5$. The value of y will have different connotations for even and odd zones therefore it is much easier to use Eq. (5.3) if an estimate of target echo position is desired within a zone. For an estimated velocity of 221 m/s, f_D, comes to be 113.53 kHz. From the TABLE II, for the Δf_D value of 2315.88 Hz, we get the result of 5.45 for K1 and 6.13 for K2 by using Eq. (5.27). There has to be a tradeoff that y in Eq. (5.27) can be set how much near to a value of 0.5 for different PRFs. A value of 5.45 implies that the target echo for K1 PRF can be expected to fall in the (5+1) 6th Nyquist zone and it can be expected to fall in the middle of the Nyquist zone as y = 0.45. It also implies that as the 6th Nyquist zone is an even zone, therefore, the target echo for K1 PRF will be expected to fall into the negative Doppler zone after aliasing with an aliased Doppler frequency in the range $(-0.5\mathrm{PRF} \rightarrow 0)$. By similar reasoning, the target echo for K2 PRF is expected to fall in the first Doppler zone after aliasing. These zone inferences for positions of target echoes in the two CPIs also tally with the experimental data of Figure 5.8 for a measured speed of 221 m/s.

Once the 2D FFT operation has been performed, the cell with the maximum complex magnitude is selected as target location in the RD-map for this tutorial study. There are certain techniques for automated target detection such as various versions of Constant False Alarm Rate (CFAR) algorithms. However, in this study, we assume that observable peak locations are detectable with straightforward selection of cell with maximum magnitude.

The Doppler column numbers obtained from the RD-maps were used as the input for CRT. As each frame comprises two subframes therefore readings corresponding to two CPIs within one frame are used as the input for CRT.

5.3 Results of Experimental Study and Discussion

After determination of the experimental setup and tuning and selection of the radar parameters, extensive field tests were carried out. The actual field data gathered during this study was subjected to processing for CRT implementtation for resolving velocity ambiguity. The salient results are provided as TABLE III of Annexure A. These include numerical results from Range-Doppler processing, CRT results for velocity ambiguity resolution and the respective chronograph readings. Note that the Doppler column indices are given in “MATLAB” convention (i.e. starting from 1). The frames (CPIs) are also mentioned for each test in which target was located. This will help to identify the required frames (CPIs) data from the transmitted 800 frames which will be of value when other researchers may process the raw data at their own.

5.3.1 Measurement Allowances, Conformity and Accuracy of the Results

The first set of experiment involved 13 tests (TABLE III of Annexure A) with two types of pellets. The pellets of course have the same bore size but slightly different weights and shapes. Figure 5.6 shows the two types of pellets used in this study and the demonstration.

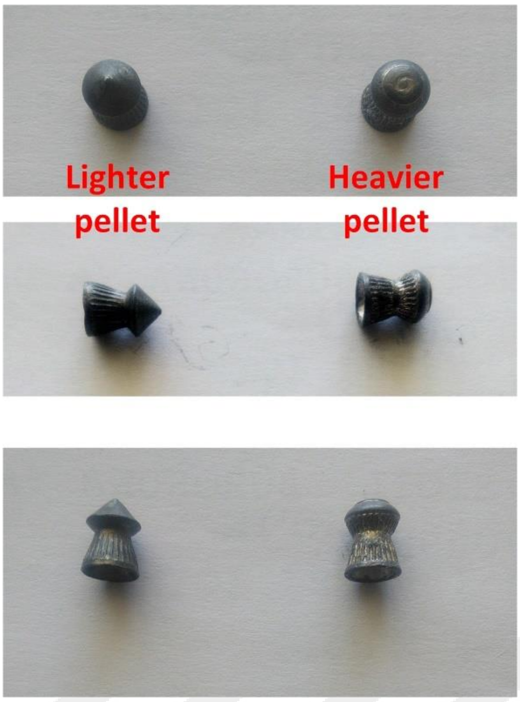

Figure 5.6 Two types of 5.5mm airgun pellets used in the experiment

It was observed that the airgun was firing the bullets with speed somewhat less than the expected speed. Therefore, towards the end of the study, the parameters were tuned slightly differently for an estimated speed of 200 m/s and two types of pellets were used as shown in Figure 5.6. Tests 18~22 in TABLE III pertain to this activity. It is understandable that commercially available airguns are not quite accurate tools and the pellets are also not very precisely made. Therefore, there could be differences in the speeds of same type of pellet in different shots and the speed could also be expected to differ from one type of pellet to the other. In addition, we also need to consider the FFT quantization margins related to the FFT bin width. However, in spite of all these factors, we can see from TABLE III in Annexure A that the results of speed measurement with the CRT and with ballistic chronograph tally fairly well with each other. The comparison of the speed measurement by the CRT and the chronograph is shown pictorially in Figure 5.7. It can be seen that the CRT results are consistent and accurate but the chronograph has produced a few erroneous results as well.

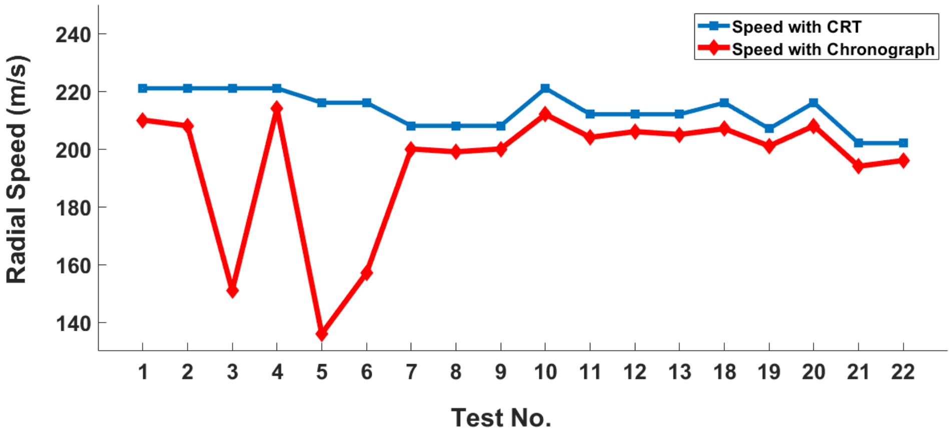

Figure 5.7 Comparison of airgun pellet speed measured by the CRT and ballistic chronograph (Refer TABLE III)

This demonstrates that despite all its perceived shortcomings, CRT has been able to correctly resolve ambiguous velocity. The use of statistical methods is well known to introduce robustness in CRT for high-noise cases while deterministic methods are said to work well mainly in low-noise cases [80] but it is seen in this research that even in very low SNR case, the CRT has been demonstrated to operate well with judicious selection of radar parameters. This experiment can be called as low SNR case because the magnitude of the target is quite feeble.

There is not a single true value for all measurements of TABLE III due to reasons mentioned earlier. The true value of each individual measurement is assumed to be midway between the measurements from the CRT and the chronograph. The outlier chronograph measurements of test number 3, 5 and 6 from Figure 5.7, are discarded and the remaining measurement results are used to calculate average accuracy of radar measurements with the CRT. The average accuracy is calculated to be 98.0% for CRT measurements.

5.3.2 A Peculiar Phenomenon

It is observed that in every measurement, the CRT result from the first set of two CPIs is incorrect. The primary reason for this occurrence is that the angle of the pellet projectile with radar FoV varies significantly as the pellet initially enters and then travels through the radar FoV and this changes the apparent radial velocity. This angle is comparatively larger at the start and it decreases significantly as the pellet travels further in the radar FoV. As a result, a higher apparent radial velocity or even radial velocity with the opposite sign is observed in first of the two CPIs of the first set. This aspect is discussed in detail in [81]. Note that if the observed radial velocity is incorrect in even one of the two CPIs, the CRT results will be grossly wrong.

This peculiar phenomenon could be probably avoided if a target (preferably with uniform RCS e.g. a metallic sphere) could be fired with required speed along the radar boresight instead of traversing across the radar FoV. This might be theoretically possible but could be probably practically challenging. However, some interested researchers may make this endeavor, if desired so.

5.3.3 Consistency of the Results

As it was not possible to synchronize the trigger of radar transmission and airgun trigger, therefore, the target was detected in different frames in different tests. As elaborated in section 5.2.1, the radar was placed fairly near to the airgun muzzle. Therefore, it can be assumed with caution that speed of pellet was fairly constant during the observation time. The same was validated by consistent velocity readings from the second to fourth or fifth frames in which the target was detected. Figure 5.8 is shown as sample result for test 4 from TABLE III. Notice that the target echo location in the first CPI for the first observation frame is inconsistent with the remaining frames and the result from first frame is incorrect also in TABLE III. Furthermore, observe the consistency in the target location in the cprresponding CPIs for successive frames.

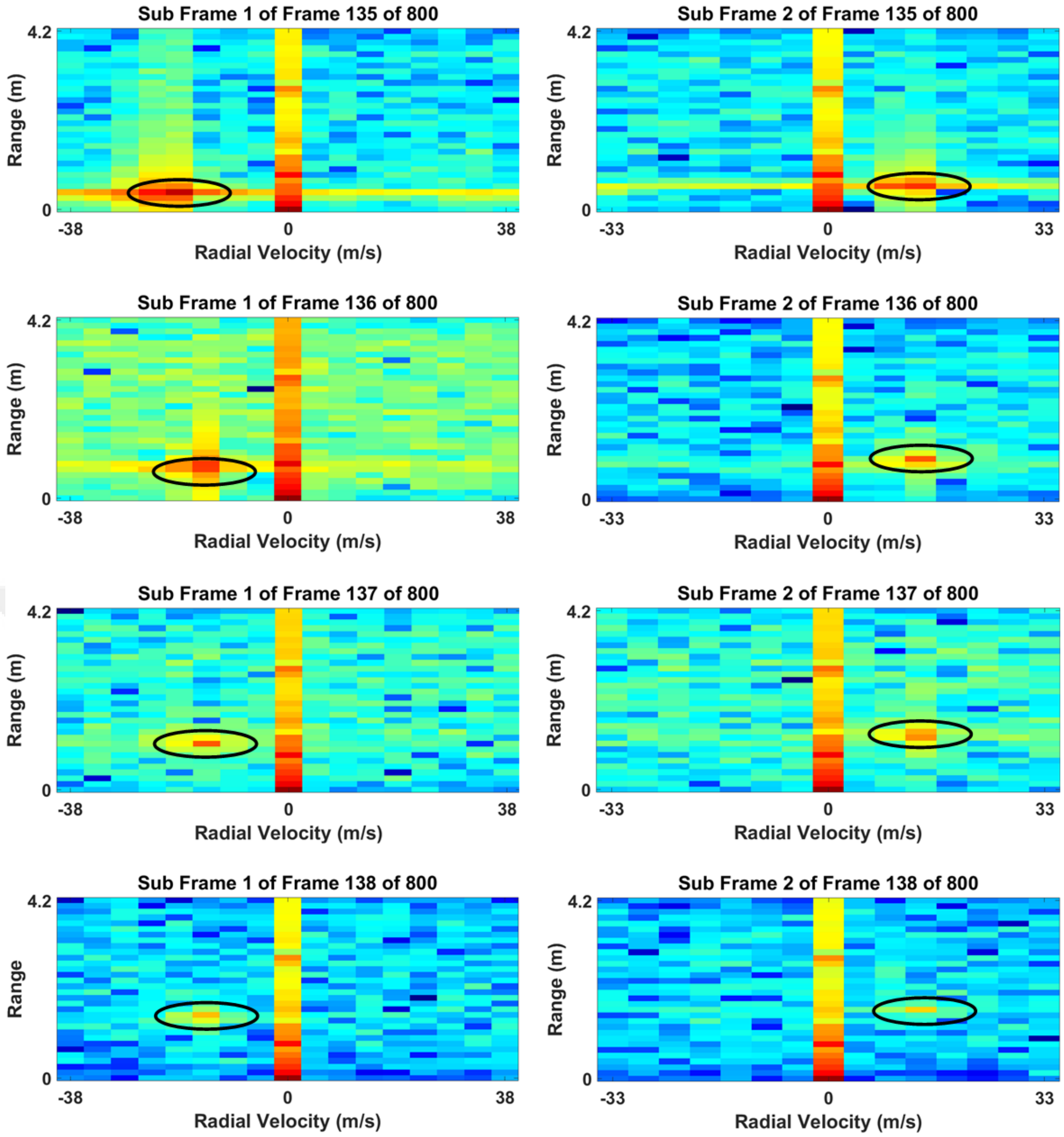

Figure 5.8 Range-Doppler heatmap (magnitude) for test 4 of TABLE III (target encircled in black ellipse, target Doppler bin number indicated by black dotted line)

One aspect needs to be considered here. The certainty about the correct CRT results in this study is established on the basis of consistency in the successive velocity measurements by the use of CRT. It is based on the assumption that the velocity is consistent during the observation/measurement time which is in fact the case. However, if velocity is changing rapidly during the observation time and if it is changing from one frame to the next then it would be very difficult to ascertain whether CRT is giving correct results.

5.3.4 FFT Processing Gain

The significance of the incoherent processing gain of FFT in the 2nd FFT pass is also observed experimentally during this study. The FFT processing (incoherent integration) gain is given by $\sqrt{M}$ where M is the number of FFT points in 2nd FFT direction. To be a little precise, the incoherent integration gain (in FFT) is given by a value between $\sqrt{M}$ (minimum for the noncoherent integration) and M (for coherent integration) [9], [82], [38]. It has been described earlier that the target has an extremely small RCS and it can be seen physically in Figure 5.8 that the target echo magnitude drops quickly as the frames progress. The same can be seen in all results from TABLE III of Annexure A. It has been further observed that in the later frames, the target is not visible in the 1D FFT range profile but the target becomes discernible in the 2D FFT RD-map (after 2nd FFT).

5.3.5 A Crude Test to Partially Check the Constant Velocity

Tests 14~17 of TABLE III were conducted to make sure that the velocity reading from several CPIs is constant. For test 14 and 15, K1=K2=17. For Test 16 and 17, K1=K2=15. Note that the velocity measurements made here cannot be used with CRT for resolving the ambiguity because the numbers of Doppler cells in the two PRFs are not coprime. However, the consistent target echo location in both CPIs of each frame (frames 3 and 4 and in some cases frame 2) indicates that although the velocity measurement is (possibly) aliased, but it is consistent.

5.3.6 Revisit to Zero-Doppler

It was observed that in some of these tests, the target echo fell in the zero-Doppler column (shown as column index 1 in TABLE III of Annexure A). This was an undesirable situation due to clutter presence in this column. Without clutter, a target falling in zero-Doppler column is not a problem, because that location of Doppler frequency is still a valid measurement for use in CRT. For the two-PRF example under consideration, it is logically impossible for a constant velocity target to fall in the zero-Doppler column in both the PRFs because it will imply $A_{a1} = A_{a2}$. Note that equal velocity readings with two different PRFs [83] are possible only if the true velocity is in the unambiguous range for each PRF (i.e. it is very low – not our case), or it is higher than the maximum resolvable velocity (Eq. (5.23)) (again – very high, more than 1152 m/s in our case). Another cause of equal readings might be that the velocity of target was significantly changing between CPIs (a hypothesis which we hopefully excluded with tests described in section 5.3.5).

1) PHYSICAL ORIGINS OF ZERO-DOPPLER

The mathematical and theoretical origins along with some physical origins of the zero-Doppler column have been discussed earlier in section 5.2.4. In addition, there are certain hardware oriented physical phenomena that give rise to target peaks in range profile which are very close to zero range and as they essentially have zero-velocity nature therefore they all sum up indistinguishably within the zero-Doppler column.

The main contributors among them are the transmitter leakage effect into the mixer in the FMCW architecture [84] and transmitter and receiver antenna coupling as well as the possible sources of DC component in the signal. Another factor is the already mentioned stationary echoes contribution. Additionally, in naturally occurring data, there is another phenomenon known as 1/f noise that manifests itself in the actual field data [64]. The point to stress here is that there are certain complex and interconnected physical phenomena which will most probably not usually surface in theoretical and simulation studies (as for example [85]), however, they arise in actual hardware-based experiments.

2) TARGET DETECTION IN ZERO-DOPPLER COLUMN

Reverting back to the discussion at hand, the zero-Doppler might not be a problem from a purely theoretical perspective. However, it is observed that in the field data in hardware-oriented studies, the zero-Doppler column is a fairly real and important phenomenon which can be troublesome as well at times especially in cases of velocity ambiguity resolution by means of multiple PRFs. This problem becomes more pronounced when the aliased target echo falls in a frequency bin adjacent to the zero-Doppler column. The zero-Doppler column already has higher energy than the rest of RD-map except possibly for the target location in the rest of the RD-map. When a zero-Doppler cell contains a target or contains energy spread from the target in an adjacent cell, then the zero-Doppler cell may have a (slightly) higher echo magnitude than the adjacent Doppler cell with the correct target location. A peak search will thus wrongly select a cell in the zero-Doppler column as the target location instead of the correct adjacent cell outside the zero-Doppler column. This will naturally produce the wrong results. This situation can be witnessed in the last CPIs of tests 12 and 13 of TABLE III of Annexure A. Using the zero-Doppler (index 1) column produces wrong results for the last CPIs of tests 12 and 13. Also notice that the zero-Doppler column has the higher echo magnitude energy than the adjacent correct 2nd column. This situation has arisen due to the fact that although the target is correctly located in the 2nd column (as evident by the correct resolved velocity) but the target echo magnitude in the correct cell has fallen lower than the magnitude of the adjacent zero-Doppler cell.

Therefore, for a constant velocity scenario, a preferable solution for such a situation is to increase the number of PRFs so that the echoes falling in the zero-Doppler column could be ignored and velocity could be resolved by using the results from the remaining PRFs. However, in this particular experiment, it was not possible to increase the number of PRFs. Therefore, the results obtained with the zero-Doppler target echo location were analyzed. It can be seen from the results that CRT is able to produce correct results even when the target echo falls in the zero-Doppler column except in some CPIs of tests 12 and 13.

The important thing is to establish that the target is actually present in the zero-Doppler column and it could be accomplished possibly in two ways which may augment each other as well. One possible way is to consider the energy leakage around the target location. In the absence of a clear target echo in the RD-map in the area outside the zero-Doppler column, a target may be assumed to be located in the zero-Doppler column if a symmetrical or nearly symmetrical energy spread is observed around the apparent target location in the zero-Doppler column. This may also be coupled with observing and comparing the zero-Doppler column when no moving target is present in the RD-map and when a moving target is suspected to be present in the zero-Doppler column. This situation is shown in Figure 5.9 which shows the RD-maps for subframe two (CPI2) from test 22 in TABLE III of Annexure

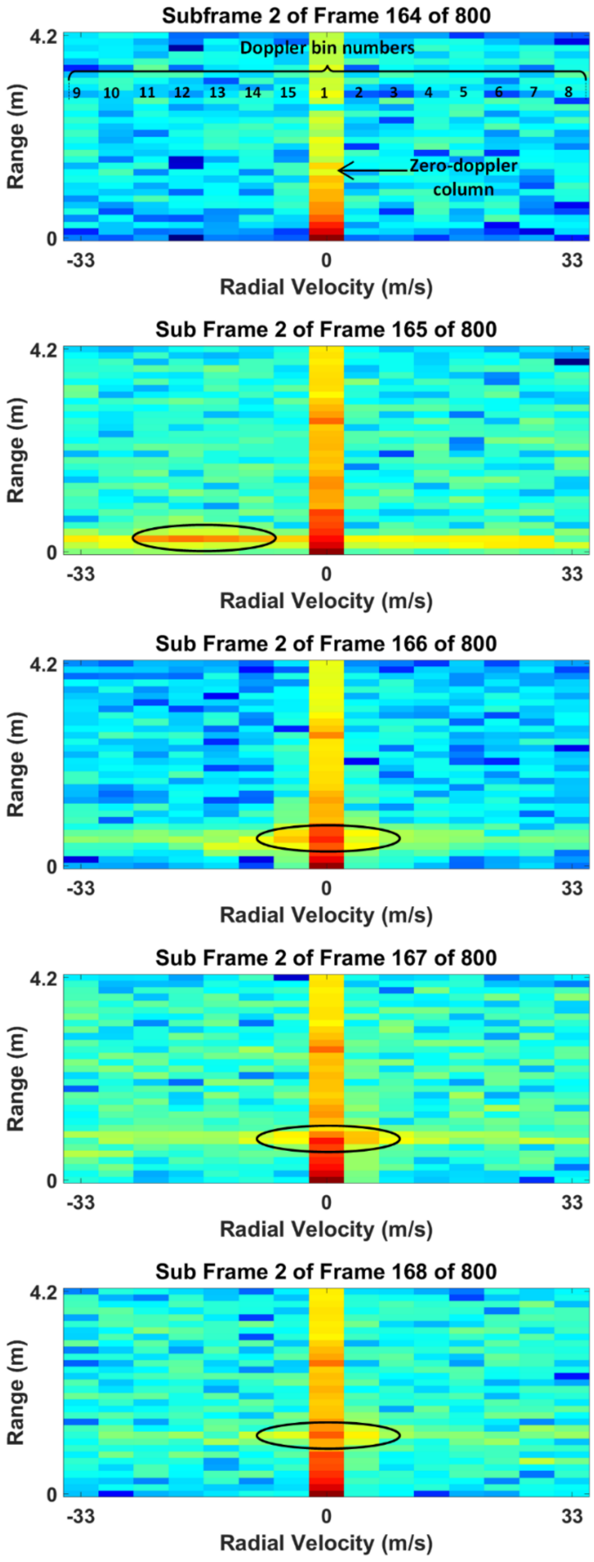

Figure 5.9 Range-Doppler heatmap (magnitude) for test 22 of TABLE III (target encircled in black ellipse, target Doppler bin number indicated by black dotted line)

The first RD-map shows the CPI in which no target is present. The 2nd RD-map shows a single target with an extended energy spread. The next three RD-maps in Figure 5.9 show the target located in the zero-Doppler column. The gradual travel of target in range dimension can also be seen in the last three RD-maps. Of course, this target detection is based on the premise that there is no significant change in the stationary target scenario from one CPI to the next.

Indeed, Figure 5.9 is a worst-case scenario describing some ideas to ascertain the target location in zero-Doppler column. This suboptimal approach can be used in the case of velocity measurement in this tutorial because the location of target along the range axis is not a point of concern. Therefore, it is easier to localize a target in the Doppler column than in a Doppler cell in the RD-map. However, the preferable approach should still be to endeavor to make arrangements to the extent possible that the expected target peak does not fall in the zero-Doppler column.

5.3.7 Caution about Energy Spread of Target Echo

We discussed earlier that a simple and general measure of the maximum target return echo has been used as a detection criterion. The Doppler columns indicating the target presence (with the highest FFT power) are shown with black dotted lines in Figure 5.8 and Figure 5.9 and the same can be referred from TABLE III, however, it can be seen in both figures that, there is an energy spread in almost every target echo which covers more than one cell in the Doppler dimension. This needs to be distinguished from the scenario of an extended target observed in the RD-map with less than the maximum ambiguous speed. For example, a walking human being will act as a localized target in the range dimension, but due to movement of various body parts, it will be seen as an extended target in the Doppler dimension because of the different speeds of different body parts [86]. However, typically, the speed of the human target will be less than the maximum measurable speed and hence in case of two or more PRFs, the speed results from multiple PRFs will be hopefully the same.

5.3.8 Error Proneness of CRT, Robust CRTs and Windowing

The standard radar texts and CRT literature widely state that CRT is prone to gross error even if there is an error of one integer – in this case, of one Doppler bin.

The same has been demonstrated earlier with an example in this research study. This is probably the reason that GCRT finds more use in applications like cryptography which require discrete numbers [87]. However, for applications like radar signal processing, frequency estimation and multiwavelength frequency estimation, certain robust CRT algorithms are used. Such robust CRTs derive their robustness from some sort of differential process based on maximum-likelihood estimation, search-based, closed-form or multistage methods [88].

In addition, it is common to observe the use of windowing even in simulation studies to obtain better results. Reference [89] cites one simulation study example of a robust CRT use for the estimation of frequency and direction of arrival. However, it can be seen in this tutorial that with careful consideration of the various parameters and availability of some a priori information, GCRT can produce conforming results in a demanding field application scenario, without the use of windowing, zero-padding or truncation of FFT data. Nonetheless, in more challenging environments, it might become necessary to use robust CRT, possibly further assisted by redundancy with three or more CPIs.

5.4 Conclusive Notes for CRT Application

This chapter is attempted to demonstrate the use of CRT for resolving velocity ambiguity and to include a real-life experiment scenario.

The resolved velocity is up to 5~6 times the maximum unambiguous velocity measurable with a particular COTS FMCW radar. The application of CRT has been demonstrated with a small RCS target (a 5.5 mm airgun pellet), therefore, it can be hopefully employed conveniently in the scenarios involving targets with bigger RCS e.g. automobiles. It is humbly expected that some researchers might find it useful in measuring speeds of targets having speeds considerably higher than the ones usually encountered in automotive scenarios. In addition, the provided dataset might be considered as a small repository for the students, researchers and/or application experts who could either like to repeat the signal processing based on this dataset (possibly for educational purposes) or who may like to apply some other technique(s) on this dataset for further research.

CHAPTER 6

SOME PECULIAR ASPECTS TO CONSIDER IN APPLICATION OF FMCW COTS RADARS

This chapter presents certain peculiar application aspects of use of COTS mmwave automotive radars that were encountered during the research for this thesis . An attempt is made to present only some selected aspects which are relatively less often discussed in the literature. The intended audience will be electrical/electronics engineers who do not have core expertise in radar engineering however they wish to use COTS automotive radars in their own respective fields as quick and readymade solutions.

6.1 Phase of The Transmitted and Received Signals and the Need for Frequency Domain Analysis

6.1.1 Simulation Study

Figure 6.1 shows the simulation of phase of the time domain transmitted signal of Eq. (2.4) where the phase is derived from Eq. (2.3). The values used for simulation are: f_c = 77 GHz, S = 95.015 MHz/µs. The time vector for simulation is formed by using the ADC sampling time for chirp (T_{cADC}) = 11.63 µs, sampling frequency (F_S) = 5500 ksps implying ADC sampling time, $T_s(= 1/F_s)$ = 0.18µs and number of ADC samples/chirp (NumADC) = 64. Initial phase, φ_0, is assumed to be zero for the sake of simplicity. The linear phase-time relationship is evident from Figure 6.1. The phase in Figure 6.1 is directly obtained from the integral of linear frequency in Eq. (2.3), therefore the issue of phase wrapping does not arise here and there is no need to employ phase unwrapping.

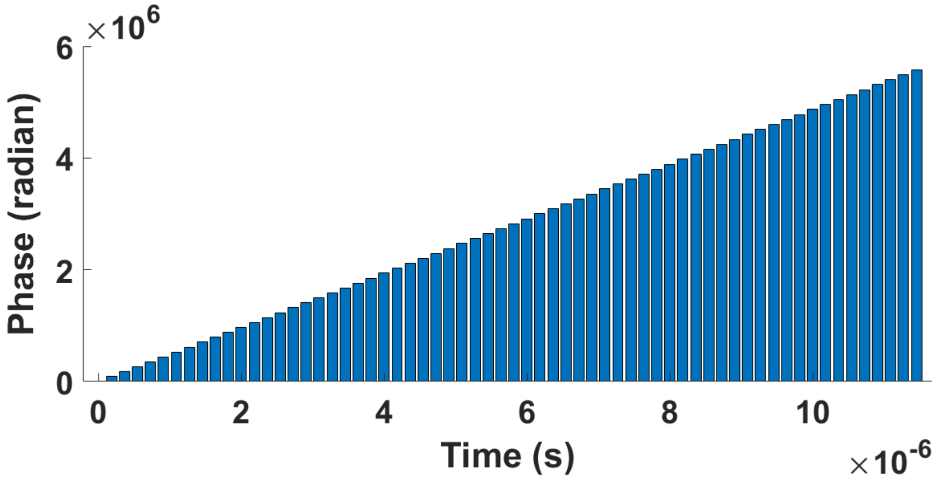

Figure 6.1 Phase of time domain Tx signal (simulation data)

Given that the transmitted signal is given by Eq. (2.4), consider that a part of the transmitted signal is received back at the radar after being reflected and backscattered upon striking a target. This received signal is a time shifted and attenuated copy of the transmitted signal and it can be given by

$$x_{rx}(t) = H\cos\left(2\pi\left(f_c(t-\tau)+\frac{S}{2}(t-\tau)^2\right)+\varphi_0\right) \tag{6.1}$$

where H is the (attenuated) magnitude of the received signal after reflection and scattering from the target which is mainly dependent on Radar Cross Section (RCS) of the target, receiver antenna gain and two-way travel distance between the transmitter and receiver and τ is as defined in Eq. (2.8).

The phase of the received signal which can be indeed simulated by Eq. (6.1) by inserting values of f_c, S and τ; however, a more pragmatic approach is to study and simulate Eq. (2.10), Eq. (2.10) and Eq. (2.12) which signify the IF I/Q output in complex number format. Figure 6.2 shows the simulated phase of time domain complex baseband IF I/Q signal. This depiction is obtained by joint simulation of Eq 2.10, Eq 2.11 and Eq 2.12 by using the parameters: S = 95.015 MHz/µs, R_0 = 0.54 m, T_s = 0.18µs, f_c = 77 GHz, v = 220 m/s, n = 1 and T_c = 11.63 µs. F and H in Eq. (2.10), Eq. (2.10) and Eq. (2.12) are the magnitudes of the transmitted and received signals respectively. It is well known that the square of the magnitude of magnetic or electric field of an electromagnetic (EM) wave is proportional to its intensity or power [38] , [37]. Therefore, F and H in Eq. (2.10), Eq. (2.10) and Eq. (2.12) can be appropriately estimated by the transmitted and received power with supposing the constant of proportionality as one. In this regard, the transmitted power of 0.017 W is assumed which can be said typical for a COTS mmwave radar platform. Eq. (4.7) is used for the estimation of received power by using the parameters which can be termed typical or practical for COTS mmwave radars; the selected parameters are: P_t = 0.017 W, G_t = 5, G_r = 5, λ = 0.0039 m and R = 0.54 m. A value of -37 dB is used for σ which in fact represents a 5.5 mm airgun pellet.

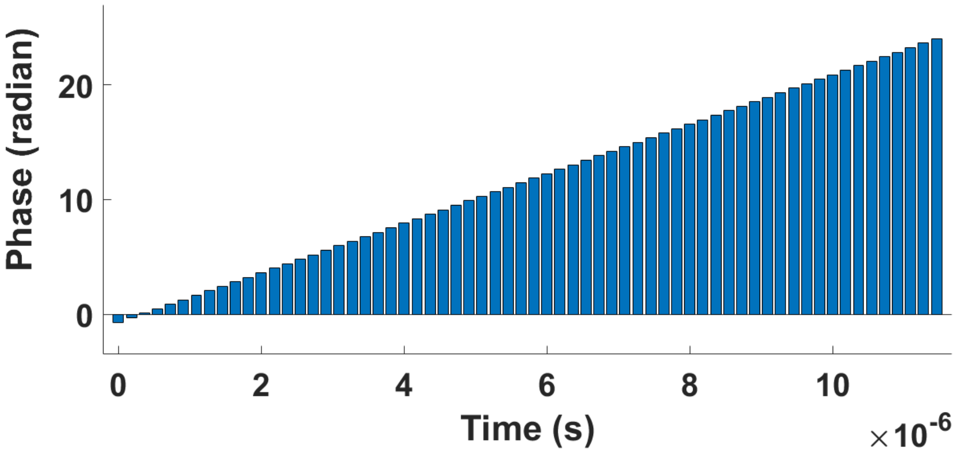

Figure 6.2 Phase of time domain IF I/Q complex baseband signal (simulation data)

Two important points warrant attention from Figure 6.2. One, the received signal also retains the linear phase-time relationship like the transmitted signal albeit with changed phase angle values. The reflection/scattering from the target and the RTOF (τ) do not alter the linear phase-time relationship in the received signal, however, the phase angle levels are changed. A small but important detail here is that the phase values of Figure 6.1 were directly obtained from the time integral in Eq. (2.3). However, the phase values of Figure 6.2 are obtained by using the arctangent function on the complex numbers denoting the time domain IF I/Q baseband signal samples. These values have been further unwrapped to obtain the final phase values of Figure 6.2. The second point is that although a target range of 0.54 m has been entered in the simulation for Figure 6.2, however, the target location cannot be discerned from the phase picture of the time domain IF I/Q mixer output. This is the point where the frequency domain picture and Fast Fourier Transform (FFT) come in handy.

The standard practice in the radar engineering is to obtain a frequency domain picture of the time domain data pertaining to beat frequency. This can be achieved by performing one dimensional (1D) FFT operation. The next step is to obtain the magnitude profile of 1D FFT data. Figure 6.3 shows the magnitude profile (also called the range profile) of single-sided FFT data of time domain data pertaining to Figure 6.2 which is the output of FMCW IF I/Q mixer. The y-axis shows the Power Spectral Density (PSD) in dB where PSD is obtained by using the well-known relation

$$\mathrm{PSD}_{fdi} = {}^{\mathrm{abs}(\mathrm{FFT_i})^2}/_{\mathrm{NumADC}} \tag{6.2}$$

where the subscript fd signifies frequency domain, i is the sample index, FFT is the complex number obtained as result of 1D FFT and `abs()` is the operator signifying the magnitude of the complex number.

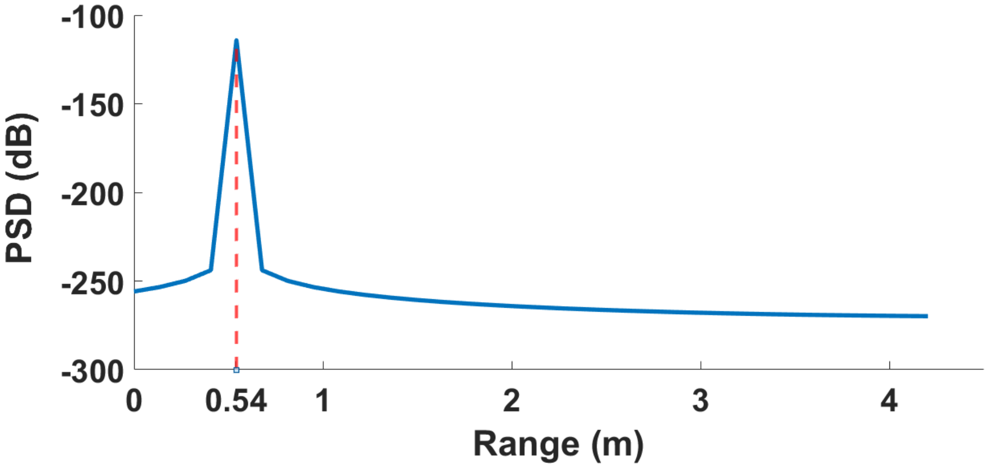

Figure 6.3 Magnitude profile of FFT of IF I/Q signal (simulation data)

The target location is clearly identifiable at the range of 0.54 m. Another small detail to note here is that the individual magnitudes, F and H, in Eq. (2.10), Eq. (2.10) and Eq. (2.12) will alter the peak level in Figure 6.3, however, the overall picture and contour of the curve for this single target scenario will remain constant. This implies that the magnitudes, F and H, do alter the peak levels but they do not alter the phase relationships. It is pertinent to mention that no windowing, no zero-padding and no truncation is used in the FFT processing to obtain Figure 6.3. Furthermore, the time domain data comprised complex numbers therefore complex FFT was executed and the negative frequencies of the complex FFT result were discarded as they would be meaningless in physical sense.

Figure 6.3 is derived from the well-known concept that the frequency domain analysis gives a breakdown of the frequencies constituting a certain time domain signal and the frequency with the biggest magnitude is deemed to be the dominant frequency in the signal. This frequency is in fact the beat frequency given by Eq. (2.12) which is later translated into the range to get the range profile. The physical basis of this phenomenon is the conversion of the time delay between the transmitted and the received signals into the target range.

It will be intuitive now to present a short discourse about the phase-time or phase-range relationship of the 1D FFT data. The phase of the transmitted wave either changes or does not change upon reflection / refraction / scattering from a target or boundary of the medium. This depends upon the nature of wave, type of medium, type of medium boundary and many other factors; the discussion on this aspect of phase change of the received wave (if any) is beyond the scope of this thesis. Let us focus on the time domain data and frequency domain data pertaining to the IF I/Q signal. The magnitude profile of the 1D FFT has already been shown in Figure 6.3. Figure 6.4 shows the phase profile (unwrapped phase of complex numbers) of the single sided 1D FFT data plotted as a function of the target range. Although we have learnt the target location (@ 0.54 m) form the standard practice of obtaining the range profile with 1D FFT operation (Figure 6.3), however, we can observe from the Figure 6.4 that there is a sharp phase transition at the point of target location (0.54 m) in the range profile.

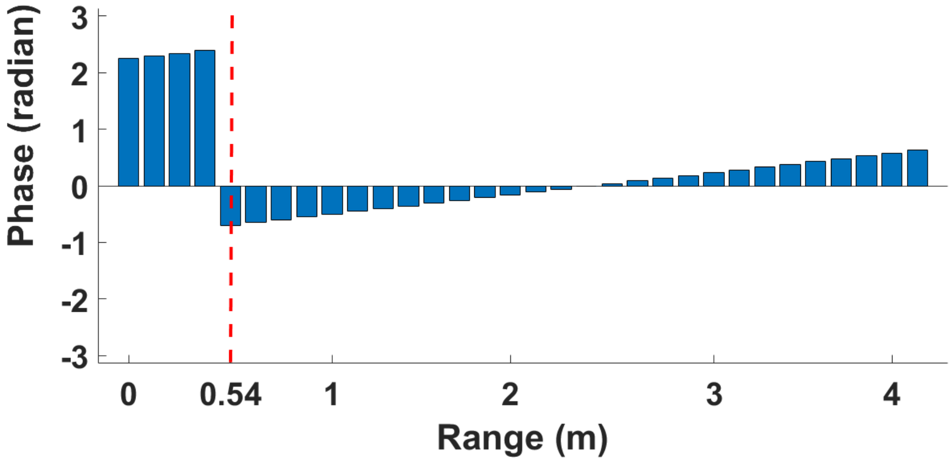

Figure 6.4 Phase vs range plot of FFT of IF I/Q signal (target @ 0.54 m) (simulation data)

Figure 6.5 and Figure 6.6 are further plotted to show the phase profile vs range for the 1D FFT data of IF I/Q simulated data by keeping all other parameters same except that the target range is changed to 1 m and 2 m respectively.

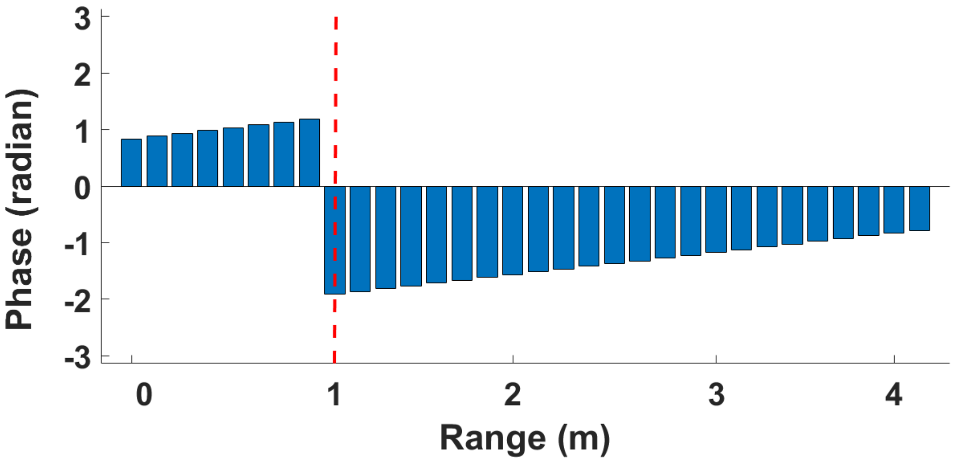

Figure 6.5 Phase vs range plot of FFT of IF I/Q signal (target @ 1 m) (simulation data)

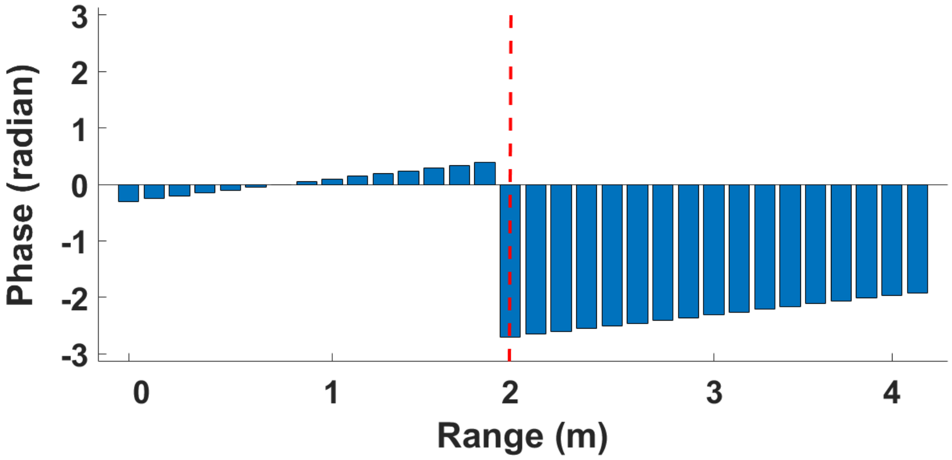

Figure 6.6 Phase vs range plot of FFT of IF I/Q signal (target @ 2 m) (simulation data)

A joint look at Figure 6.4, Figure 6.5 and Figure 6.6 brings forth some important observations. One, while comparing these three figures with Figure 6.2 which shows the time domain IF I/Q data, we can see that the phase profile of time domain data does not enable target localization, however, the phase profile of 1D FFT data enables the target localization by a sharp and abrupt transition at the point of target location in range profile. The total amount of this phase reversal at the point of target location is almost π radians. Two, as mentioned earlier, the initial phase, φ_0, for the transmitted signal is assumed to be zero for the sake of simplicity. However, the initial phase of IF I/Q signal after 1D FFT is not zero in Figure 6.4, Figure 6.5 and Figure 6.6. This is because the initial phase in the received signal varies due to two-way optical length to a stationary target and for a moving target, the stationary phase further includes a component corresponding to the Doppler frequency [27]. Three, the target location bifurcates the otherwise continuous phase slope, however, the slopes of individual piecewise continuous segments of phase-time curve remain same and constant for different target ranges in the figs. Figure 6.4, Figure 6.5 and Figure 6.6. A last point to note from comparison of Figure 6.2 with figs. Figure 6.4, Figure 6.5 and Figure 6.6 is that the phase values in Figure 6.2 are not limited to π radians however the phase values in figs. Figure 6.4, Figure 6.5 and Figure 6.6 are limited to π radians. This is in spite of the fact that phase unwrapping is used in both scenarios for unwrapping the phase obtained by using arctangent operation on complex numbers.

6.1.2 Experimental Study of Phase

It has been seen earlier in the Figure 6.2 of simulation study that the phase profile of time domain IF signal does not give information about target location. It is interesting to briefly observe Figure 6.7 showing the phase profile of IF pertaining to chirp 5284 from the set 22 of experimental data (TABLE III of Annexure A). The particular chirp has been selected as a demonstration example which has an appropriate and observable return echo magnitude in an otherwise challenging scenario of observing a small RCS target traversing radar FoV at a relatively high speed.

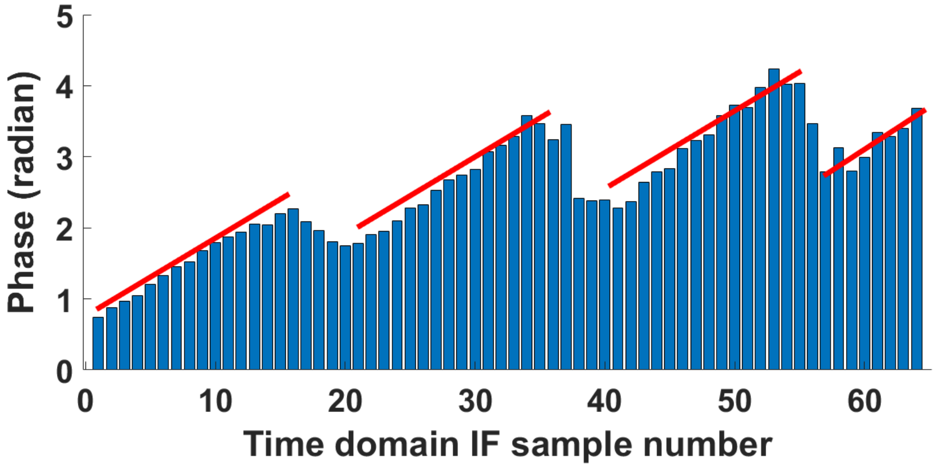

Figure 6.7 Phase of time domain IF signal (field data)

An initial look at Figure 6.7 may give the impression that peaks in phase profile probably indicate targets' positions. Now consider the red approximate trend lines in Figure 6.7 which have same slope but they are offset from each other. A further closer look now at Figure 6.7 with the help of red lines indicates that phase-sample number relationship which is in fact the phase-time relationship, is, in fact linear, however, the discontinuities and offsets are introduced due to phase unwrapping algorithm and due to the various imperfections present in real life situations. Comparison of Figure 6.2 of simulation data and Figure 6.7 of experimental data, shows the same facts that the phase-time relationship of received time domain IF signal remains linear after reflection form the target and that the target location cannot be discerned from this phase-time relationship. This again brings us to the frequency domain analysis; this time we will use the experimental data instead of simulation data. The single-sided FFT of the IF data pertaining to the chirp 5284 of set 22 of the experimental data (TABLE III of Annexure A) is obtained and shown in Figure 6.8 which is the range profile of the data used for Figure 6.7.

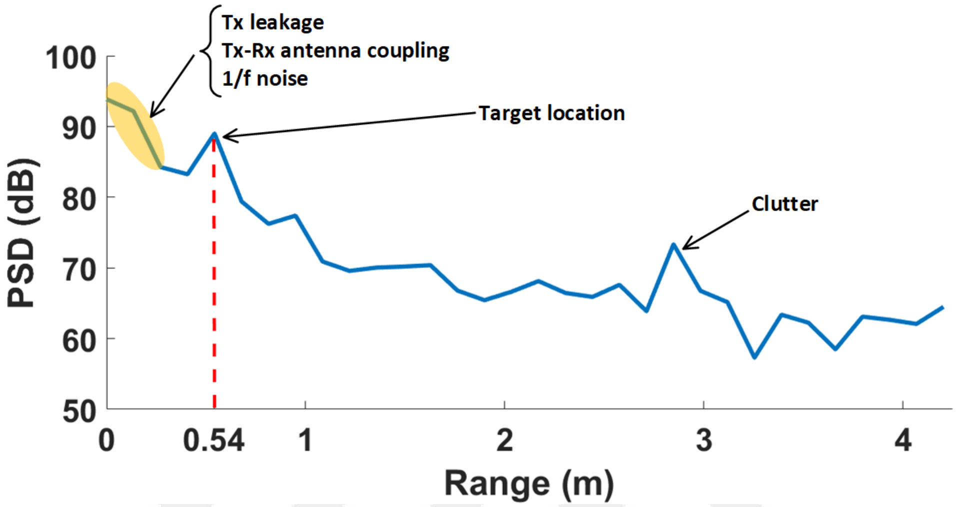

Figure 6.8 FFT range profile (field data)

We have the a priori knowledge from the experimental scenario and study in Chapter 5 that the peak at approx. 2.8 m range is in fact due to stationary clutter / unwanted stationary target in radar FoV. The magnitude peak at 0.54 m shows the target which is the 5.5 mm airgun pellet traversing the radar FoV. A small reminder here is that Figure 6.8 is the momentary snapshot of a target in motion therefore the target appears stationary at 0.54 m range. To have the information about the motion dynamics of the target, we need to have the Doppler profile from two-dimension (2D) FFT which has been discussed in Chapter 5.

6.1.3 Some Aspects Peculiar to Experimental / Field Study

A close comparison of Figure 6.3 and Figure 6.8 shows that the range profile is almost same for the single point target used in simulation study and for the actual point target in the form of an airgun pellet. Apart from that, there are two dissimilarities among Figure 6.3 and Figure 6.8. One, the presence of the clutter echo as discussed briefly earlier. Two, the strong return echoes at zero range and near zero ranges as highlighted in Figure 6.8. This is a small but important detail which is usually missed in the simulation studies where it is usually not effectively modelled. The high return echo magnitude portion in the range profile at zero range and near zero ranges in field data is caused by the following factors:

1) Tx SIGNAL LEAKAGE

Refer Figure 2.1 depicting the FMCW I/Q architecture where we can see that part of FMCW waveform generator (also called Local Oscillator (LO)) is fed to the mixer. Theoretically, it is a straightforward mixing operation which gives a sum and a difference frequency where the sum frequency is filtered out by the low pass filter and difference frequency is retained. However, in real life scenario, there is less than ideal isolation between the two signals being fed to the mixer input ports and this causes several kinds of leakages between the LO and RF signals in the IF and RF signal domains [90].

2) Tx-Rx ANTENNA COUPLING

A separate phenomenon with same outcome as Tx the signal leakage, is the coupling between Tx and Rx antennas. This phenomenon occurs in FMCW systems either with one antenna for both the transmission and reception, or with separate transmitting and receiving antennas. However, the extent of problem worsens in case of single antenna FMCW radar.

3) $1/f$ NOISE

The above-mentioned factors pertain specifically to FMCW radars. However, there is another factor that is specific to the frequency domain analysis of many diverse types of time domain naturally occurring data. This is called the $1/f$ noise and it is observed to be present in near zero frequency region (very low frequency region) in most naturally occurring data [64]. $1/f$ noise is described to be present in data as diverse as electronic noise in transistors, traffic density on freeways, music, stock markets, memory, reaction times etc. Sufficient explanation of the origin of $1/f$ and its wide occurrence has not been possible yet, however, it remains a significant fact.

4) INSEPARABILITY OF THE FACTORS CAUSING CLOSE RANGE RETURN ECHOES

The important points to note here are that the individual manifestations of these three factors cannot be segregated from each other, and, it is very difficult, if not impossible, to identify and segregate the target echoes due to these factors. The only way to overcome these factors at near zero ranges is to have enough return echo magnitude so that the target rises above the elevated noise floor and the echoes at near zero ranges. However, it may or may not be possible to achieve this in the wake of limitations imposed by operational scenario vis-a-vis the hardware system constraints. The other point to be mindful about is that the simulation scenario does not always depict the challenges encountered in field data therefore a realization and appreciation of the practical aspects of a technology application is necessary.

5) ORIGINS OF ZERO-DOPPLER COLUMN IN 2D FFT RANGE-DOPPLER PROFILE

Although this chapter is more focused on 1D FFT range profile however a short mention of 2D FFT is warranted here. 2D FFT operation on the IF time domain data yields a Range-Doppler (RD-map). Figure 6.9 shows two RD-maps from set 22 (subframe 2 of frame 164 and 165) of the experimental data [TABLE III of Annexure A] which may be referred for further details. The first RD-map does not contain a target echo and the 2nd RD-map shows a moving target. We can see high energy cells in the zero-Doppler column which is shown at index 1.

The energy to the zero-Doppler column is contributed by all those factors which have zero Doppler speed and there are two types of such contributories. One, all the factors mentioned vide para 6.1.3(1) Tx Signal Leakage, para 6.1.3(2) Tx-Rx Antenna Coupling and para 6.1.3(3) $1/f$ noise. All these factors have a zero-Range nature but their effect may also extend to ranges a little more than zero range (refer Figure 6.8). However, they essentially have zero-Doppler nature because of their stationary nature and therefore, in a RD-map, those factors will be confined to zero-Doppler column. Second, all stationary targets will also fall in zero-Doppler column with zero Doppler speed but with the corresponding non-zero range.

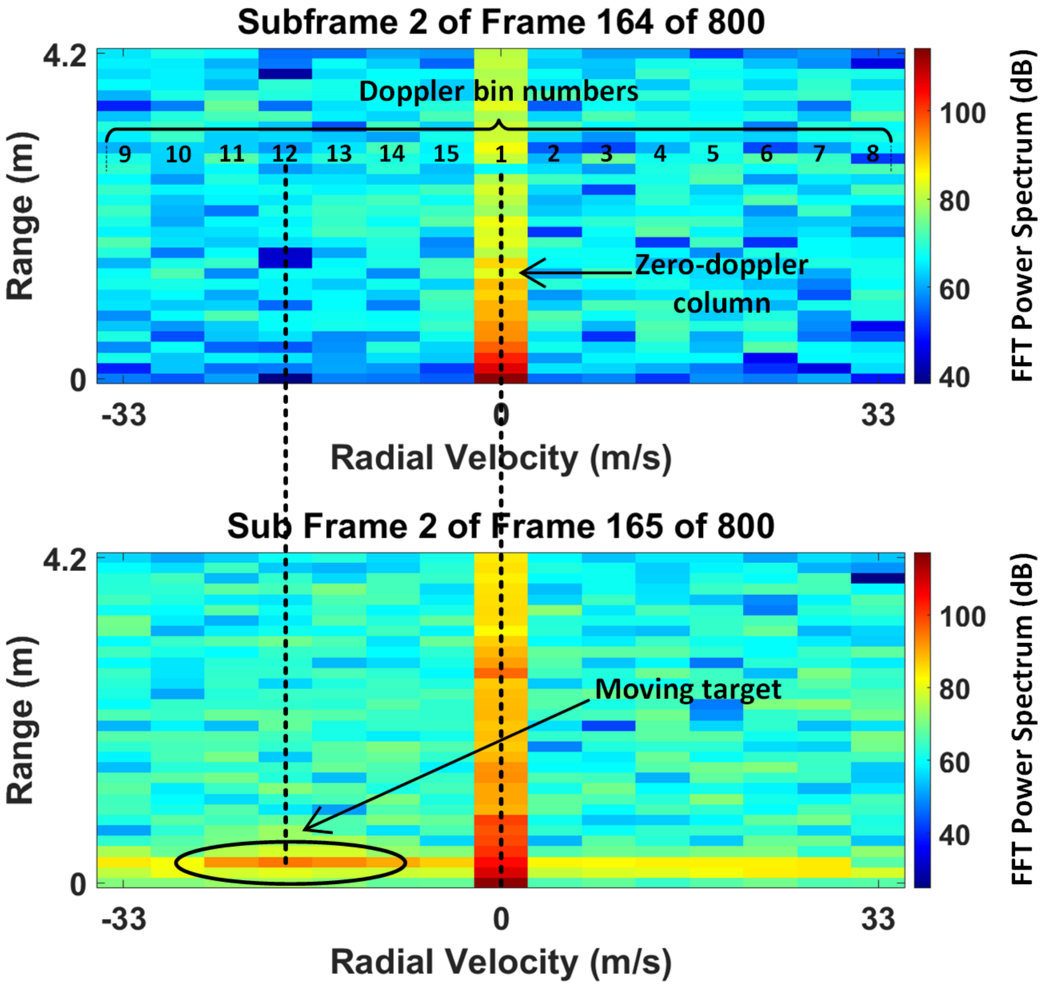

Figure 6.9 Examples of RD-maps (with and without target)

6.1.4 Some Cautions about Frequency Domain Analysis

There are certain techniques to improve the operation and results of the frequency domain analysis. Some of the commonly used operations are windowing, zero-padding and truncation. Extensive literature exists on these topics. In the particular connection of the phase-time or phase-sample number relation of the FMCW signals (Tx signal, Rx signal or IF signal), some points need to be careful about. Windowing process is carried out some times to extract a target peak in range profile or to make the peak broader or sharper. No windowing process has been used in this tutorial study because the target peak was appropriately discernable and it was intended to keep the signal processing as unaided as possible. However, if windowing needs to be performed, then it must be ensured to make the windowing operation symmetrical with respect to its central point. This is required to retain the linear phase [27]. Furthermore, zero-padding is used sometimes to increase the resolution of the FFT operation. Again, zero-padding was not used in this study. However, even if zero-padding needs to be executed, attention needs to be given to the fact that zero-padding distorts the linear phase relationship. The simulation example and the field data, both use 64 ADC samples; 256-point FFT operation is performed next on the 64-point data to emulate zero-padding.

Figure 6.10 shows the phase curve reconstructed by first performing 256-point FFT on the 64-point IF data obtained from the simulation of Eq. (2.12) and then performing the 256-point Inverses FFT (IFFT) on the FFT data. We can see in Figure 6.10 that only the initial 64-point part of the 256-point reconstructed sequence corresponds to the original simulated phase graph of Figure 6.2. The remaining part corresponds to the zero-padded portion and it does not contain any meaningful information.

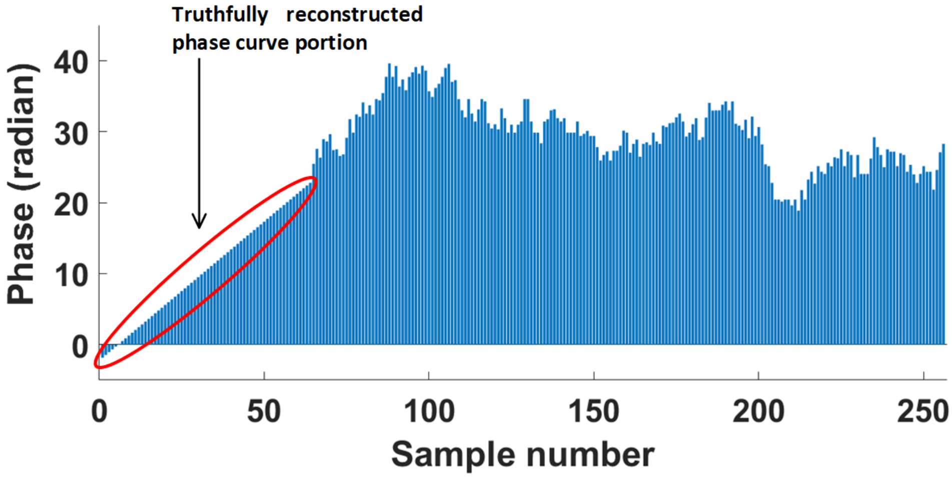

Figure 6.10 Phase curve reconstruction by IFFT of 256-point FFT of 64-point simulated IF data

Next, the 64-point time domain IF data for chirp 5284 from the set 22 of experimental data (TABLE III of Annexure A) is subjected to 256-point FFT and then 256-point IFFT is executed; the phase profile of the reconstructed data is shown as Figure 6.11.

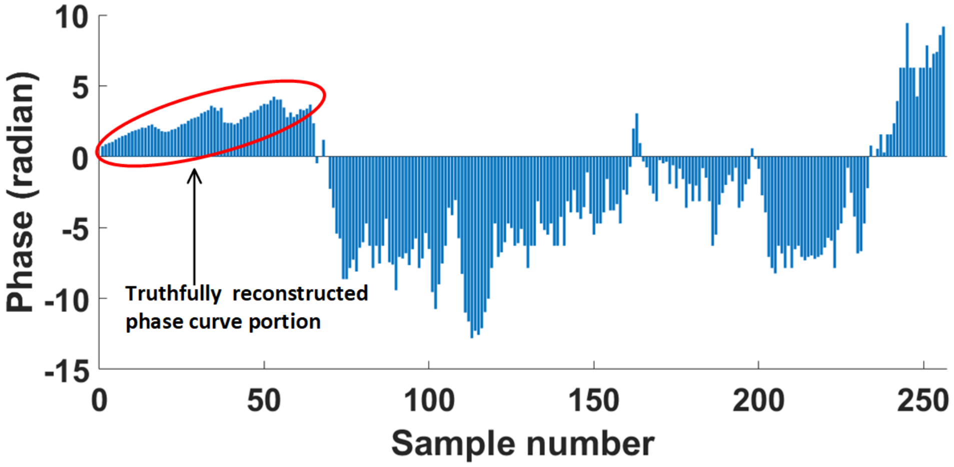

Figure 6.11 Phase curve reconstruction by IFFT of 256-point FFT of 64-point field IF data

When compared with Figure 6.7, we observe from Figure 6.11 that only the portion corresponding to the original 64-point ADC data can be reconstructed and the zero-padding distorts the phase relation in the zero-padded portion of the data sequence. The simulation study of Figure 6.10 and the field experimental data of Figure 6.11 depict the same observation that although the use of zero-padding might be appealing for improving the FFT resolution, however, the use of zero-padding is not useful for a study that is based on the phase values of the zero-padded data. Interested readers may like to further research this area.

Truncation is another allied technique where the time domain sample sequence is sometimes truncated during FFT operation. Its implication in connection with this phase study is straightforward in the sense that truncation here is tantamount to losing data which will imply shortening of range profile in 1D FFT.

6.1.5 The Case of FFT Processing Gain

The 2nd pass of 2D FFT operation is performed on the data obtained after execution of 1st FFT operation on the time domain IF data. The RD-map obtained as a result of 2D FFT operation is usually obtained by noncoherent integration during 2nd FFT pass which is actually adding the FFT magnitude from given chirps across each range bin. This facilitates a FFT processing gain which is in fact noncoherent integration gain. From an ideal perspective, FFT processing is ought to produce coherent gain of value M for a M-point measurement. However, due to practical aspects like Doppler cell straddling, filter shape losses etc., the value of FFT processing gain falls below the ideal value of coherent integration gain. In addition, more often, the 2nd FFT operation is itself performed as noncoherent integration process across each individual range bin. Due to these facts, the FFT processing gain is generally said to have a value between $\sqrt{M}$ (lowest value corresponding to noncoherent integration gain) and M (highest value corresponding to coherent integration) [9], [82], [38].

Basic and advanced details of 2D FFT operation to obtain RD-map from time domain data are widely available. Therefore, only a brief practical demonstration of FFT processing gain is shared which is derived from a field study. Figure 6.12 shows the range profiles for the 15 chirps in two different CPIs from set 04 (subframe 2 of frame 138 and 151) of the experimental data (TABLE III of Annexure A). It was known a posteriori (based on 2D FFT post processing) that the apparent peaks at approx. 1.2 m and 3 m belong to stationary clutter and that target was detected in subframe (SF) 2 of frame 138 at 1.63 m range as it crossed radar FoV and that the moving target was not detected in SF 2 of frame 151 as it had exited the radar FoV by then. Now with this a priori knowledge, we observe Figure 6.12 and it can be clearly seen that there is no noticeable indication of target presence in SF 2 of frame 138 in the range profile. In fact, there is hardly any difference in the range profiles of the CPI with the target (frame 138) and CPI without the target (frame 151) in Figure 6.12.

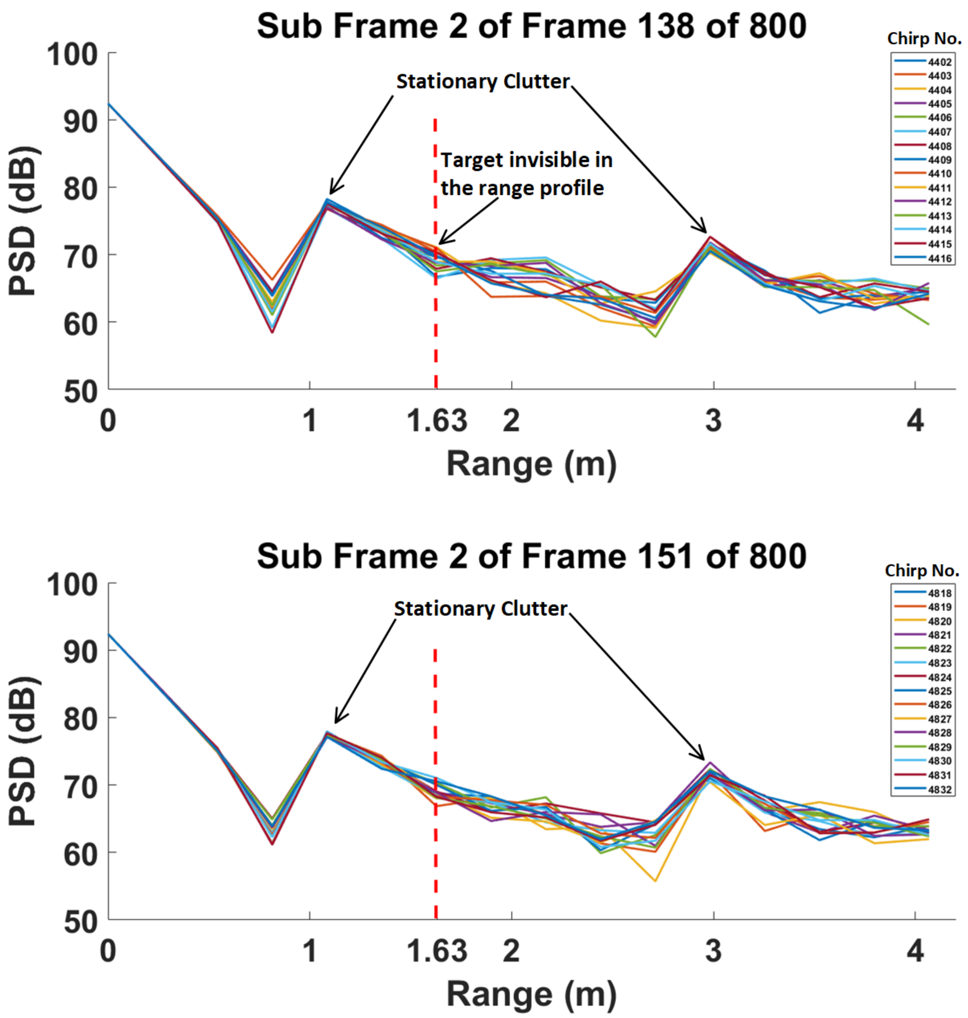

Figure 6.12 Range profile for two different CPIs (with and without a moving target)

Subsequently, Figure 6.13 depicts the RD-maps for SF 2 of frame 138 and 151, respectively. Although the target is significantly feeble, yet it is observable in RD-map of SF 2 of frame 138 at a range of 1.63 m. No target can be seen in RD-map of SF 2 of frame 151. Comparison of range profile from Figure 6.12 and RD-map from Figure 6.13, for SF 2 of frame 138, demonstrates the contribution of FFT processing gain with the help of experimental field data. It furnishes an example of FFT processing gain making a moving target visible in 2D FFT RD-map which was earlier invisible in 1D FFT range profile.

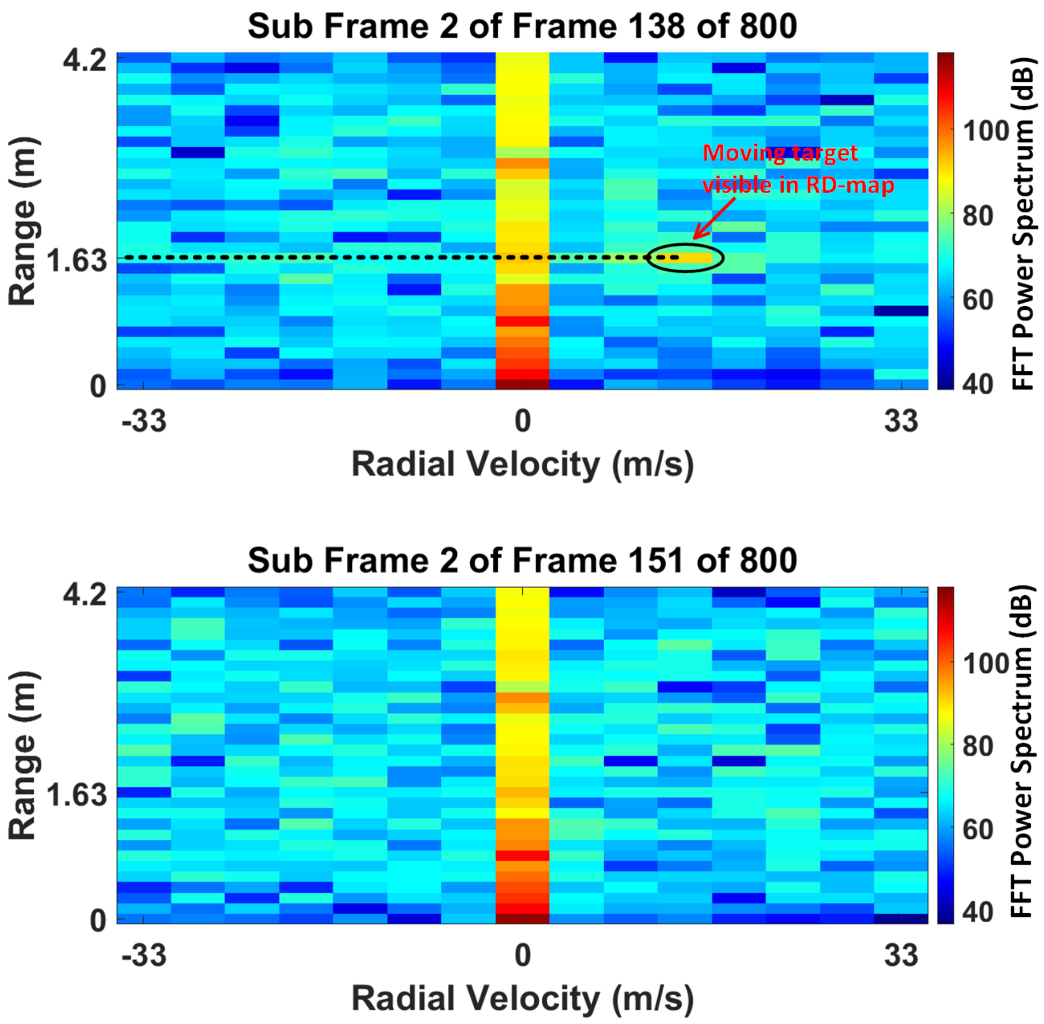

Figure 6.13 RD-maps from two different CPIs (with and without a moving target)

6.2 Some Additional Applied Aspects

6.2.1 Comparison of Range Resolution from Physics and FFT Aspects

The range resolution is defined as the minimum distance between the targets for enabling the radar to distinguish them as distinct targets. Form radar engineering perspective, range resolution is given as [23] :

$$\Delta R = \frac{c}{2B} \tag{6.3}$$

For the demonstration example (TABLE II), for a bandwidth of 1.1056 GHz, ΔR has a value of 0.1356 m from Eq. (6.3). Next suppose the time domain I/Q signal is sampled with a sampling frequency F_s. Then, the frequency bin of FFT is given as Eq. (4.5). The center frequency for the n^{th} FFT bin is then given by

$$f_n = \frac{\Delta f}{2} n \tag{6.4}$$

The FFT frequency peak will shift to next or previous bin if the FFT frequency exceeds or decreases from the value of f_n by $\pm 0.5\Delta f$ [64]. The unambiguously measurable maximum range of a FMCW radar is given as [23]:

$$R = \frac{c f_{IF} T_c}{2B} \tag{6.5}$$

where f_{IF} is the intermediate frequency obtained after mixer operation shown in Figure 2.1. In fact, f_{IF} could be changed for any other relevant value of frequency parameter and corresponding range could be obtained. For example, we can replace f_{IF} in Eq. (6.5) by Δf from Eq. (4.5) and thus we can find the length of one range bin corresponding to one FFT frequency bin. For a value of N=64 (64 ADC samples/chirp) and ADC sampling frequency (F_s) of 5.5Msps, we obtain Δf=85.9 kHz which gives a corresponding range 0.1355 m from Eq. (6.5) by using T_c= 11.63 µs. This value 0.1355 m range bin closely matches the range bin value of 0.1356 m from Eq. (6.3) which shows the agreement in range resolution derived from physics aspect (Eq. (6.3) and from FFT aspects (Eq. (4.5), Eq. (6.4) and Eq. (6.5)). However, two subtle points need attention here. One, the FFT range resolution can be improved (finer resolution) by increasing n in Eq. (4.5). One evident way to achieve this is to increase the number of ADC samples. The other way to increase FFT resolution is to use zero-padding, however, as shown earlier, this will distort the phase relationship therefore, the coherent processing will not remain relevant. The zero-padding can still be used for benefit of range resolution improvement with non-coherent processing. The second small detail to consider is to be careful about what constitutes the chirp time (T_c). In ideal theoretical conditions, the chirp time will be equal to total ADC sampling time for n samples. However, in real-life scenarios, there is some extra idle time at the start and the end of the chirp which makes total chirp time longer [23]. Nonetheless, the range-related calculations should be based on actual ADC total sampling time only otherwise the results will be wrong. At the same time, be careful that in contrast to range related calculations, Eq. (4.4) for velocity measurement uses complete chirp time, including the idle times within the chirp.

6.2.2 The Connection of Range Resolution and Velocity Ambiguity: An Optimization Problem

Refer Eq. (4.4) and Eq. (4.6) which involve instantaneous phase measurements from two distinct chirps could be either from same range bins or different range bins. Let us first suppose the less probable case that the two phase measurements for use in Eq. (4.4) are from two distinct, rather, consecutive range bins. For the demonstrative case, λ= 0.0039 m for f_c= 77 GHz. A straightforward approach for measuring a high velocity could be to tune the radar parameters in a way that the range resolution is made equal to wavelength (i.e. $\Delta R = \lambda$). In such case, the maximum measurable velocity can be estimated by the relation $\lambda = v_r T_c$ for a given T_c and fixed λ. However, it could be prohibitive in terms of hardware limitations to obtain such fine range resolution. For the 77 GHz frequency under consideration, a bandwidth of 38.4 GHz is required for achieving range resolution of 0.0039 m and this value of bandwidth is not available, at least in COTS automotive radar platforms. As bandwidth is inseparably tied with frequency slope, so it is not feasible from technology availability perspective. In fact, the simple approach just mentioned is the measurement of velocity from two distinct range measurements and phase measurement comes in an indirect connotation with the limitation that the velocity is high enough that two consecutive measurements do not fall in the same range bin. The imposition of consecutive range bins is a worst case scenario described just for explanation purpose, partially to emphasize principal value of phase in (0,2π) open interval. In fact, phase measurement rather becomes redundant in this case as the velocity can also be conveniently measured by using two distinct range measurements and the chirp time by using the distance formula.

The widely used case of velocity measurement through phase angle (Eq. (4.4)) involves presence of (at least) two measurements in the same range bin. Here, consider the previous example of 1D FFT operation (without zero-padding) for obtaining range profile with range resolution ΔR value of 0.1356 m. In this case, the one range bin will contain ($\Delta R/\lambda = 0.1356/0.0039 \cong$) 34 wavelengths. In this case, for velocity measurement to be unambiguous, the phase difference between measurements from two chirps should be within the limit $|\varphi_v| < \pi$. This obviously explains why phase measurement provides very precise velocity measurement and even range measurement, provided that the displacement is relatively less, preferably in order of a few tens of λ, given that the velocity is not high enough to cause ambiguous measurements. The quantitative measure of the maximum measurable velocity can be thus obtained from Eq. (4.6) while considering T_c as per relevant hardware limitations.

CHAPTER 7

CONCLUSION

This thesis research has had a more applied focus. The goal was to explore the use of a COTS FMCW mmwave automotive radar hardware platform for proximity sensing at speeds significantly higher than the ones encountered by automotive radars. The theoretical aspects were explored and developed to overcome the limitations and constraints while attempting to extend operational limit for the velocity measurement by a COTS FMCW automotive radar. This was followed by the experimental demonstration of the theoretical techniques in the field experiment.

7.1 Contributions of The Research

From the onset of the study, it was envisaged that a 9 mm pistol would be used to generate approximately 300 m/s speed. This led to a study for the RCS measurement of 9 mm pistol bullet with 77 GHz COTS FMCW automotive radar. To the knowledge of the authors, this frequency band has not been used and reported so far for a similar RCS study.

Further use of 9 mm bullet was abandoned due to safety, logistics and availability reasons and it was decided to use 5.5 mm pellet with an airgun to generate a high-speed target scenario.

Phase measurement is the basic idea for speed measurement, particularly in FMCW radars. A pragmatic approach was developed based on the basic but applied relations between magnitude and phase of complex numbers. The technique has certain limitations, especially due to non-linear relation between the received back-scattered power and range of the target form the radar. However, a quasi-linear portion of this relation was assumed. The theoretical model was developed and implemented. The experimental demonstration was sub-optimal due to various peculiar scenarios. However, the speed of the small RCS high-speed target (5.5 mm airgun pellet) was demonstrated to be measured with optimal accuracy. The proposed method based on interpolation of magnitude to resolve phase ambiguity is novel but nascent. It has certain limitations but to the knowledge of the author, it has been not suggested earlier. Researchers in other scientific and physical sciences fields can probably explore this idea for application in other fields, especially where there is a linear and directly proportional relation between the two physical quantities being processed.

CRT is a popular technique for resolving ambiguity in various fields. However, its use, especially in real-time field experiment has not been demonstrated so far in 77 GHz frequency range for a similar small RCS target with similar speed. The detailed application example is also deemed to serve as a detailed applied tutorial or case study on resolving velocity ambiguity with CRT.

Certain details are presented for the frequency domain analysis especially pertaining to the phase study of the radar transmitted and received signals. To the knowledge of the authors, a similar compilation of these intricate and sometimes overlooked aspects, has not been presented earlier, especially in the context of automotive radar applications for such high-speed small RCS target.

7.2 Future Research

There could be many venues for future research in the connection with this thesis. One is the application of the magnitude interpolation technique for resolving phase ambiguity for measuring various physical quantities. As the experimental data is gathered in complex baseband I/Q format during this research, therefore another aspired possible research direction is to explore the potential of complex baseband especially in the context of interference rejection.

REFERENCES

[1] Z. Peng, L. Ran, and C. Li, "A K-Band Portable FMCW Radar With Beamforming Array for Short-Range Localization and Vital-Doppler Targets Discrimination," *IEEE Transactions on Microwave Theory and Techniques,* vol. 65, no. 9, pp. 3443-3452, 2017.

[2] S. E. Craig, W. Fishbein, and O. E. Rittenbach, "Continuous-Wave Radar with High Range Resolution and Unambiguous Velocity Determination," *IRE Transactions on Military Electronics,* vol. MIL-6, no. 2, pp. 153-161, 1962.

[3] A. Bazzi, C. Karnfelt, A. Peden, T. Chonavel, P. Galaup, and F. Bodereau, "Estimation techniques and simulation platforms for 77 GHz FMCW ACC radars," (in English), *European Physical Journal-Applied Physics,* Article vol. 57, no. 1, Jan 2012.

[4] J. Hasch, E. Topak, R. Schnabel, T. Zwick, R. Weigel, and C. Waldschmidt, "Millimeter-Wave Technology for Automotive Radar Sensors in the 77 GHz Frequency Band," *IEEE Transactions on Microwave Theory and Techniques,* vol. 60, no. 3, pp. 845-860, 2012.

[5] W. Menzel and A. Moebius, "Antenna Concepts for Millimeter-Wave Automotive Radar Sensors," *Proceedings of the IEEE,* vol. 100, no. 7, pp. 2372-2379, 2012.

[6] C. Händel, H. Konttaniemi, and M. Autioniemi, "State-of-the-Art Review on Automotive Radars and Passive Radar Reflectors, Arctic Challenge research project," Lapland University of Applied Sciences, Rovaniemi, FinlandSeries B. Research reports and compilations 6/2018, 2018.

[7] C. Zhang, M. D. Cao, Y. Li, Y. Q. Gong, and Y. M. Huang, "Velocity ambiguity resolution for wideband automotive millimeter wave radar: a carrier frequency multiplexing framework," (in English), *Journal of Electromagnetic Waves and Applications,* Article vol. 34, no. 3, pp. 375-389, Feb 2020.

[8] N. S. Reddy and M. N. S. Swamy, "Resolution of range and doppler ambiguities in medium PRF radars in multiple-target environment," *Signal Processing,* vol. 11, no. 3, pp. 223-236, 1986/10/01/ 1986.

[9] C. Alabaster, *Pulse Doppler Radar, Principles, Technology, Applications*. Raleigh, North Carolina, USA: Scitech Publishing, 2012.

[10] D. Brumbi, "Industrial Level Sensing with Radar," *Frequenz,* vol. 60, pp. 2-6, 02/01 2006.

[11] M. Vogt, T. Neumann, and M. Gerding, "Frequency-diversity technique for reliable radar level measurement of bulk solids in silos," in *2013 European Radar Conference*, 2013, pp. 129-132.

[12] M. v. Wanum, M. Polushkin, and R. v. Dijk, "Analogue baseband processing for single chip radar proximity sensor," in *2020 17th European Radar Conference (EuRAD)*, 2021, pp. 438-441.

[13] M. Mercuri *et al.*, "2-D Localization, Angular Separation and Vital Signs Monitoring Using a SISO FMCW Radar for Smart Long-Term Health Monitoring Environments," *IEEE Internet of Things Journal*, vol. 8, no. 14, pp. 11065-11077, 2021.

[14] A. A. Pramudita and F. Y. Suratman, "Low-Power Radar System for Noncontact Human Respiration Sensor," *IEEE Transactions on Instrumentation and Measurement*, vol. 70, pp. 1-15, 2021.

[15] J. Liu, Y. Li, C. Li, C. Gu, and J. Mao, "Accurate Measurement of Human Vital Signs with Linear FMCW Radars under Proximity Stationary Clutters," *IEEE Transactions on Biomedical Circuits and Systems*, pp. 1-1, 2021.

[16] C. Migliaccio *et al.*, "Millimeter-Wave Radar for Rescue Helicopters," in *2006 9th International Conference on Control, Automation, Robotics and Vision*, 2006, pp. 1-6.

[17] T. Luo, C. E. Wu, and Y. E. Chen, "A 77-GHz CMOS Automotive Radar Transceiver With Anti-Interference Function," *IEEE Transactions on Circuits and Systems I: Regular Papers*, vol. 60, no. 12, pp. 3247-3255, 2013.

[18] J. Park, H. Ryu, K. Ha, J. Kim, and D. Baek, "76–81-GHz CMOS Transmitter With a Phase-Locked-Loop-Based Multichirp Modulator for Automotive Radar," *IEEE Transactions on Microwave Theory and Techniques*, vol. 63, no. 4, pp. 1399-1408, 2015.

[19] H. Haderer, R. Feger, C. Pfeffer, and A. Stelzer, "Millimeter-Wave Phase-Coded CW MIMO Radar Using Zero- and Low-Correlation-Zone Sequence Sets," *IEEE Transactions on Microwave Theory and Techniques*, vol. 64, no. 12, pp. 4312-4323, 2016.

[20] T. Fujibayashi *et al.*, "A 76- to 81-GHz Multi-Channel Radar Transceiver," *IEEE Journal of Solid-State Circuits*, vol. 52, no. 9, pp. 2226-2241, 2017.

[21] M. Alizadeh, "Remote vital signs monitoring using a mm-wave FMCW radar," Master Thesis, Electrical and Computer Engineering, University of Waterloo, Ontario, Canada, 2019.

[22] S. Suleymanov, "Design and Implementation of an FMCW Radar Signal Processing Module for Automotive Applications," Master Thesis, University of Twente, Enschede, The Netherlands, 2016.

[23] Z. Xia, Y. Luomei, C. Zhou, and F. Xu, "Multidimensional Feature Representation and Learning for Robust Hand-Gesture Recognition on Commercial Millimeter-Wave Radar," *IEEE Transactions on Geoscience and Remote Sensing,* vol. 59, no. 6, pp. 4749-4764, 2021.

[24] S. Jeng, W. Chieng, and H. Lu, "Estimating Speed Using a Side-Looking Single-Radar Vehicle Detector," *IEEE Transactions on Intelligent Transportation Systems,* vol. 15, no. 2, pp. 607-614, 2014.

[25] J. J. Lin, Y. P. Li, W. C. Hsu, and T. S. Lee, "Design of an FMCW radar baseband signal processing system for automotive application," (in English), *Springerplus*, Article vol. 5, p. 16, Jan 2016, Art. no. 42.

[26] M. Rameez, "Interference mitigation techniques in FMCW automotive radars," Licentiate, Department of Mathematics and Natural Sciences, Blekinge Institute of Technology, Karlskrona, Sweden, 2020.

[27] B. R. Mahafza, *Radar Systems Analysis and Design Using MATLAB*, 3rd ed. Boca Raton, Florida, USA: CRC Press, Taylor & Francis Group, 2013.

[28] M. MATLAB. Radar Data Cube. Internet: https://www.mathworks.com/help/phased/gs/radar-data-cube.html#bs1f5v6 , [Oct. 18, 2020].

[29] S. Harmer, S. Cole, and N. Bowring, "Radar identification of hostile fire by means of the electromagnetic complex natural resonances of projectiles," *Progress In Electromagnetics Research M*, vol. 24, pp. 167-178, 2012.

[30] T. Pizzillo, "Technical Report ARL-TN-0296 Radar Cross Section Measurement of a 50 Caliber Bullet at Ka-Band," ARL US Army Research Laboratory2007.

[31] C. Kenyon and T. Dogaru, "Technical Report ARL-TR-7468 Numerical Computation of the Radar Cross Section of Rockets and Artillery Rounds," ARL US Army Research Laboratory2015.

[32] K. Chang, M. A. Pollock, M. K. Skrehot, G. D. Arndt, and J. Suddath, "System feasilbility study of a microwave millimeter-wave radar for space debris tracking," *International Journal of Infrared and Millimeter Waves,* vol. 10, no. 1, pp. 1-19, Jan 1989.

[33] F. A. Sadjadi, "A model based technique for recognizing targets by using millimeter wave radar signatures," *International Journal of Infrared and Millimeter Waves,* vol. 10, no. 3, pp. 337-342, Mar 1989.

[34] E. Yigit, S. Demirci, A. Unal, C. Ozdemir, and A. Vertiy, "Millimeter-wave Ground-based Synthetic Aperture Radar Imaging for Foreign Object Debris Detection: Experimental Studies at Short Ranges," *Journal of Infrared Millimeter and Terahertz Waves*, vol. 33, no. 12, pp. 1227-1238, Dec 2012.

[35] *IEEE Std 1502-2007 Recommended Practice for Radar Cross-Section Test Procedures*, null, 2007.

[36] Y. Song, Y. P. Li, S. Pang, S. S. Zhao, and H. Q. Wang, "RCS measurement at terahertz waves for cylinders with different surface roughness," (in English), *Electronics Letters*, Article vol. 54, no. 11, pp. 714-715, May 2018.

[37] M. A. Richards, J. A. Scheer, and W. A. Holm, *Principles of Modern Radar Vol. I: Basic Principles*. Edison, New Jersey, USA: SciTech Publishing, 2010.

[38] M. A. Richards, *Fundamentals of Radar Signal Processing*, 2nd ed. McGraw-Hill Education, 2014.

[39] S. Pang, Y. Zeng, Q. Yang, B. Deng, H. Q. Wang, and Y. L. Qin, "Improvement in SNR by Adaptive Range Gates for RCS Measurements in the THz Region," (in English), *Electronics*, Article vol. 8, no. 7, Jul 2019.

[40] A. Hulsmann. Millimeter-wave radar for hostile fire indication. Internet: https://www.iaf.fraunhofer.de/content/dam/iaf/documents/ausz%C3%BCge-jahresberichte/16_gf1_3_millimeter-wave-radar.pdf , Oct. 01, 2019 [Dec. 19, 2020].

[41] P. Grohs, S. Koppensteiner, and M. Rathmair, "Phase Retrieval: Uniqueness and Stability," (in English), *SIAM Review*, Article vol. 62, no. 2, pp. 301-350, Jun 2020.

[42] N. Lippok, B. E. Bouma, and B. J. Vakoc, "Stable multi-megahertz circular-ranging optical coherence tomography at 1.3 mu m," *Biomedical Optics Express*, vol. 11, no. 1, pp. 174-185, Jan 2020.

[43] H. Y. Fan, L. X. Ren, E. K. Mao, Q. H. Liu, and J. Yang, "A High-Precision Phase-Derived Velocity Measurement Method for High-Speed Targets Based on Wideband Direct Sampling LFM Radar," *IEEE Trans. Geosci. Remote Sens.*, vol. 57, no. 12, pp. 10147-10163, Dec 2019.

[44] Q. C. Chen, Y. Liu, B. Tan, K. Woodbridge, and K. Chetty, "Respiration and Activity Detection Based on Passive Radio Sensing in Home Environments," *IEEE Access*, vol. 8, pp. 12426-12437, 2020.

[45] X. H. Xu and D. T. Sandwell, "Toward Absolute Phase Change Recovery With InSAR: Correcting for Earth Tides and Phase Unwrapping Ambiguities," *IEEE Trans. Geosci. Remote Sens.*, vol. 58, no. 1, pp. 726-733, Jan 2020.

[46] S. Sirianunpiboon, P. Q. C. Ly, and S. D. Elton, "A Practical Diophantine Approximation for Sparse Linear Array Direction Finding," *IEEE Trans. Aerosp. Electron. Syst.,* pp. 1-1, 2020.

[47] W. Horng, "An Efficient DOA Algorithm for Phase Interferometers," *IEEE Trans. Aerosp. Electron. Syst.,* vol. 56, no. 3, pp. 1819-1828, 2020.

[48] S. Scherr, S. Ayhan, B. Fischbach, A. Bhutani, M. Pauli, and T. Zwick, "An Efficient Frequency and Phase Estimation Algorithm With CRB Performance for FMCW Radar Applications," *IEEE Trans. Instrum. Meas.,* vol. 64, no. 7, pp. 1868-1875, 2015.

[49] L. Piotrowsky, T. Jaeschke, S. Kueppers, J. Siska, and N. Pohl, "Enabling High Accuracy Distance Measurements With FMCW Radar Sensors," *IEEE Trans. Microw. Theory Techn.,* vol. 67, no. 12, pp. 5360-5371, 2019.

[50] M. Scherhäufl, F. Hammer, M. Pichler-Scheder, C. Kastl, and A. Stelzer, "Radar Distance Measurement With Viterbi Algorithm to Resolve Phase Ambiguity," *IEEE Trans. Microw Theory Techn.,* vol. 68, no. 9, pp. 3784-3793, 2020.

[51] H. J. Huh and D. E. Pelinovsky, "Nonexistence of self-similar blowup for the nonlinear Dirac equations in (1+1) dimensions," *Applied Mathematics Letters,* vol. 92, pp. 176-183, Jun 2019.

[52] A. Garcia-Mondejar, N. Gourmelen, M. J. Escorihuela, M. Roca, A. Shepherd, and S. Plummer, "Multisurface Retracker for Swath Processing of Interferometric Radar Altimetry," *IEEE Geosci. Remote Sens. Lett.,* vol. 16, no. 12, pp. 1839-1843, Dec 2019.

[53] A. Acharya and N. Kawade, "A Fabry-Perot Interferometer based Fiber Optic Dynamic Displacement Sensor with an Analog In-phase/Quadrature Generator," *IEEE Sensors J.,* pp. 1-1, 2020.

[54] M. C. Casaban, J. C. Cortes, J. V. Romero, and M. D. Rosello, "Probabilistic solution of random homogeneous linear second-order difference equations," *Applied Mathematics Letters,* vol. 34, pp. 27-32, Aug 2014.

[55] P. Berestesky and E. H. Attia, "Sidelobe Leakage Reduction in Random Phase Diversity Radar Using Coherent CLEAN," *IEEE Trans. on Aerosp. Electron. Syst.,* vol. 55, no. 5, pp. 2426-2435, 2019.

[56] X. Y. Xiong, Z. M. Deng, W. Qi, and Y. J. Dou, "High-precision angle estimation based on phase ambiguity resolution for high resolution radars," *Science China-Information Sciences,* vol. 62, no. 4, Apr 2019, Art. no. 040307.

[57] R. Tan. Complex Sinusoids Interactive Demo, MATLAB Central File Exchange. Internet:

https://www.mathworks.com/matlabcentral/fileexchange/53410-complex-sinusoids-interactive-demo, Aug. 28, 2020 [Oct. 23, 2020].

[58] Q. H. Wu, F. G. Sun, P. Lan, G. R. Ding, and X. F. Zhang, "Two-Dimensional Direction-of-Arrival Estimation for Co-Prime Planar Arrays: A Partial Spectral Search Approach," *IEEE Sensors J.*, vol. 16, no. 14, pp. 5660-5670, Jul 2016.

[59] R. M. Corless and D. J. Jeffry, "Graphing Elementary Riemann Surfaces," *ACM Sigsam Bulletin*, vol. 32(1), no. 123, pp. 11-17, March 1998.

[60] B. X. Fu *et al.*, "Single-Shot Colored Speckle Pattern for High Accuracy Depth Sensing," *IEEE Sensors J.*, vol. 19, no. 17, pp. 7591-7597, Sep 2019.

[61] B. Grobwindhager, "The Potential of Low-cost Millimeter-Wave Sensors for Mobile Radar Applications," The Austrian Marshall Plan Foundation2019 Scholarship paper.

[62] K. Jin, G. Q. Li, T. Lai, T. Jin, and Y. J. Zhao, "A Novel Long-Time Coherent Integration Algorithm for Doppler-Ambiguous Radar Maneuvering Target Detection," *IEEE Sensors J.*, vol. 20, no. 16, pp. 9394-9407, Aug.15 2020.

[63] B.-u.-d. Ahmed, A. Kara, E. Zencir, and M. Benzaghta, "Opportunities and challenges in RCS measurement of 9-mm bullet model with 77 GHz mmwave COTS radar systems," *Microwave and Optical Technology Letters*, vol. 62, no. 12, pp. 3772-3778, 2020.

[64] S. W. Smith, *The Scientist and Engineer's Guide to Digital Signal Processing*. San Diego, California, USA: California Technical Publishing, 1997.

[65] S. A. Hovanessian, "Medium PRF Performance Analysis," *IEEE Transactions on Aerospace and Electronic Systems*, vol. AES-18, no. 3, pp. 286-296, 1982.

[66] D. Yuming, Y. Jianyu, and X. Jintao, "Novel method for ambiguity elimination in the linear FMCW radar," in *Proceedings 7th International Conference on Signal Processing, 2004. Proceedings. ICSP '04. 2004.*, 2004, vol. 3, pp. 2066-2069 vol.3.

[67] A. Ferrari, C. Berenguer, and G. Alengrin, "Doppler ambiguity resolution using multiple PRF," *IEEE Transactions on Aerospace and Electronic Systems*, vol. 33, no. 3, pp. 738-751, 1997.

[68] G. Trunk and S. Brockett, "Range and velocity ambiguity resolution," in *The Record of the 1993 IEEE National Radar Conference*, 1993, pp. 146-149.

[69] S. A. Hovanessian, "An Algorithm for Calculation of Range in a Multiple PRF Radar," *IEEE Transactions on Aerospace and Electronic Systems*, vol. AES-12, no. 2, pp. 287-290, 1976.

[70] W. Genyuan, X. Xiang-Gen, V. C. Chen, and R. L. Fielder, "Detection, location, and imaging of fast moving targets using multifrequency antenna array SAR," *IEEE Transactions on Aerospace and Electronic Systems*, vol. 40, no. 1, pp. 345-355, 2004.

[71] X. Li, H. Liang, and X. Xia, "A Robust Chinese Remainder Theorem With Its Applications in Frequency Estimation From Undersampled Waveforms," *IEEE Transactions on Signal Processing*, vol. 57, no. 11, pp. 4314-4322, 2009.

[72] C. Y. Chang and J. C. Curlander, "Application of the multiple PRF technique to resolve Doppler centroid estimation ambiguity for spaceborne SAR," *IEEE Transactions on Geoscience and Remote Sensing*, vol. 30, no. 5, pp. 941-949, 1992.

[73] C. Chi, H. Vishnu, K. T. Beng, and M. Chitre, "Utilizing Orthogonal Coprime Signals for Improving Broadband Acoustic Doppler Current Profilers," *IEEE Journal of Oceanic Engineering*, vol. 45, no. 4, pp. 1516-1526, 2020.

[74] G. V. Trunk and M. W. Kim, "Ambiguity resolution of multiple targets using pulse-Doppler waveforms," *IEEE Transactions on Aerospace and Electronic Systems*, vol. 30, no. 4, pp. 1130-1137, 1994.

[75] J. Y. N. Cho, "Multi-PRI signal processing for the Terminal Doppler weather radar. Part II: Range-velocity ambiguity mitigation," *Journal of Atmospheric and Oceanic Technology*, vol. 22, no. 10, pp. 1507-1519, Oct 2005.

[76] A. Wojtkiewicz, J. Misiurewicz, M. Nałęcz, K. Jedrzejewski, and K. Kulpa, "Two-dimensional Signal Processing in FMCW Radars," presented at the XXth National Conference on Circuit Theory and Electronic Networks, Kolobrzeg, Poland, 1997.

[77] J. Cho, "Improved range-velocity ambiguity mitigation for the Terminal Doppler Weather Radar," in *Proceedings of the 11th Conference on Aviation, Range and Aerospace Meteorology*, Hyannis, MA, 2004.

[78] W. Kester, "What the Nyquist Criterion Means to Your Sampled Data System Design ,MT-002 (Rev.A, 10/08, WK)," Analog Devices, Tutorial 2009.

[79] S. W. Smith, "ADC and DAC," in *The Scientist and Engineer's Guide to Digital Signal Processing*San Diego, California, USA: California Technical Publishing, 1997.

[80] H. Xiao, N. Du, Z. Wang, and G. Xiao, "Wrapped ambiguity Gaussian mixed model with applications in sparse sampling based multiple parameter estimation," *Signal Processing*, vol. 179, p. 107825, 2021/02/01/ 2021.

[81] N. Balal, Y. Balal, Y. Richter, and Y. Pinhasi, "Detection of Low RCS Supersonic Flying Targets with a High-Resolution MMW Radar," *Sensors,* vol. 20, no. 11, p. 3284, 2020.

[82] C. Yang, M. Miller, T. Nguyen, and E. Blasch, "Comparative Study of Coherent, Non-Coherent, and Semi-Coherent Integration Schemes for GNSS Receivers," in *Proceedings of the 63rd Annual Meeting of The Institute of Navigation*, Cambridge, MA, 2007, pp. 572-588.

[83] L. Gang, X. Jia, P. Ying-Ning, and X. Xiang-Gen, "Moving target location and imaging using dual-speed velocity SAR," in *2006 IEEE Antennas and Propagation Society International Symposium*, 2006, pp. 2701-2704.

[84] A. Melzer, A. Onic, F. Starzer, and M. Huemer, "Short-Range Leakage Cancelation in FMCW Radar Transceivers Using an Artificial On-Chip Target," *IEEE Journal of Selected Topics in Signal Processing*, vol. 9, no. 8, pp. 1650-1660, 2015.

[85] U. Chipengo, A. Sligar, and S. Carpenter, "High Fidelity Physics Simulation of 128 Channel MIMO Sensor for 77GHz Automotive Radar," *IEEE Access,* vol. 8, pp. 160643-160652, 2020.

[86] W. Zhang, H. Li, G. Sun, and Z. He, "Enhanced Detection of Doppler-Spread Targets for FMCW Radar," *IEEE Transactions on Aerospace and Electronic Systems,* vol. 55, no. 4, pp. 2066-2078, 2019.

[87] X. Li, X. Xia, and H. Liang, "A robust Chinese remainder theorem with its applications in moving target Doppler estimation," in *2010 IEEE Radar Conference*, 2010, pp. 1289-1294.

[88] C. Chi, H. Vishnu, K. T. Beng, and M. Chitre, "Robust Resolution of Velocity Ambiguity for Multifrequency Pulse-to-Pulse Coherent Doppler Sonars," *IEEE Journal of Oceanic Engineering,* vol. 45, no. 4, pp. 1506-1515, 2020.

[89] X. Huang, L. Cao, and A. Liu, "Sequential Estimation of Frequency and Direction-of-Arrival Based on the Relaxed Coprime Array for Multiple Targets," *IEEE Access,* vol. 8, pp. 80318-80332, 2020.

[90] Z. Li and K. Wu, "On the Leakage of FMCW Radar Front-End Receiver," in *2008 Global Symposium on Millimeter Waves*, 2008, pp. 127-130.

APPENDIX A

SUMMARY OF FIELD TEST DATA FOR VELOCITY AMBIGUITY RESOLUTION BY USE OF CRT

TABLE III SUMMARY OF FIELD TESTS RESULTS

Test No.	Frame No. of 2D FFT peak from Subframe 1	Frame No. of 2D FFT peak from Subframe 2	Column index for observed target velocity (dB magnitude of target peak cell) from subframe X RD-map (No. of chirps/frame = K)		Resolved Cell number from CRT (A)	CRT mid-point for velocity = $\left(\frac{K1\times K2}{2}\right)+0.5+1$) (B)	Doppler velocity resolution (Δv) (m/s) (C)	Resolved Velocity from CRT (m/s) (=Cell No. × Δv) (if A<B) Or - ((K1×K2) - A)× Δv) (if A>B)	Speed from Chronograph (m/s)
			Subframe 1 (K=17)	Subframe 2 (K=15)					
1.		292		15 (107.62)	15 (15,15)	129	4.52	**67**	**210**
	293	293	15 (112.27)	4 (100.92)	49			**221**	
	294	294	15 (101.45)	4 (98.33)	49			**221**	
	295	295	15 (94.95)	4 (94.41)	49			**221**	
2.		272		2 (108.52)	32 (15,2)	129	4.52	**144**	**208**
	273	273	15 (108.52)	4 (138.56)	49			**221**	
	274	274	15 (99.48)	4 (98.70)	49			**221**	
	275	275	15 (98.07)	4 (92.26)	49			**221**	
3.		182		15	15 (15,15)	129	4.52	**67**	**151**
	183	183	15 (107.81)	4 (102.96)	49			**221**	
	184	184	15 (100.72)	4 (95.29)	49			**221**	
	185	185	15 (94.97)	4 (93.54)	49			**221**	
4.	135	135	14 (113.37)	4 (103.63)	184	129	4.52	**-320**	**214**
	136	136	15 (99.91)	4 (100.55)	49			**221**	
	137	137	15 (99.69)	4 (93.97)	49			**221**	
	138	138	15 (93.56)	4 (91.18)	49			**221**	

Test No.	Frame No. of 2D FFT peak from Subframe 1	Frame No. of 2D FFT peak from Subframe 2	Column index for observed target velocity (dB magnitude of target peak cell) from subframe X RD-map (No. of chirps/frame = K)		Resolved Cell number from CRT (A)	CRT mid-point for velocity = $\left(\frac{K1\times K2}{2}\right)+0.5+1$ (B)	Doppler velocity resolution (Δv) (m/s) (C)	Resolved Velocity from CRT (m/s) (=Cell No. × Δv) (if A<B) Or - ((K1×K2) - A)× Δv) (if A>B)	Speed from Chronograph (m/s)
			Subframe 1 (K=17)	Subframe 2 (K=15)					
5.		698		2 (107.99)	167 (14,2)	129	4.52	**-411**	**136**
	699	699	14 (107.92)	3 (101.35)	48			**216**	
	700	700	14 (98.13)	3 (94.70)	48			**216**	
	701	701	14 (94.94)	3 (90.39)	48			**216**	
6.	163	163	12 (112.07)	2 (106.67)	182	129	4.52	**-194**	**157**
	164	164	14 (103.22)	3 (99.17)	48			**216**	
	165	165	14 (97.06)	3 (95.02)	48			**216**	
	166	166	14 (94.08)	3 (88.28)	48			**216**	
7.		291		15 (108.93)	165 (12,15)	129	4.52	**-406**	**200**
	292	292	12 (106.74)	1 (101.99)	46			**208**	
	293	293	12 (101.17)	1 (95.67)	46			**208**	
	294	294	12 (95.56)	1 (94.76)	46			**208**	
8.	207	207	9 (106.87)	15 (111.95)	60	129	4.52	**271**	**199**
	208	208	12 (102.48)	1 (102.31)	46			**208**	
	209	209	12 (99.58)	1 (97.64)	46			**208**	
	210	210	12 (93.73)	1 (95.63)	46			**208**	
9.		163		12 (95.05)	147 (11,12)	129	4.52	**-488**	**200**
	164	164	11 (112.87)	1 (107.68)	181			**-334**	
	165	165	12 (100.59)	1 (100.43)	46			**208**	
	166	166	12 (98.72)	1 (97.55)	46			**208**	
Tests with lighter pellet									
10.	644	644	12 (110.15)	1 (104.19)	46	129	4.52	**207**	**212**
	645	645	15 (101.96)	4 (95.78)	49			**221**	

Test No.	Frame No. of 2D FFT peak from Subframe 1	Frame No. of 2D FFT peak from Subframe 2	Column index for observed target velocity (dB magnitude of target peak cell) from subframe X RD-map (No. of chirps/frame = K)		Resolved Cell number from CRT (A)	CRT mid-point for velocity = $\left(\frac{K1\times K2}{2}\right) + 0.5+1$) (B)	Doppler velocity resolution (Δv) (m/s) (C)	Resolved Velocity from CRT (m/s) (=Cell No. × Δv) (if A<B) Or - ((K1×K2) - A)× Δv) (if A>B)	Speed from Chronograph (m/s)
			Subframe 1 (K=17)	Subframe 2 (K=15)					
	646	646	15 (98.15)	4 (93.67)	49			**221**	
	647	647	15 (90.68)	4 (87.97)	49			**221**	
11.		92		15 (109.96)	80 (12,15)	129	4.52	**361**	**204**
	93	93	12 (106.20)	1 (101.68)	46			**207**	
	94	94	13 (101.60)	2 (94.40)	47			**212**	
	95	95	13 (93.19)	2 (90.46)	47			**212**	
Consider these tests 12 and 13 as examples when zero-Doppler is more problematic									
12.	396	396	9 (100.56)	2 (108.69)	77	129	4.52	**343**	**206**
	397	397	13 (100.86)	2 (98.58)	47			**212**	
	398	398	13 (97.93)	2 (94.83)	47			**212**	
	399	399	13 (90.36)	1 (92.23) Or 2 (90.98)	166 47			**-402** **212**	
13.	413	413	11 (107.01)	2 (105.65)	62	129	4.52	**280**	**205**
	414	414	13 (102.15)	2 (99.49)	47			**212**	
	415	415	13 (96.94)	2 (94.11)	47			**212**	
	416	416	13 (94.18)	1 (91.96) Or 2 (91.35)	166 47			**-402** **212**	
Tests with lighter pellet, K1=K2=17									
14.	116	116	11 (99.63)	13 (108.66)	Not applicable as bases are not coprime	129	4.52		**207**
	117	117	13 (101.42)	14 (97.77)					
	118	118	14 (95.87)	14 (91.47)					
	119	119	13 (89.22)	13 (90.43)					

Test No.	Frame No. of 2D FFT peak from Subframe 1	Frame No. of 2D FFT peak from Subframe 2	Column index for observed target velocity (dB magnitude of target peak cell) from subframe X RD-map (No. of chirps/frame = K)		Resolved Cell number from CRT (A)	CRT mid-point for velocity = $\left(\frac{K1 \times K2}{2}\right) + 0.5+1$) (B)	Doppler velocity resolution (Δv) (m/s) (C)	Resolved Velocity from CRT (m/s) (=Cell No. × Δv) (if A<B) Or - ((K1×K2) - A)× Δv) (if A>B)	Speed from Chronograph (m/s)
			Subframe 1 (K=17)	Subframe 2 (K=15)					
15.		726		10 (109.86)	Not applicable as bases are not coprime	129	4.52		**204**
	727	727	12 (110.07)	13 (102.38)					
	728	728	13 (103.01)	13 (100.91)					
	729	729	13 (96.73)	13 (9322)					
Tests with lighter pellet, K1=K2=15									
16.	76	76	15 (110.64)	1 (105.87)	Not applicable as bases are not coprime	129	4.52		**202**
	77	77	1 (106.16)	1 (104.74)					
	78	78	1 (97.61)	1 (93.45)					
	79	79	1 (96.25)	1 (97.24)					
17.	88	88	11 (101.53)	15 (109.65)	Not applicable as bases are not coprime	129	4.52		**192**
	89	89	14 (102.23)	14 (92.75)					
	90	90	14 (96.89)	14 (97.64)					
	91	91	14 (91.22)	14 (86.31)					
Tests with lighter pellet, parameters tried to be tuned for 200 m/s speed									
18.		232		1 (104.26)	31 (14,1)	129	4.41	**136**	**207**
	233	233	14 (111.35)	4 (100.6)	184			**-313**	
	234	234	15 (99.18)	4 (97.45)	49			**216**	
	235	235	15 (94.67)	4 (89.62)	49			**216**	
19.	70	70	11 (108.23)	2 (103.84)	62	129	4.41	**273**	**201**
	71	71	13 (103.86)	2 (101.24)	47			**207**	
	72	72	13 (99.15)	2 (92.97)	47			**207**	
	73	73	13 (94.89)	2 (93.62)	47			**207**	

Test No.	Frame No. of 2D FFT peak from Subframe 1	Frame No. of 2D FFT peak from Subframe 2	Column index for observed target velocity (dB magnitude of target peak cell) from subframe X RD-map (No. of chirps/frame = K)		Resolved Cell number from CRT (A)	CRT mid-point for velocity = $\left(\frac{K1\times K2}{2}\right)+0.5+1$ (B)	Doppler velocity resolution (∆v) (m/s) (C)	Resolved Velocity from CRT (m/s) (=Cell No. × ∆v) (if A<B) Or - ((K1×K2) - A)× ∆v) (if A>B)	Speed from Chronograph (m/s)
			Subframe 1 (K=17)	Subframe 2 (K=15)					
20.	106	106	11 (99.73)	3 (107.40)	198	129	4.41	**-251**	**208**
	107	107	15 (102.14)	4 (100.11)	49			**216**	
	108	108	15 (98.69)	4 (92.81)	49			**216**	
	109	109	15 (93.46)	4 (91.14)	49			**216**	
Tests with heavier pellet, parameters tried to be tuned for 200 m/s speed									
21.	222	222	8 (98.46)	15 (110.72)	195	129	4.41	**-264**	**194**
	223	223	11 (104.40)	1 (100.68)	181			**-326**	
	224	224	12 (96.35)	1 (96.31)	46			**202**	
	225	225	12 (93.71)	1 (97.81)	46			**202**	
22.		165		12 (94.67)	147 (11,12)	129	4.41	**-555**	**196**
	166	166	11 (112.99)	1 (104.1)	181			**-326**	
	167	167	12 (100.00)	1 (103.46)	46			**202**	
	168	168	12 (98.38)	1 (97.42)	46			**202**	